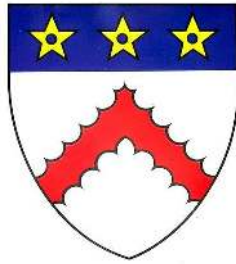# A Search For Sterile Neutrinos at the MINOS Experiment

Robert N. M. Pittam

Keble College, Oxford

Thesis submitted in partial fulfilment of the requirements for the degree of Doctor of Philosophy at the University of Oxford

Hilary Term, 2010

A Search For Sterile Neutrinos at the MINOS Experiment

Robert N. M. Pittam
Keble College, Oxford

Thesis submitted in partial fulfilment of the requirements for the degree of
Doctor of Philosophy at the University of Oxford

Hilary Term, 2010

Abstract

MINOS is a long baseline neutrino oscillation experiment based at the Fermi National Accelerator Laboratory in Illinois, USA. The experiment was designed to study neutrino oscillation phenomena. The ν_μ beam produced by the NuMI beam facility at FNAL is used along with two functionally identical detectors. The Near Detector at FNAL and a Far Detector 735 km away in the Soudan Underground Laboratory in northern Minnesota. Comparison of the observed spectra of neutrinos at the two detectors provides the evidence for neutrino oscillations.

This thesis presents work on the postulated phenomena of sterile neutrinos. Oscillations between active and sterile neutrinos will lead to a deficit in the expected rate of measured Neutral Current interactions at the Far Detector. A technique for selecting Neutral Current events utilising an Artificial Neural Network is presented with resulting overall efficiency of 91.1% and purity of 66.0%. A method of predicting the expected Charged and Neutral Current energy spectra at the Far Detector given the data recorded at the Near Detector is presented. A model to search for oscillations between sterile and active neutrinos is developed. Sources of systematic uncertainty that can effect the results of the analysis are discussed.

The analysis developed is applied to a Standard Model 3 flavour oscillation model as a cross check under the scenarios with and without ν_e appearance. The oscillation parameters measured by this model are $\Delta m_{32}^2 = (2.39^{+0.23}_{-0.15}) \times 10^{-3}$ eV^2 and $\theta_{23} = 0.727^{+0.22}_{-0.11}$ for the no ν_e appearance result. An analysis of the resulting prediction reveals no evidence for active neutrino disappearance.

The analysis is then performed using the 4 flavour neutrino oscillation model developed. Again this is done under the 2 scenarios of ν_e appearance and no ν_e appearance. The results of this analysis are $\Delta m_{31}^2 = (2.44^{+0.23}_{-0.14}) \times 10^{-3}$ eV^2, $\theta_{23} = 0.755^{+0.19}_{-0.12}$ and $\theta_{34} = 0.00^{+0.35}$ for no ν_e appearance and $\Delta m_{31}^2 = (2.46^{+0.21}_{-0.14}) \times 10^{-3}$ eV^2, $\theta_{23} = 0.849^{+0.12}_{-0.19}$ and $\theta_{34} = 0.00^{+0.60}$ for ν_e appearance. This is consistent with no oscillations between active and sterile neutrinos.

Contents

List of Figures

List of Tables

Chapter 1

Introduction

From humble beginnings as an unwanted postulate to explain an anomalous experimental result the neutrino is now a fundamental part of the Standard Model of particle physics. Arguably the most exciting developments in the field of particle physics in the previous decade have been in the study of neutrinos.

A gathering body of experimental evidence suggests that neutrinos undergo flavour oscillations in contrast to the Standard Model assumption of flavour conservation. These oscillations indicate that the neutrinos have must have a mass much smaller than the other particles in the Standard Model opening up a series of interesting theoretical possibilities to explain this.

One such experiment performing neutrino oscillation studies is the MINOS experiment based at the Fermi National Accelerator Laboratory in Illinois USA. MINOS is a terrestrial long baseline experiment that makes use of the NuMI neutrino beam and 2 steel/scintillator calorimeter detectors. The Near Detector is near the beam production point at Fermilab and the Far Detector is located 735 km away in the Soudan Underground Laboratory in northern Minnesota. Comparison of the measured spectra at each detector reveals information about possible

neutrino oscillations. It is the study of neutrinos using the MINOS experiment that forms the basis of this thesis. In particular the study of the Neutral Current interaction is considered to search for oscillations into a so called sterile neutrino.

Chapter 2 presents an introduction to the field of neutrino physics including a brief history of the topic followed by a derivation of the formalism necessary to understand neutrino oscillations. Also included is a summary of the current experimental evidence for neutrino oscillation phenomena and a discussion of future work to be performed in the field to contextualise the work of the MINOS experiment to the field as a whole

Chapter 3 describes the MINOS experiment in detail. Providing descriptions of the NuMI neutrino beam and the detector technology. It also contains descriptions of the physics goals of the experiment and presents some of the successful analyses already performed by the MINOS collaboration.

Chapter 4 demonstrates the technique used to separate events due to the Neutral and Charged current interactions. This utilises a series of pre-classification cuts followed by an Artificial Neural Network. Also included in this chapter is a description of the necessary data cleaning to ensure good event selection.

Chapter 5 describes in detail the technique used to predict the Neutral Current and Charged Current spectra at the Far Detector based on the measured Near Detector spectra in a process called extrapolation. As a part of the extrapolation a fit is performed on the Neutral Current spectra in the Near Detector between the measured data and the Monte Carlo simulation in different NuMI beam configurations and this is also described.

Chapter 6 then expands on the formalism for oscillations introduced in Chapter 2 to develop a model of oscillation involving sterile neutrinos. The full formalism for 4 neutrino oscillations is presented and the assumptions and simplifications

necessary before the model can be be applied to the MINOS data are discussed.

Chapter 7 presents the result of the analysis outlined in the thesis up to this point. First the systematic errors that could effect the measurements of the oscillation analysis are discussed and finally a cross check analysis using only 3 neutrino flavour oscillations and the result of the full 4 flavour oscillation treatment are presented and discussed.

The final Chapter 8 summarises and concludes the thesis. The result are summarised within the context of the current understanding of neutrino physics and the implications and any further work to be performed by the MINOS collaboration are discussed.

Chapter 2

The History and Physics of Neutrinos

2.1 History of the Neutrino

In the early part of the 20th century it had been experimentally determined that the spectrum of electrons observed in β-decay was continuous. This was a problem as electrons emitted in β-decay were of too high an energy to be from atomic orbitals and therefore must have come from the nucleus and therefore should have a unique energy. This continuous energy spectrum of β-decay electrons in contradiction of the theory implied that energy conservation was violated. To resolve this and the additional problem of spin statistics in β-decay Wolfgang Pauli in 1930 postulated, in an open letter to a physics conference in Tübingen [1], the existence of a neutral weakly interacting fermion which would be emitted with the electron in β-decay. He called this particle the neutron.

Two years after Pauli's letter, in 1932, John Chadwick discovered the particle we now call the neutron in experiments involving bombarding beryllium and boron

with α radiation [2]. This resulted in Enrico Fermi renaming the Pauli particle the neutrino being an Italian play on words and meaning "small neutral one".

The next stage in the development of the neutrino was Fermi's theory of β interactions published in 1934 [3][1] which put the neutrino on a firm theoretical footing and implied the neutrino was massless. Further work by Hans Bethe and Rudolf Peirels showed it to have a very small cross section for interaction with matter [5]. The spectacular success of Fermi's theory did much to support the existence of the neutrino but 2 decades were to pass before it was observed experimentally.

A neutrino was first experimentally observed in 1956 by Frederick Reines and Clyde Cowan in experiments at a nuclear reactor at the Savannah River Plant facility [6, 7]. They detected $\overline{\nu}$ by the use of inverse β-decay $\overline{\nu} + p \to n + e^+$ in 2 tanks of water with $CdCl_2$ dissolved in it, sandwiched between 3 layers of liquid scintillator. The positron annihilation photons were detected immediately with the photons due to the neutron capture in the cadmium detected a short time later.

Also in 1956 in response to the $\tau - \theta$ puzzle[2] Tsung-Dao Lee and Chen-Ning Yang noted that parity seemed to be violated in weak decays and suggested several experimental tests to determine one way or another [8]. These suggestions were immediately acted on and experiments performed in 1957 found parity violation in the β-decay of polarised ^{60}Co [9] and in pion $\pi^+ \to \mu^+ + \nu_\mu$ and muon $\mu^+ \to e^+ + \nu_e + \overline{\nu}_\mu$ decays [10].

In light of these discoveries it was necessary to modify Fermi's theory which was constructed implicitly assuming parity conservation. In particular the vector-

---

[1]A translation into English of which can be found in [4].
[2]In which two otherwise identical particles could only be distinguished by their decay mode to opposite parity states of 2 or 3 pions.

vector nature of the interaction was replaced with a vector-axial form. In this theory the neutrino and anti-neutrino must have definite and opposite helicity. In 1958, in a widely acclaimed experiment, Goldhaber *et al.* determined the helicity of the neutrino to be left-handed [11].

Fermi's theory involved a point like interaction. It was realised that this violated unitarity and was probably a low energy approximation and at higher energies a propagator was most likely involved. This followed on from work by Hideki Yukawa showing the use of exchange bosons in the strong force. The exchange boson required would be spin 1 and must have mass to explain the short range. However simply adding the mass to the boson lead to divergences in the theory. A problem which was solved in 1967 by Sheldon Glashow [12], Steven Weinberg [13] and Abdus Salam [14] in the GWS theory. As well as solving the divergences problem the GWS theory unified the weak and electromagnetic forces into the electroweak force, predicted weak neutral currents and the masses of the charged and neutral current exchange bosons (W and Z).

The predicted neutral current interaction mediated by the Z boson would be similar to the interactions of a photon but with a short range due to the Z mass and with the additional distinction that, unlike the electromagnetic force, it would involve neutrinos. Consequently neutrino beams were the ideal place to search for neutral current interactions and the first was observed in 1973 in the Gargamelle bubble chamber experiment at CERN in both $\nu_\mu + e^- \rightarrow \nu_\mu + e^-$ [15] and $\nu_\mu + N \rightarrow \nu_\mu + Hadrons$ [16, 17] channels. This was subsequently confirmed at Fermilab [18]. The neutrino was thus confined to having only weak interactions due to it being non-hadronic and electrically neutral. The allowed neutrino interactions are shown in Figure 2.1.

Other developments in the particle physics world had begun to impact on
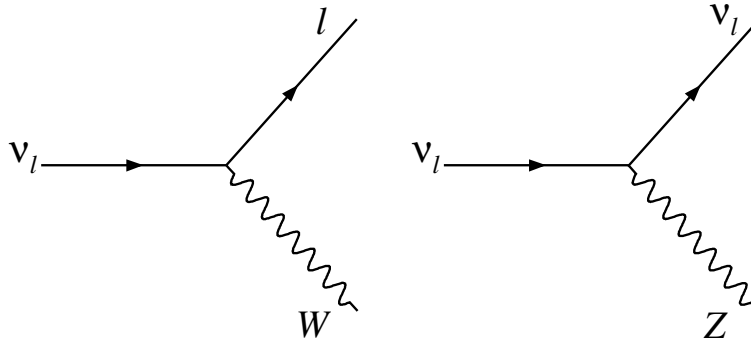
Figure 2.1: The possible interactions of the neutrino of flavour l. The Charged Current (CC) vertex is shown on the left. The Neutral Current (NC) vertex shown on the right.

neutrinos. In the early 1940s it was realised that rather than being Yukawa's "meson"[3] the muon and pion were actually separate particles. Indeed it transpired that the muon shared all the properties of the electron except for its greater mass. The pion decayed to the muon in a very similar way to β-decay resulting in a neutrino. However it was not known whether this was the same neutrino as was involved in β-decay. The lack of decays such as $\mu \rightarrow e\gamma$ suggested that the 2 neutrinos were distinct. If this was the case then $\nu_\mu + n \rightarrow p + e^-$ was forbidden. A suggestion followed that if it could be shown that the ν_μ produced in pion decay cannot induce e^-, then ν_μ and ν_e are distinct. This was demonstrated experimentally in 1962 at Brookhaven which showed that the 2 neutrinos were distinct in the first experiment to use a neutrino beam [19].

The τ lepton was discovered in 1975 by Martin Perl [20] at the SPEAR[4] collider and naturally raised the question of whether there was an associated neutrino. Measurements of the width of the Z at LEP in 1989 had shown that there were 3 neutrino flavours [21] and the ν_τ was eventually observed in 2001 at the DONUT[5]

---

[3]which was originally suspected to the mediating particle in the strong nuclear force
[4]Stanford Positron Electron Asymmetric Ring
[5]Direct Observation of NU Tau

experiment at Fermilab [22].

2.2 Neutrino Flavour Change and Oscillations

The first proposal of the possibility of flavour change in neutrinos was in 1957 by Pontecorvo [23]. Motivated by predictions of $K^0 \rightleftarrows \overline{K}^0$ mixing he postulated mixing between the only neutrinos available to him at the time $\nu \rightleftarrows \overline{\nu}$. The failure of Raymond Davis Jr. to observe events of the type $\overline{\nu}_e +^{37} \text{Cl} \rightarrow^{37} \text{Ar} + e^+$ in an experiment at Brookhaven [24] in 1955 eliminated this possibility as the interaction should be allowed if $\overline{\nu}$ oscillate to ν. Furthermore, the development of the V-A theory of weak interactions stated that even if the right-handed $\overline{\nu}$ oscillated to right-handed ν (as helicity is conserved) the process would still not be possible as the interaction can only be caused by left-handed neutrinos. Following the discovery of the ν_μ in 1967 he proposed the possibility of $\nu_\mu \rightleftarrows \nu_e$ flavour changing oscillations .

The nature of neutrino phenomena is in some way dependent on the nature of neutrinos themselves. A full treatment of the nature of neutrinos is beyond the scope of this thesis and is only presented in summary here but details can be found in for example [23]. There are 2 possible types of neutrino termed Dirac and Majorana. In the case of Dirac neutrinos ν and $\overline{\nu}$ are distinct particles. In the case of Majorana neutrinos ν and $\overline{\nu}$ are the same particle. In the case that neutrinos have no mass Dirac and Majorana neutrinos are identical. Current experimental evidence shows that neutrinos have a small mass. Combining Dirac and Majorana neutrinos can lead to a plausible explanation of the small size of the neutrino mass via the see-saw mechanism [23]. The nature of neutrinos can be determined from double-β decay experiments. Double-β decays that produce neutrinos will imply

Dirac neutrinos. Neutrinoless double-β decay would imply Majorana neutrinos due to the identical neutrino and anti-neutrino cancelling each other. Double-β decay experiments are an active area of neutrino research.

2.2.1 Neutrino Oscillations

For neutrino oscillations to take place 2 conditions are required to be satisfied; leptonic mixing and neutrinos having mass.

Neutrinos experience the weak force as lepton flavour eigenstates ν_α. When a neutrino undergoes a weak Charged Current interaction it does so in some definite flavour associated with the lepton that appears at the W interaction vertex l_α.

Neutrinos propagate through a vacuum as mass eigenstates ν_i. There is no need for these two bases to be equivalent. The neutrino of definite flavour can be expressed as a combination of mass eigenstates[6]:

$$|\nu_\alpha\rangle = \sum_i U_{\alpha i}^* |\nu_i\rangle . \tag{2.1}$$

where i runs over the number of neutrino states. The matrix U is the unitary leptonic mixing matrix often called the PMNS (or MNS) matrix after Pontecorvo, Maki, Nakagawa and Sakata who were leading figures in the development of theories of mixing and oscillation.

The process by which a neutrino changes flavour is therefore a quantum mechanical one found by evaluating the time evolution of Equation 2.1. The mass eigenstates evolve as the neutrino propagates:

$$|\nu_\alpha(t)\rangle = \sum_i U_{\alpha i}^* e^{-ip.x} |\nu_i\rangle . \tag{2.2}$$

---

[6]The convention chosen here is that used in [25]

To calculate the probability of ν_α oscillating to ν_β it is necessary to calculate the matrix element $\langle \nu_\beta | \nu_\alpha(t) \rangle$. From equation 2.1 we have:

$$\langle \nu_\beta | = \sum_j U_{\beta j} \langle \nu_j |. \tag{2.3}$$

And the matrix element given as:

$$\langle \nu_\beta | \nu_\alpha(t) \rangle = \sum_i U_{\beta i} U_{\alpha i}^* e^{-ip.x} \tag{2.4}$$

Labelling the ith neutrino mass eigenstate momentum as $\mathbf{p_i}$ and mass as m_i and assuming all ν_i have a common Energy E[7] we have $p_i.x = Et - \mathbf{p}_i.\mathbf{x}$. In the extreme relativistic limit we have $t = L$ and $\mathbf{p}_i.\mathbf{x} = \mathbf{p}_i.L$ where L is the distance travelled. Assuming $m_i \ll E$ we can expand $\mathbf{p}_i = (E^2 + m_i^2)^{\frac{1}{2}} \approx E + \frac{m_i^2}{2E}$ to give $p_i \cdot x = \frac{m_i^2}{2E}L$. Substituting into Equation 2.4 we have

$$\langle \nu_\beta | \nu_\alpha(L) \rangle = \sum_i U_{\beta i} U_{\alpha i}^* e^{-i\frac{m_i^2}{2E}L} \tag{2.5}$$

This then gives the probability of ν_α oscillating to ν_β as:

$$
\begin{aligned}
P(\nu_\alpha \to \nu_\beta) &= | \langle \nu_\beta | \nu_\alpha(L) \rangle |^2 \\
&= \sum_i U_{\beta i} U_{\alpha i}^* e^{-i\frac{m_i^2}{2E}L} \sum_j U_{\beta j}^* U_{\alpha j} e^{+i\frac{m_j^2}{2E}L} \\
&= \sum_i \sum_j U_{\beta i} U_{\alpha i}^* U_{\beta j}^* U_{\alpha j} e^{-i\frac{\Delta m_{ij}^2}{2E}L}
\end{aligned}
\tag{2.6}
$$

Where $\Delta m_{ij}^2 = m_i^2 - m_j^2$. The expression for the probability can be further simplified by adding

---

[7]This is an approximation due the use of plane waves. A more exact treatment using wave packets [26] has been shown to give the same result.

$$\sum_i \sum_j U_{\beta i} U_{\alpha i}^* U_{\beta j}^* U_{\alpha j} - \sum_i \sum_j U_{\beta i} U_{\alpha i}^* U_{\beta j}^* U_{\alpha j}$$

(which obviously sums to 0) to Equation 2.6 and rearranging to give:

$$P(\nu_\alpha \to \nu_\beta) = \sum_i U_{\beta i} U_{\alpha i}^* \sum_j U_{\beta j}^* U_{\alpha j} + \sum_i \sum_j U_{\beta i} U_{\alpha i}^* U_{\beta j}^* U_{\alpha j} \left(e^{-i\frac{\Delta m_{ij}^2}{2E}L} - 1 \right)$$

(2.7)

Due to U being unitary the first term can be expressed as $\delta_{\alpha\beta}$. To simplify the second term we note that when $i = j$ it simplifies to 0 and the terms where $i > j$ are complex conjugates of the terms where $i < j$. When summing over this term we can therefore pair up those that are not 0 to give

$$P(\nu_\alpha \to \nu_\beta) = \delta_{\alpha\beta} + 2 \sum_{i>j} \mathfrak{Re} \left[U_{\beta i} U_{\alpha i}^* U_{\beta j}^* U_{\alpha j} \left(e^{-i\frac{\Delta m_{ij}^2}{2E}L} - 1 \right) \right]$$

(2.8)

Making use of

$$e^{-i\frac{\Delta m_{ij}^2}{2E}L} = \cos\left(\frac{\Delta m_{ij}^2}{2E}L \right) + i \sin\left(\frac{\Delta m_{ij}^2}{2E}L \right)$$

and the trigonometric identity

$$\cos\left(\frac{\Delta m_{ij}^2}{2E}L \right) = 1 - 2\sin^2\left(\frac{\Delta m_{ij}^2}{4E}L \right)$$

We have the final probability expressed as

$$P(\nu_\alpha \to \nu_\beta) = \delta_{\alpha\beta} - 4 \sum_{i>j} \mathfrak{Re} \left[U_{\beta i} U_{\alpha i}^* U_{\beta j}^* U_{\alpha j} \right] \sin^2 \left(\frac{\Delta m_{ij}^2}{4E} L \right)$$
$$+ 2 \sum_{i>j} \mathfrak{Im} \left[U_{\beta i} U_{\alpha i}^* U_{\beta j}^* U_{\alpha j} \right] \sin \left(\frac{\Delta m_{ij}^2}{2E} L \right) \qquad (2.9)$$

In the case where $\nu_\beta = \nu_\alpha$ the 3rd term will give 0 and Equation 2.9 gives the survival probability. This is often the case in neutrino experiments. A known flux of neutrinos is measured after some propagation distance to see if neutrinos have disappeared. Hence these experiments are termed disappearance experiments.

$$P(\nu_\alpha \to \nu_\alpha) = 1 - 4 \sum_{i>j} |U_{\alpha i}|^2 |U_{\alpha j}|^2 \sin^2 \left(\frac{\Delta m_{ij}^2}{4E} L \right) \qquad (2.10)$$

In contrast an appearance experiment uses a known flux of neutrinos and looks for the appearance of a neutrino not originally within that flux.

CP violation

Assuming that CPT invariance holds we have:

$$P\left(\overline{\nu}_\alpha \to \overline{\nu}_\beta \right) = P\left(\nu_\beta \to \nu_\alpha \right) \qquad (2.11)$$

In addition a careful examination of Equation 2.9 shows that

$$P\left(\nu_\beta \to \nu_\alpha; U \right) = P\left(\nu_\alpha \to \nu_\beta; U^* \right) \qquad (2.12)$$

So when CPT is inviolate substituting Equation 2.11 into Equation 2.12 gives:

$$P\left(\overline{\nu}_\alpha \to \overline{\nu}_\beta; U \right) = P\left(\nu_\alpha \to \nu_\beta : U^* \right) \qquad (2.13)$$

In other words the oscillation probability for neutrinos and anti-neutrinos is the same under the substitution of U for its hermitian conjugate.

Thus neutrino and anti-neutrino oscillation probabilities can differ if U is not real leading to an opposite sign in the third term of Equation 2.9. Assuming CPT invariance then any difference between the neutrino and anti-neutrino probabilities is due to CP violation. As stated above the third term is 0 when looking at the survival probability. Thus if CPT is conserved neutrino and anti-neutrino oscillations should be the same for disappearance experiments. A further consequence is that only experiments looking for neutrino appearance are sensitive to CP violation.

2.3 Standard Model Oscillations

The treatment in the previous section was general and applies to any number of neutrino flavours and mass eigenstates. Here we consider the application of oscillations in the case of the standard model.

2.3.1 The 3 Flavour Model

There are 3 flavours of neutrino in the Standard Model and therefore the PMNS matrix is given by

$$U = \begin{pmatrix} U_{e1} & U_{e2} & U_{e3} \\ U_{\mu1} & U_{\mu2} & U_{\mu3} \\ U_{\tau1} & U_{\tau2} & U_{\tau3} \end{pmatrix} \tag{2.14}$$

The unitarity of the matrix results in it having 9 real parameters. Under the assumption of Dirac neutrinos 5 of these parameters which are relative phases between the 3 leptons and 3 neutrinos and can be absorbed by those fields. This

leaves U with 4 free parameters; 3 of these can be expressed as rotations with the 4th as a complex phase. The matrix is often parameterised in terms of the 3 mixing angles θ_{12}, θ_{13} and θ_{23} and the CP violating phase δ as

$$
U = \begin{pmatrix} 1 & 0 & 0 \\ 0 & c_{23} & s_{23} \\ 0 & -s_{23} & c_{23} \end{pmatrix} \begin{pmatrix} c_{13} & 0 & s_{13}e^{-i\delta} \\ 0 & 1 & 0 \\ -s_{13}e^{i\delta} & 0 & c_{13} \end{pmatrix} \begin{pmatrix} c_{12} & s_{12} & 0 \\ -s_{12} & c_{12} & 0 \\ 0 & 0 & 1 \end{pmatrix} \quad (2.15)
$$

where $c_{ij} = \cos\theta_{ij}$ and $s_{ij} = \sin\theta_{ij}$. If the neutrinos are Majorana only 3 of the complex phases can be absorbed and a further diagonal matrix is required in the parameterisation $\mathrm{diag}(e^{i\alpha_1}/2, e^{i\alpha_2}/2, 1)$. However these phases are unobservable as they cancel in Equation 2.4.

This parameterisation is useful when considering the experimental tests of oscillations which will be outlined in greater detail in the next section. The first rotation measures the effects of oscillations in the atmospheric neutrino sector. The third rotation measures the effect of the oscillations in the solar neutrino sector. The middle rotation contains the so far unmeasured θ_{13} and the phase. Taking the complex conjugate of U in this form shows that only the sign of δ changes and it is therefore know as the CP violating phase. This sector is the focus of current and future experimental programs. This parameterisation is desirable due to the experimental findings that θ_{13} is small and that the two mass splittings Δm_{21}^2 and Δm_{32}^2 are very different. These findings will be discussed later in the chapter. The consequence of this is that the middle matrix in Equation 2.15 is nearly diagonal and that the 2 flavour approximation becomes valid as described in the next section.

This parameterisation can further be expressed as

$$U = \begin{pmatrix} c_{13}c_{12} & c_{13}s_{12} & s_{13}e^{-i\delta} \\ -c_{23}s_{12} - s_{13}c_{12}s_{23}e^{+i\delta} & c_{23}c_{12} - s_{13}s_{12}s_{23}e^{+i\delta} & c_{13}s_{23} \\ s_{23}s_{12} - s_{13}c_{12}c_{23}e^{+i\delta} & -s_{23}c_{12} - s_{13}s_{12}c_{23}e^{+i\delta} & c_{13}c_{23} \end{pmatrix} \qquad (2.16)$$

2.3.2 2 Flavour Approximation

In the case with 3 flavours there are 3 mass eigenstates and therefore 2 mass splittings. If one of these mass splittings ΔM^2 is much larger than the other then if an experiment is designed with an L/E such that $\Delta M^2 L/E = \mathcal{O}(1)$ it will effectively only notice the big mass splitting. In this experiment all the neutrinos above and below ΔM^2 appear to be only 1 neutrino. In actuality the oscillations take place between combination of the two neutrinos with the small mass splitting. As there is only 1 mass splitting the PMNS matrix takes on the form:

$$U = \begin{pmatrix} \cos\theta & \sin\theta \\ -\sin\theta & \cos\theta \end{pmatrix} \qquad (2.17)$$

Substituting this into 2.9 the 2 flavour approximation oscillation and survival probabilities become

$$P(\nu_\alpha \to \nu_\beta) \simeq \sin^2(2\theta)\sin^2\left(1.267\frac{\Delta M^2}{E}L\right)$$
$$P(\nu_\alpha \to \nu_\alpha) \simeq 1 - \sin^2(2\theta)\sin^2\left(1.267\frac{\Delta M^2}{E}L\right) \qquad (2.18)$$

Where the numerical factor 1.267 comes from re-inserting the so far neglected factors of $\hbar$ and c and expressing ΔM^2 in units of eV^2, L in km and E in GeV.

As U is real in this case it means CP violation is not possible.

It has been determined experimentally as will be demonstrated in Section 2.4 that $\Delta m^2_{32} \gg \Delta m^2_{21}$ and therefore the 2 neutrino oscillation approximation is valid in many experiments. When considering oscillations in the atmospheric sector described in Section 2.4.3 the large mass splitting ΔM^2 in Equation 2.18 is therefore some combination of Δm^2_{32} and Δm^2_{31}. This is given various names in neutrino literature including Δm^2_{atm}. In this thesis the atmospheric 2 flavour approximation mass splitting is referred to as Δm^2_{32}.

2.3.3 4 Flavour Oscillations and Sterile Neutrinos

As will be seen in the next section almost all experimental data is in agreement with the picture of 3 neutrino flavours and 2 mass splittings. However the LSND experiment [27] implies there is a 3rd mass splitting. This would require at least a 4th mass and flavour eigenstate.

Assuming the fourth neutrino to be lighter than the W mass this 4th flavour eigenstate would seem to have no charged lepton associated with it and therefore would not couple to the W boson.

Precision measurements of the width of the Z boson [28] have shown the number of light neutrinos that couple to the Z to be 2.9840 ± 0.008. Therefore the 4th flavour eigenstate (if it exists) would not be able to couple to the Z boson either. As it has no interactions this hypothetical neutrino is termed sterile with the other neutrinos being termed active by contrast.

The minimal extension that could be made would be to add one sterile neutrino to expand the PMNS matrix to be 4×4. This would increase the number of real parameters in the matrix to 16 of which 7 could be absorbed in the lepton fields leaving 9 free parameters; 6 rotation angles and 3 complex phases. The

large number of free parameters in this model requires simplifying assumptions to become phenomenologically useful. A search for evidence of sterile neutrinos forms the basis of this thesis and therefore a detailed description of extended models will be shown in Chapter 6.

2.4 Evidence For Neutrino Oscillations

As has been described above the neutrino was originally thought to be massless and therefore incapable of oscillations. It is currently believed that they have a small mass and undergo oscillations. Two problems in neutrino physics forced this change of paradigm; the Solar Neutrino Problem and the Atmospheric Neutrino Anomaly. Experiments performed in the last 2 decades have resolved these problems with the solution being universally accepted as neutrino oscillations.

2.4.1 Solar Neutrinos

The sun is powered by constant nuclear fusion reactions. These nuclear processes produce a flux of neutrinos that can be measured at the earth. This mainly takes place through the pp-chain(98%) with the only other significant contribution being the CNO-cycle. The net result of both processes is the conversion:

$$4p + 2e^- \rightarrow {}^4\text{He} + 2\nu_e + 26.731 \text{ MeV}$$
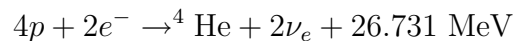
The energy released will be in the form of photons and kinetic energy of the neutrinos[8], with the average neutrino energy being 0.6 MeV. A break down of the neutrino energies due to the different reactions in the pp-chain and CNO-cycle is show as Figure 2.2.

---

[8]the kinetic energy of the ^{4}He nucleus can be ignored due to its large mass.
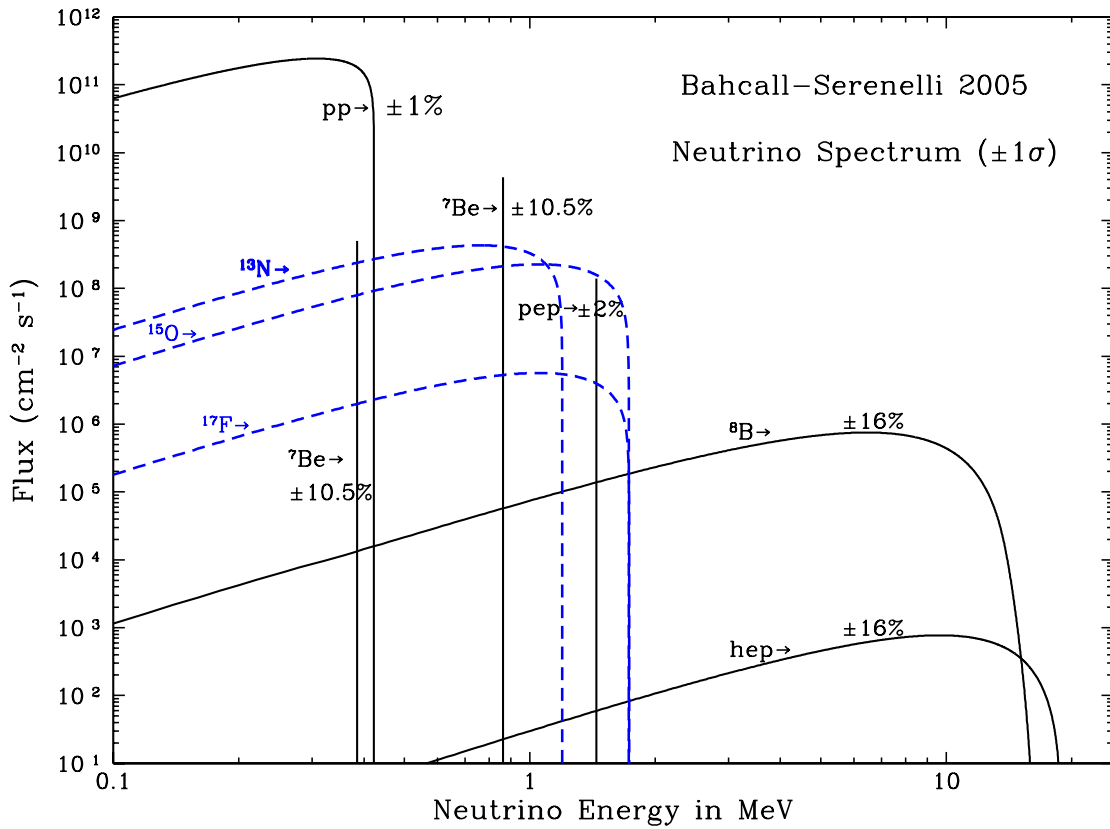
Figure 2.2: Energy spectra of solar neutrino fluxes. The black line shows the pp-chain reactions and the blue dashed lines the CNO-cycles. The Standard Solar Model (SSM) used is the BS05(OP). The neutrino fluxes from continuum sources are in units of $cm^{-2}s^{-1}MeV^{-1}$ and the line fluxes are given in $cm^{-2}s^{-1}$. Figure taken from [29].

Radio-chemical Experiments

The first observed problem with the neutrino model came with the flux of solar neutrinos. In a 1967 experiment at the Homestake Mine [30] using a larger version of the apparatus from his 1955 experiment and the slightly different interaction $\nu_e + {}^{37}\text{Cl} \rightarrow {}^{37}\text{Ar} + e^-$ Davis observed the flux of ν_e neutrinos from the sun. The threshold energy for this interaction is 0.814 MeV and therefore as can be seen from Figure 2.2 mainly detects neutrinos from the ${}^8\text{B}$ branch of the decay chain. The detector was in the Homestake Mine in South Dakota 1478 m below the surface. It was composed of a single steel tank with a volume of 600 kilolitres. To provide the chlorine 615 tons of C_2Cl_4 was dissolved in the tank. The argon was periodically chemically extracted and the radioactive argon counted, hence why this type of experiment is called radio-chemical. The measured neutrino flux was found to be significantly less (about a third) of what was predicted by the then current solar models The initial suspicion was that the model or experiment was incorrect but after 20 years of model refinement and taking data the so called "Solar Neutrino Problem" had not been resolved. The Solar Neutrino Problem was confirmed in the next generation of experiments which used gallium instead of chlorine as the interaction medium. These experiments make use of the reaction $\nu_e + {}^{71}\text{Ga} \rightarrow {}^{71}\text{Ge} + e^-$ which has a lower threshold of 0.233MeV and therefore as can be seen from Figure 2.2 allows neutrinos from all sources to be detected. In gallium experiments the ${}^{71}\text{Ge}$ produced by the neutrino interactions are extracted with chemical methods and detected in proportional counters as it decays back to ${}^{71}\text{Ga}$.

The first experiment to use Gallium was GALLEX[9] at the Gran Sasso National Laboratory in Italy. The detector consisted of 101 tons of liquid $GaCl_3$. GALLEX

---

[9]GALLium EXperiment

operated between 1991 and 1997 and was then replaced by GNO which used the same detector with a different germanium extraction technique. GNO[10] operated between 1998 and 2003. The GALLEX/GNO experiment measured about half the flux expected from the solar models. The final Gallium experiment was SAGE[11] which used 50 tons of liquid Gallium in the Baskan Neutrino Observatory in Russia. SAGE began taking data in 1990 and has consistently recorded a neutrino flux in agreement with GALLEX/GNO [31].

Water Cherenkov Detectors

Water Cherenkov detectors detect neutrinos by observing the Cherenkov light emitted in water from tracks created by relativistic charged leptons produced by neutrino interactions. The detector is a large tank of water surrounded by photo multiplier tubes to record the Cherenkov light. By knowing the precise time the light arrives at the PMTs interaction points and track directions can be determined. Water Cherenkov detectors have a threshold energy of a few MeV for detecting neutrinos and are therefore only really capable of detecting ^{8}B solar neutrinos. There have been 3 solar neutrino water Cherenkov experiments; Kamiokande[12], Super-Kamiokande and SNO[13].

Kamiokande was originally built to search for proton decay and is located 1 km underground in the Kamioka mine in Japan. It was upgraded in 1986 in order to be able to observe the ^{8}B solar neutrinos via the elastic scattering reaction $\nu_\alpha + e^- \rightarrow \nu_\alpha + e^-$. This interaction is mainly sensitive to ν_e as both NC and CC processes can contribute whereas ν_μ and ν_τ are NC only. The ν_e cross section for the process is therefore roughly 6 times larger than for ν_μ or ν_τ. Kamiokande

---

[10]Gallium solar Neutrino Observatory
[11]Soviet-American Gallium Experiment
[12]Kamioka Nucleon Decay Experiment
[13]Sudbury Neutrino Observatory

ran until 1996 when it was succeeded by a larger version of essentially the same experiment called Super-Kamiokande. This experiment increased the volume of water for solar neutrino interactions from 680 tons to 22.5 ktons. Both experiments measured the flux of ^{8}B solar neutrinos to be about half the flux expected from solar models in agreement with the radio-chemical experiments.

The latest water Cherenkov detector is SNO which is located 2092 m underground in the Creighton mine in Canada. It uses 1 kton of D_2O as the detection medium. The use of heavy water allows 3 different interactions to be observed. The CC interaction $\nu_e + d \rightarrow p + p + e^-$, the NC interaction $\nu_\alpha + d \rightarrow p + n + \nu_\alpha$ and the electron scattering process used in the H_2O water Cherenkov experiments $\nu_\alpha + e^- \rightarrow \nu_\alpha + e^-$.

SNO started in 1999 and has gone through 3 phases. Phase 1 used only the D_2O and lasted until 2001. Phase 2 added 2 tons of NaCl to the heavy water to increase the efficiency of neutron capture and thus aiding the measurement of the NC flux and ran until 2003. Phase 3 added ^{3}He proportional counter tubes to further increase the efficiency of neutron capture and further aid the NC measurement.

The main advantage SNO has over other experiments is that it can measure the total flux of neutrinos from all active flavours via the NC interaction. If the deficit in ν_e measured in previous experiments is due to flavour change we would expect the NC measurement in which all flavours contribute to agree with the solar model flux prediction. This is what is observed as can be seen from Figure 2.3 which is the result of phase 2 of the experiment.

This shows that the constraints from all 3 measurements coincide in a region consistent with neutrino flavour change.
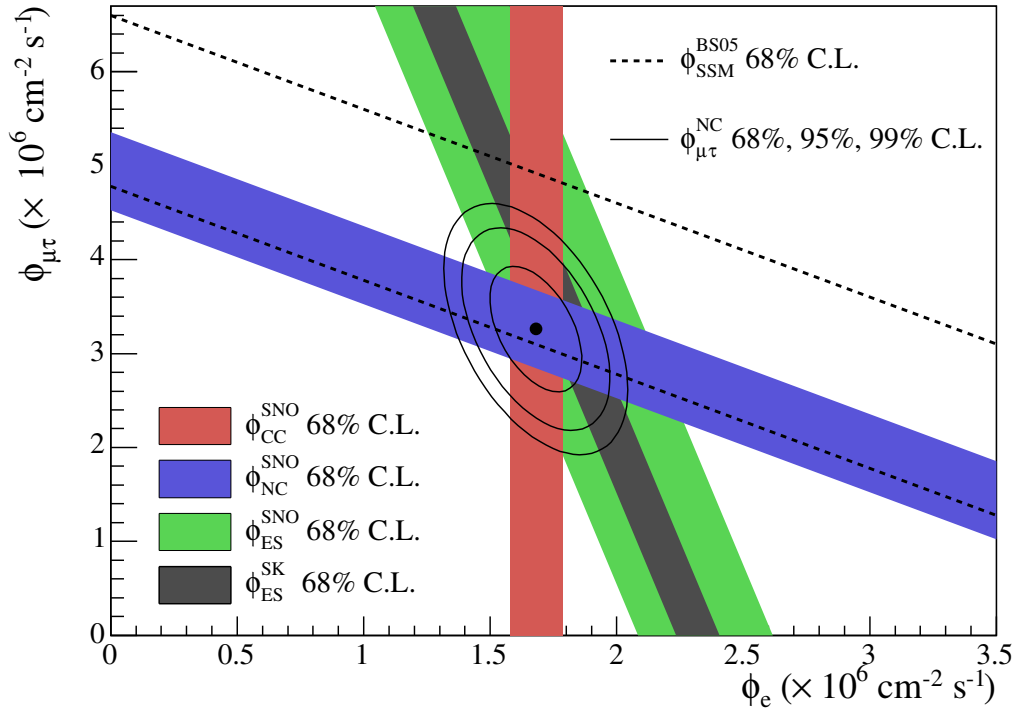
Figure 2.3: The flux ν_μ and $\nu_\tau (\phi_{\mu\tau})$ versus the flux of $\nu_e(\phi_e)$ as measured by the SNO experiment. The red area is the measured flux from ν_e CC interactions. The green area is the measured electron scattering flux. The grey area is the electron scattering flux measured by the Super-Kamiokande experiment. The blue area is the region where the $\nu_e + \nu_\mu + \nu_\tau$ fluxes sum to the total flux measured by the NC interactions. Dotted lines show the region from the total predicted solar neutrino flux predicted by SSM . Figure taken from [32].
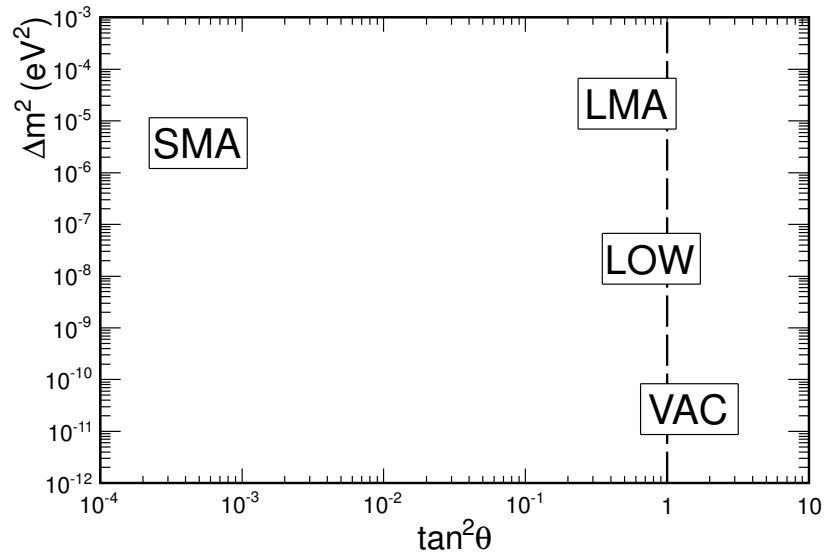
Figure 2.4: The possible values of the solar mixing parameters. The dashed line represents maximal mixing.

2.4.2 Neutrino Oscillations Solution to the Solar Neutrino Problem

The experimental evidence clearly shows a deficit in solar ν_e reaching the earth compared to that predicted by solar models. Unsuccessful attempts were made to adjust the solar models to agree with observed fluxes until the SNO results showed that flavour conversion took place between solar neutrinos. The most probable explanation for this flavour conversion is neutrino oscillation with competing theories such as neutrino decay and decoherence being disfavoured. There were several different allowed sets of oscillation parameters. The most likely at the time was the Large Mixing Angle (LMA; $\Delta m^2 \sim 7 \times 10^{-5} \mathrm{eV}^2, \tan^2 \theta \sim 0.4$) solution but other possibilities included the low mass (LOW;$\Delta m^2 \sim 8 \times 10^{-8} \mathrm{eV}^2, \tan^2 \theta \sim 0.7$) , the small mixing angle (SMA; $\Delta m^2 \sim 5 \times 10^{-6} \mathrm{eV}^2, \tan^2 \theta \sim 5 \times 10^{-4}$) and vacuum (VAC;$\Delta m^2 \sim 5 \times 10^{-10} \mathrm{eV}^2, \tan^2 \theta \sim 1.8$) oscillations solutions. The relative sizes of these oscillation parameters is shown in Figure 2.4

The VAC solution is the simplest and relies on neutrino oscillations in vacuum alone. The LMA, SMA and LOW are solutions of neutrino oscillations in matter.

Matter Effects

Lincoln Wolfenstein first noticed that neutrino oscillation probabilities could be significantly altered by propagating through matter [33]. Stanislav Mikheyev and Alexei Smirnov [34] later built on this work and helped apply its conclusions to neutrinos produced in the sun. A neutrino propagating in matter will be subject to an extra potential due to the coherent forward scattering of the neutrino from particles in the matter. Scattering can take place off electrons and nucleons, in the former case only for ν_e via a CC interaction and for the latter all flavours via an NC interaction. Thus the additional potential will depend on the density of the matter in which the neutrino is propagating. This is termed the MSW effect. A full treatment of matter effects is beyond the scope of this thesis and is mentioned only in passing as an explanation for the Solar Neutrino Problem. In a 2 flavour approximation neutrinos propagating in the presence of matter experience an effective mass splitting and mixing angle [23]. The effective squared-mass difference is given by:

$$\Delta m_M^2 = \Delta m^2 \sqrt{\left(\cos 2\theta - \frac{2\sqrt{2}EG_FN_e}{\Delta m^2} \right)^2 + \sin^2 2\theta)} \qquad (2.19)$$

and the effective mixing angle given by:

$$\sin^2 2\theta_M = \frac{\sin^2 2\theta}{\left(\cos 2\theta - \frac{2\sqrt{2}EG_FN_e}{\Delta m^2} \right)^2 + \sin^2 2\theta} \qquad (2.20)$$

Where G_F is the Fermi coupling and N_e is the electron density. This means there is a resonance condition when $\Delta m_{32}^2 \cos 2\theta = 2\sqrt{2}EG_FN_e$ which results in

maximal mixing, leading to the possibility of total transitions between the two flavours.

Vacuum oscillations are only dependent on the squared mass difference and therefore cannot say anything about the direction of the splitting. The resonance condition contains the sign of the mass splitting. This means that matter effects can determine the hierarchy of the neutrino mass eigenstates. The direction of the mass splitting in the solar sector is determined with $\nu_2 > \nu_1$. The direction of the mass splitting Δm_{32}^2 between ν_3 and $\nu_1 \approx \nu_2$ is still not experimentally determined. The case that $\nu_3 \gg \nu_1 \approx \nu_2$ is termed Normal Hierarchy. The situation with $\nu_3 \ll \nu_1 \approx \nu_2$ is called Inverted Hierarchy. The direction of this splitting is an ongoing area of research.

In the case that the medium of propagation has a constant density then the oscillation probability is given by Equation 2.18 with the effective mass-splitting and mixing angle from Equations 2.19 and 2.20. If the density profile is more complicated than this then a host of effects can be seen. In the particular case of the sun the electron density is greatest at its core and drops smoothly. Neutrinos created in the core of the sun are therefore produced in an almost entirely ν_{2m} state as with very high electron density the mixing angle tends to 0 as can be seen from Equation 2.19 and the mass and flavour states therefore become almost coincident. If the change of density is gradual enough the neutrinos stay as ν_{2m} as θ_m approaches θ at the point the neutrinos enter the vacuum of space at which point they are in the ν_2 state. They then propagate to earth in this ν_2 state without oscillating and are consequently a mixture of all neutrino flavours when detected explaining the ν_e deficit.

As can be seen in Figure 2.5 the radiochemical experiments excluded much of the parameter space but left small areas that satisfy the VAC, LMA, SMA

and LOW solutions. If the deficit was due to oscillations in vacuum it would be expected that there would be a seasonal variation in the solar flux measured as the earth moved nearer and further from the sun. As no such effect has been seen the vacuum solution is disfavoured.

The water Cherenkov experiment data provided additional information and excluded much more parameter space. These experiments allowed the energy spectrum of the neutrinos to be measured. The shape of the spectrum is effected by the size of the mixing angle due to the matter effects described above. Therefore by comparing differences in the expected spectrum from SSMs with the measured spectra the size of the mixing angle can be refined. The water Cherenkov experiments measured only a small distortion in the predicted spectrum excluding the SMA model which would require different oscillation probabilities at different energies. If the mixing parameters are right there can be a regeneration of solar ν_e as they travel through the earth. As the solar neutrinos have to travel a greater distance through the earth at night than during the day the Water Cherenkov detectors were able to show there was no day-night asymmetry in the measured flux reducing the available parameter space to only two small areas corresponding to the LMA and LOW solutions with LMA being favoured.

Liquid Scintillator Experiment

The final experiment relevant to the solar neutrino sector is KamLAND[14]. KamLAND was a 1 kton liquid scintillator detector in the old Kamiokande cavity in the Kamioka mine. In contrast to the other experiments discussed above KamLAND does not detect neutrinos from the sun but rather ν_e with a terrestrial source to confirm the results of the solar neutrino experiments. It was designed

---

[14]Kamioka Liquid Scintillator Anti-Neutrino Detector
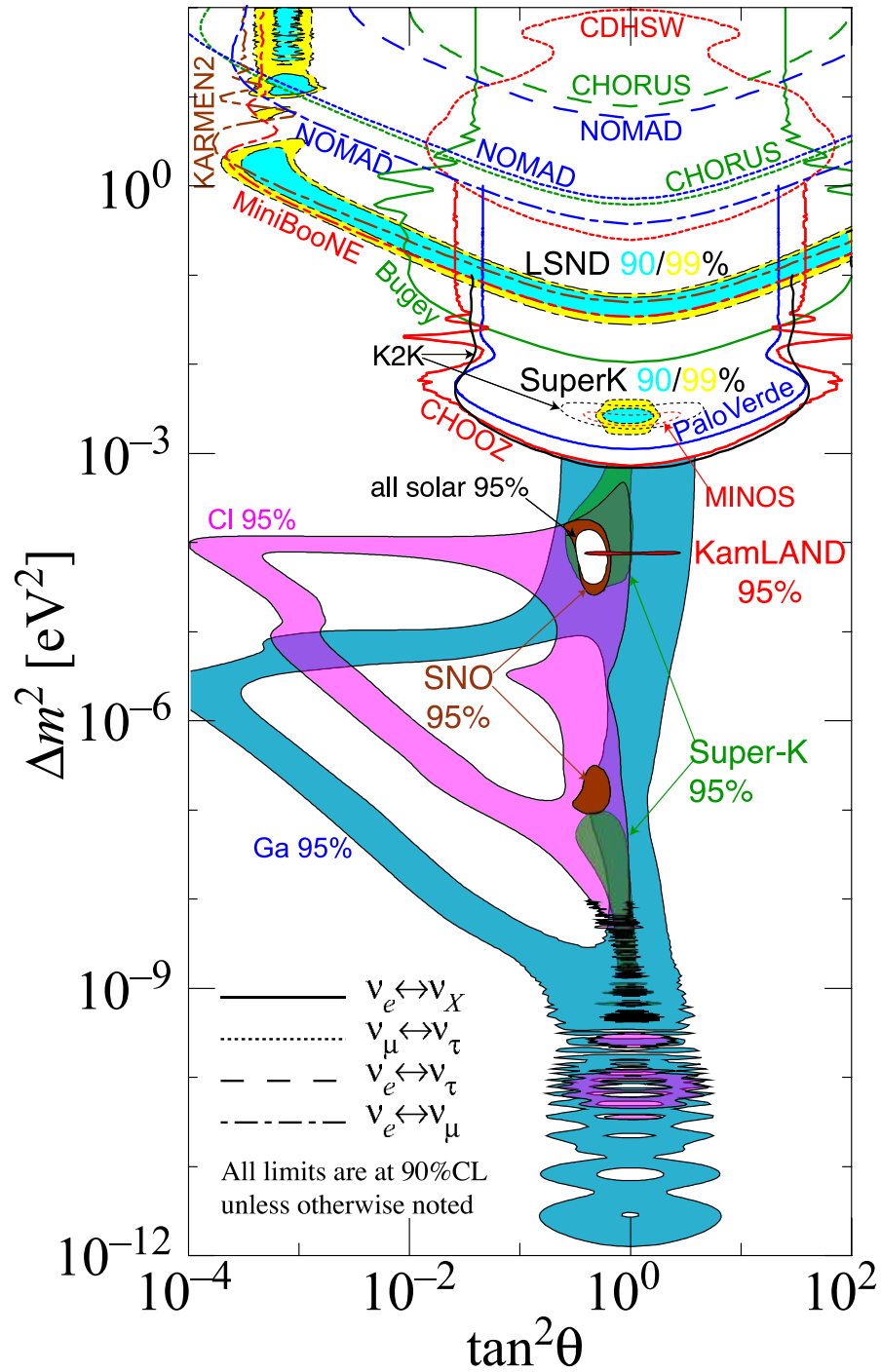
Figure 2.5: The regions of mass splitting and mixing angle favoured or excluded by all experiments up to 2008. Filled areas represent allowed regions. Lines are exclusion limits. Figure taken from http://hitoshi.berkeley.edu/neutrino/
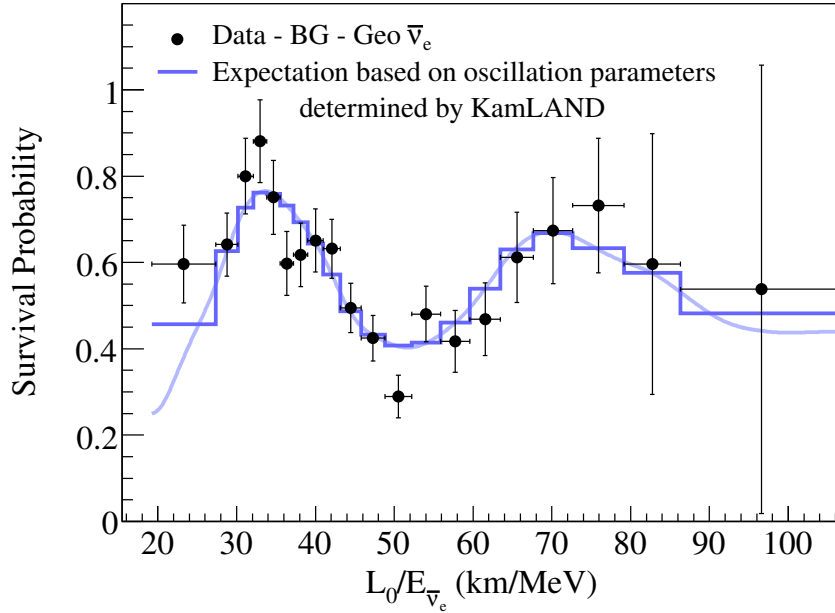
Figure 2.6: The ratio of measured $\overline{\nu}_e$ to the no-oscillation expectation as a function of distance travelled/energy in the KamLAND experiment. Black dots show data. The blue line shows the best fit to oscillations. Figure taken from [35]

to detect $\overline{\nu}_e$ produced by nuclear reactors all over Japan with an average distance of 180 km by the inverse β-decay $\overline{\nu}_e + p \rightarrow n + e^-$. It was designed so that it could measure the same oscillations[15] as solar neutrinos with the LMA solution. KamLAND reported that the measured $\overline{\nu}_e$ spectrum to be undistorted by oscillations is excluded at $> 5\sigma$ [35]. In addition the measured energy spectrum shown in Figure 2.6 clearly shows an energy dependent deficit of events which is a clear signature of neutrino oscillations.

The KamLAND experiment does not suffer from matter effects due to its short baseline and was therefore able to give a much more precise measurement of the mass splitting than the solar experiments. The parameter space available is now extremely small as can be seen in Figure 2.5. A combined analysis of all solar neutrino data and KamLAND leaves only the LMA solution with best fit

---

[15]Assuming CPT conservation

parameters of [36]:

$$\Delta m_{21}^2 = 8.0^{+0.6}_{-0.4} \times 10^{-5} \text{eV}^2 \tag{2.21}$$

$$\theta_{12} = 33.9^{\circ +2.4}_{-2.2} \tag{2.22}$$

Future Experiments

The solar neutrino problem has essentially been solved. Future progress should determine the oscillation parameters more precisely and search for non-standard physics such such as sterile neutrinos. More precise measurements of the NC flux at SNO phase 3 and measurements of the pp flux from the pp-chain will improve measurements of the mixing angle.

Further tests of the SSM will be made by trying to measure the flux from other parts of the pp chain with lower energy such as the mono-energetic ^{7}Be and the pp flux. To measure such low energy neutrinos will require the use of low background liquid scintillator detectors such as Borexino. Borexino has recently published it's first results showing agreement with the LMA [37] solution and showing confirmation of the MSW effect in the transition between matter and vacuum oscillations. A similar liquid scintillator experiment is designed to replace SNO. It is termed SNO+ and is under construction at the time of writing [38].

2.4.3 Atmospheric Neutrinos

Comsic rays interact with particles in the upper atmosphere. One of the most abundant particles produced in these interactions is pions. These decay almost exclusively into muon and muon neutrinos $\pi \rightarrow \mu + \nu_\mu$. Cosmic ray interactions therefore produce a flux of neutrinos termed atmospheric neutrinos. Additional

muons can be created by high energy kaons. The muons which decay before reaching the earth will decay into electrons and 2 neutrinos $\mu \rightarrow e + \nu_e + \nu_\mu$. The neutrinos produced by these processes are called atmospheric neutrinos. The decay channels lead to the conclusion that for muons at low enough energy to decay before reaching the ground $E \simeq 1$ GeV the flux ratios should be:

$$R = \frac{\phi_{\nu_\mu} + \phi_{\overline{\nu}_\mu}}{\phi_{\nu_e} + \phi_{\overline{\nu}_e}} \approx 2 \qquad (2.23)$$

At energies higher than 1 GeV more muons reach the ground before decaying resulting in fewer ν_e neutrinos being produced and consequently an increase in R. Calculations of atmospheric fluxes can be very detailed taking into account many factors. The measurement of the ratio is complicated by the fact that experiments do not measure the neutrinos directly but the charged lepton that is associated with them. Electron and muon neutrinos have different cross-sections and detection efficiencies and thus the experimental results to search for the atmospheric neutrino anomaly are usually expressed as the double ratio

$$R = \frac{R_{data}}{R_{MC}} \qquad (2.24)$$

Where R_{data} and R_{MC} are defined as in Equation 2.23. Atmospheric ν_μ were first recorded in 1965 in scintillator experiments in mines in India [39] and South Africa [40]. These experiments showed a deficit in the ratio of expected ν_μ but with large uncertainties. In the late 1980s large underground water Cherenkov detectors were built. These were primarily built to search for nucleon decay but an important background were events due to atmospheric neutrinos. In trying to measure these backgrounds Kamiokande (described in the section above in the

context of solar neutrinos) [41] and the IMB[16] [42] experiment measured a deficit of atmospheric ν_μ leading to what became known as the Atmospheric Neutrino Anomaly. This was initially controversial as 2 fine grained iron tracking detector experiments NUSEX[17] [43] and Frejus [44] saw no such deficit. In addition IMB only saw a deficit for sub-1.5 GeV contained ν_μ events and not for higher energies. Further experimental evidence of a deficit was provided when two more iron tracking detector experiments MACRO[18] in 1995 [45] and Soudan-2 in 1997 [46] measured a smaller than expected flux of atmospheric neutrinos.

Neutrino oscillations were considered a likely candidate as a solution of the Atmospheric Neutrino Anomaly. The experimental breakthrough in showing this came from the observation of an up-down asymmetry of atmospheric neutrino events at the Super-Kamiokande detector (described previously). Neutrinos arriving from the top of the detector have only travelled 20 km before detection. Those arriving from below will have travelled through the entire diameter of the earth before being detected. The variation in neutrino flux as a function of zenith angle was first shown by Kamiokande [47] and confirmed by Super-Kamiokande [48]. A water Cherenkov detector can distinguish muons and electrons by the cleanliness of the signal they leave. Electrons shower as they travel through the water resulting in diffuse rings of Cherenkov light. Muons do not shower and therefore produce cleaner rings. The direction of the incoming neutrino is closely correlated with the direction of the lepton.

An improved analysis binning the ν_μ flux as a function of L/E [49] for high resolution events was performed and confirmed the oscillation hypothesis. As can be seen in Figure 2.7 the predicted flux and the data agree well up until

---

[16]Irvine-Michigan-Brookhaven
[17]NUcleon Stability EXperiment
[18]Monopole, Astrophysics and Cosmic Ray Observatory
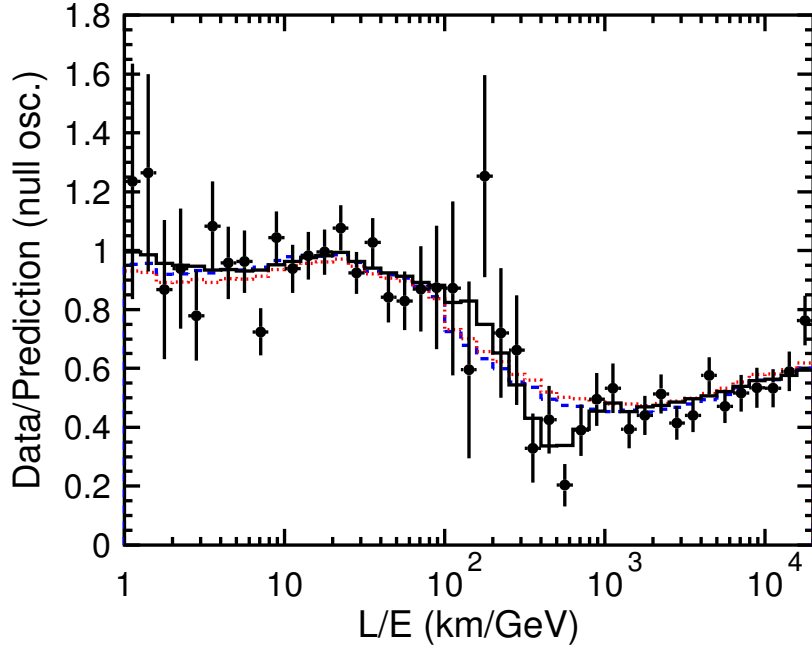
Figure 2.7: Ratio of the data to the MC prediction without neutrino oscillations as a function of reconstructed L/E in the Super-Kamiokande detector. The points show the data. The solid black line the prediction with $\nu_\mu \leftrightarrows \nu_\tau$ oscillations. The blue dashed line shows the best fit for neutrino decay and the red dotted line the best fit for neutrino decoherence. Figure taken from [49].

$L/E \gtrsim 10^2$ kmGeV^{-1} when flavour transitions begin to take place. Included in this plot are fits to 2 other possible explanations for the Atmospheric Anomaly namely neutrino decay and decoherence. The figure shows both are disfavoured compared to oscillations.

The Super-Kamiokande collaboration have recently refitted the entire data from the first running period [50]. Figure 2.8 shows the flux of ν_e and ν_μ in the Super-Kamiokande detector.

There is a clear deficit of ν_μ which is energy dependent and corresponds well to the oscillation model. The measured flux of ν_e agrees well with the prediction. This would suggest that the oscillations are $\nu_\mu \rightleftarrows \nu_\tau$ and not $\nu_\mu \rightleftarrows \nu_e$. This is in agreement with the results of reactor experiments of appropriate baselines which have excluded the $\nu_\mu \rightleftarrows \nu_e$ oscillation channel.
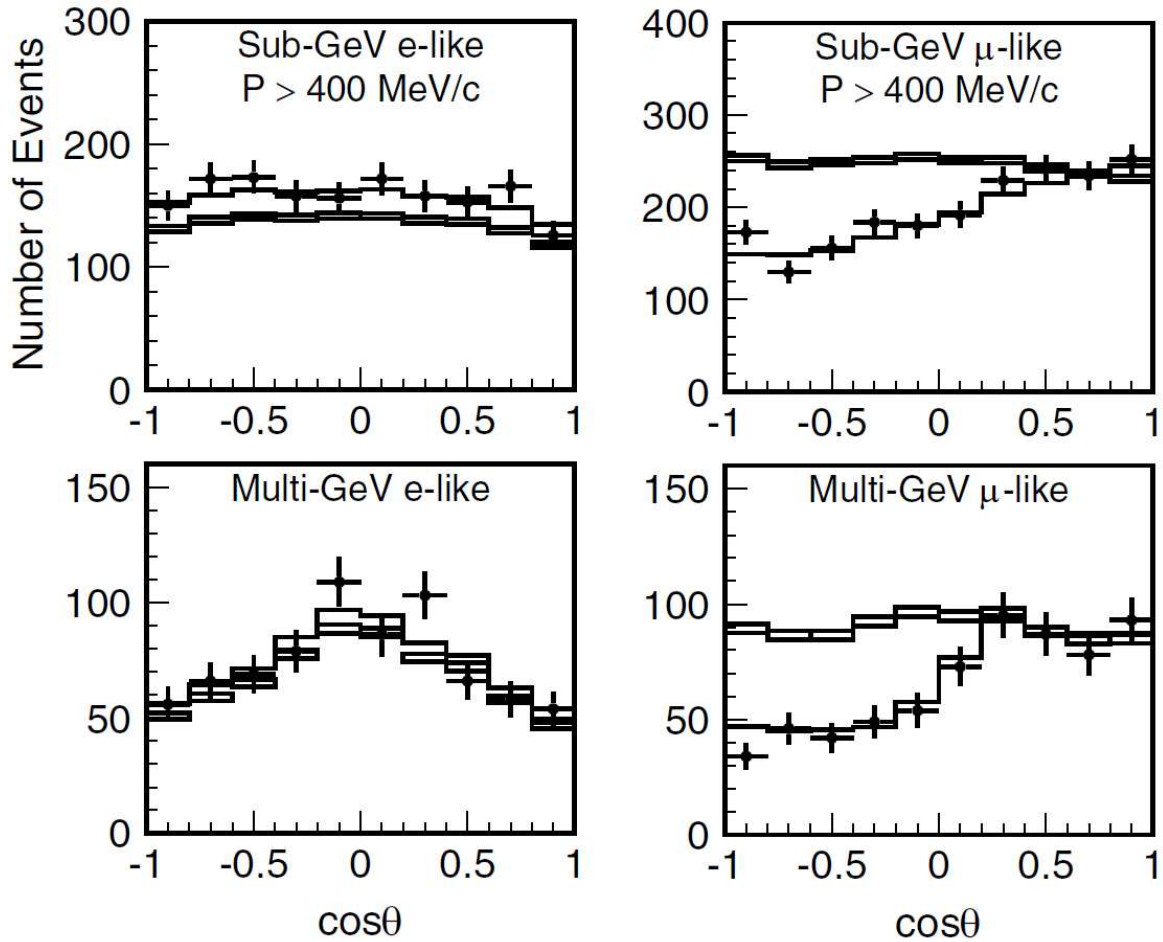
Figure 2.8: The distribution of electron and muon events as a function of zenith angle measured by Super-Kamiokande. In all figures the data is shown by the points. The black line shows the best fit for $\nu_\mu \leftrightarrows \nu_\tau$ oscillations. The boxes show the unoscillated MC prediction. The size of the box indicates the statistical error. The top 2 figures show the result for low energy events. The bottom 2 for higher energy events. The left 2 figures show the result for electron events. The right 2 figures show the result for muon events. Figure taken from [50].

Terrestrial Atmospheric Experiments

As in the case of the solar neutrino sector experiments have been built creating a neutrino beam that explores the parameter space of the atmospheric sector. The K2K[19] experiment created an almost pure beam of ν_μ at the KEK laboratory and detected them after a 250 km propagation in the Super-Kamiokande detector described earlier. The neutrinos produced have an average energy of 1.3GeV and are therefore sensitive to the atmospheric neutrino sector. The K2K experiment makes use of a smaller but similar detector at the production point. Comparison of the measurements made with this detector with the Super-Kamiokande detector measurement showed a deficit of expected neutrino events. The total number of data events recorded was 112 with an unoscillated expectation of $158.1^{+9.2}_{-8.6}$. The expected number of events in the presence of oscillations was 107.2. The observed energy spectra showed the characteristic energy dependency of ν_μ disappearance indicative of oscillations [51].

The MINOS experiment on which this thesis is based uses a very similar experimental design and will be described in detail in the next chapter.

The results of the atmospheric experiments described are all consistent with each other. The allowed regions of parameter space for the most accurate can be seen in Figure 2.5. The current accepted values for the atmospheric oscillation parameters at 90% confidence limit are [25]:

$$1.9 \times 10^{-3} \text{ eV}^2 < \Delta m^2_{32} < 3.0 \times 10^{-3} \text{ eV}^2 \tag{2.25}$$

$$\sin^2(2\theta_{23}) > 0.92 \tag{2.26}$$

---

[19]KEK to Kamioka

2.4.4 θ_{13} Mixing Angle

The final mixing angle in the 3 flavour oscillation model is the angle θ_{13}. One of the ways this can be observed is $\nu_\mu \rightleftarrows \nu_e$ oscillations at the atmospheric mass splitting. Examination of beams of ν_μ will mainly result in ν_μ disappearance as they oscillate to ν_τ. However sub dominant oscillations of ν_μ to ν_e can result in excess ν_e detection. Reactor experiments are well suited in terms of L/E to measure this effect.

As was mentioned when discussing the Super-Kamiokande experiment limits from short distance neutrino oscillations at reactor experiments have shown that θ_{13} is small. The best limit on θ_{13} comes from the CHOOZ experiment in France. CHOOZ looked for disappearance of $\overline{\nu}_e$ over a baseline of $\sim$ 1km from the Chooz nuclear reactor by inverse neutron decay $\overline{\nu}_e + p \rightarrow n + e^+$ in a 5 ton liquid scintillator detector loaded with gadolinium to aid in neutron capture. The rate and shape of the measured energy spectrum was in agreement with no oscillations demonstrating that the atmospheric oscillations were due to $\nu_\mu \leftrightarrows \nu_\tau$ and not $\nu_\mu \leftrightarrows \nu_e$ oscillations.

This allowed the CHOOZ experiment to set a 90% Confidence Limit (C. L.) limit on the value of θ_{13} as: [52]

$$\sin^2(2\theta_{13}) < 0.19 \tag{2.27}$$

This limit is a function of the atmospheric mass splitting Δm^2_{32} with the above being the value obtained when $\Delta m^2_{32} = 1.9 \times 10^{-3}$ eV^2 from Equation 2.26 which gives the largest possible limit consistent with the measured values of Δm^2_{32} [25].

An alternative way to measure the value of θ_{13} is by looking for $\nu_\mu \rightleftarrows \nu_e$ oscillations at the atmospheric mass splitting by searching for ν_e appearance. The

MINOS experiment on which this thesis is based and will be discussed in the next chapter is capable of making such a measurement.

Future Long Baseline Experiments

Several experiments are planned or in the early stages of data taking that will improve the knowledge in the atmospheric sector. As well as more accurately measuring the atmospheric parameters, these new experiments will also measure the θ_{13} mixing angle.

First are the long baseline experiments searching for $\nu_\mu \rightleftarrows \nu_e$ oscillations. The T2K[20] experiment in Japan will send a beam of neutrinos from the J-PARC accelerator in Tokai 295 km to the Super-Kamiokande detector at Kamioka. In this experiment the detector will be very slightly off-axis $\sim 2°$. This will result in an almost monochromatic neutrino flux.

The T2K experiment recently announced it had detected the first neutrino event within the detectors. The NOνA [21] experiment will have baseline of 800 km and use the same neutrino beam as MINOS although it will again be off-axis and addtionally will use liquid scintillator detectors. Due to the increased baseline NOνA can also use matter effects to determine the sign of Δm_{32}^2 and therefore determine the neutrino mass hierarchy.

As these experiments rely on ν_e appearance in addition to measuring θ_{13} they are sensitive to the CP violating phase δ and hope to measure this as well.

As has been shown above the atmospheric oscillation is suspected to be $\nu_\mu \rightarrow \nu_\tau$ but this has never been explicitly detected. The OPERA[22] experiment is looking for ν_τ appearance making use of the CNGS neutrino beam over a base line of

---

[20]Tokai to Kamioka

[21]NUMI Off-axis ν_e Appearance

[22]Oscillation Project with Emulsion Tracking Apparatus

732 km. To observe the short tracks left by the τ lepton appearance and decay OPERA is built of high resolution interweaved layers of emulsion and lead plates. The experiment is currently taking data.

A next generation reactor experiment to measure θ_{13} by $\overline{\nu}_e$ disappearance is also in production. It will replace the CHOOZ experiment and because it has 2 detectors with different base lines will be know as double CHOOZ. The neutrinos will be detected in liquid scintillator loaded with Gadolinium. Double CHOOZ will hope to either measure θ_{13} or improve the 90% C. L. by an order of magnitude to $\theta_{13} < 0.03$. Further planned experiments in this sector include Daya Bay [53] and RENO [54].

2.4.5   LSND Mass Splitting

As previously mentioned almost all the experimental evidence is in agreement with there being 3 flavours of neutrino and therefore 2 mass splittings. The exception being the result of the LSND[23] experiment. LSND differs from the experiments so far described in that it searches for the appearance of a neutrino from oscillations rather than a disappearance. In particular LSND searches for $\overline{\nu}_e$ appearance from $\overline{\nu}_\mu \rightleftarrows \overline{\nu}_e$. The neutrinos originate with a proton source incident on a target which produces a large number of pions. The $\overline{\nu}_\mu$ then come from the decays $\pi^+ \rightarrow \mu^+ + \nu_\mu$ and subsequent $\mu^+ \rightarrow e^+ + \nu_e + \overline{\nu}_\mu$. These decay chains are lacking in $\overline{\nu}_e$ which can then be searched for by the interaction $\overline{\nu}_e + p \rightarrow e^+ + n$ which has a large and well know cross section. The detector consists of a 5.7 m diameter by 8.3 m long cylindrical tank containing liquid scintillator at low concentration to allow the detection of scintillator and Cherenkov light. The $\overline{\nu}_e$ are identified over a baseline of $\sim$ 30 m by recording the e^+ from the $\overline{\nu}_e$ interaction as well as the 2.2 MeV

---

[23]Liquid Scintillator Neutrino Detector

photons from $np \to d\gamma$. In addition the small flux of ν_e allows for the possibility of a similar search for $\nu_\mu \rightleftarrows \nu_e$ oscillations.

The LSND experiment saw a significant excess of $\overline{\nu}_e$ events above the background of $87.9 \pm 22.4 \pm 6.0$. The results were consistent with oscillations with a mass splitting of between $0.2 - 10$ eV^2 [27]. This splitting is significantly larger than that found for solar and atmospheric neutrinos.

Further experiments such as NOMAD[24] [55] and Bugey [56] have tested the same parameter space and imposed constraints as can be see in Figure 2.5. In particular KARMEN[25] performed a similar experiment over a shorter baseline $\sim$ 18m and saw no such excess [57]. This excluded a large portion of the parameter space available for the LSND oscillation as shown in Figure 2.9. MiniBooNE is the latest experiment to attempt to verify the LSND result. MiniBooNE makes use of protons from the Booster at the Fermilab accelerator complex to create a beam of primarily ν_μ via pion decay detected in a spherical tank of liquid scintillator. Depending on the charge of the pions focused will result in either a flux of ν_μ or $\overline{\nu}_\mu$ and the oscillation search will be by looking for an excess of ν_e or $\overline{\nu}_e$. Under the assumption of CPT invariance the neutrino analysis should be the same as the anti-neutrino and the LSND result.

As can be seen in Figure 2.9 the ν_μ analysis excludes almost the entire LSND allowed region for 2 flavour oscillations [58]. In addition the neutrino analysis saw an unexplained excess of low energy ν_e. Models to reconcile this MiniBooNE result and excess ν_e involving sterile neutrinos and Lorentz violation have been explored. The recent $\overline{\nu}_e$ analysis [59] has found no evidence of an excess of $\overline{\nu}_e$ at any energies but does not exclude the LSND result due to low statistics as shown in Figure 2.9. A higher statistics analysis is expected in the coming years.

---

[24]Neutrino Oscillation MAgnetic Detector
[25]KArlsruhe Rutherford Medium Energy Neutrino
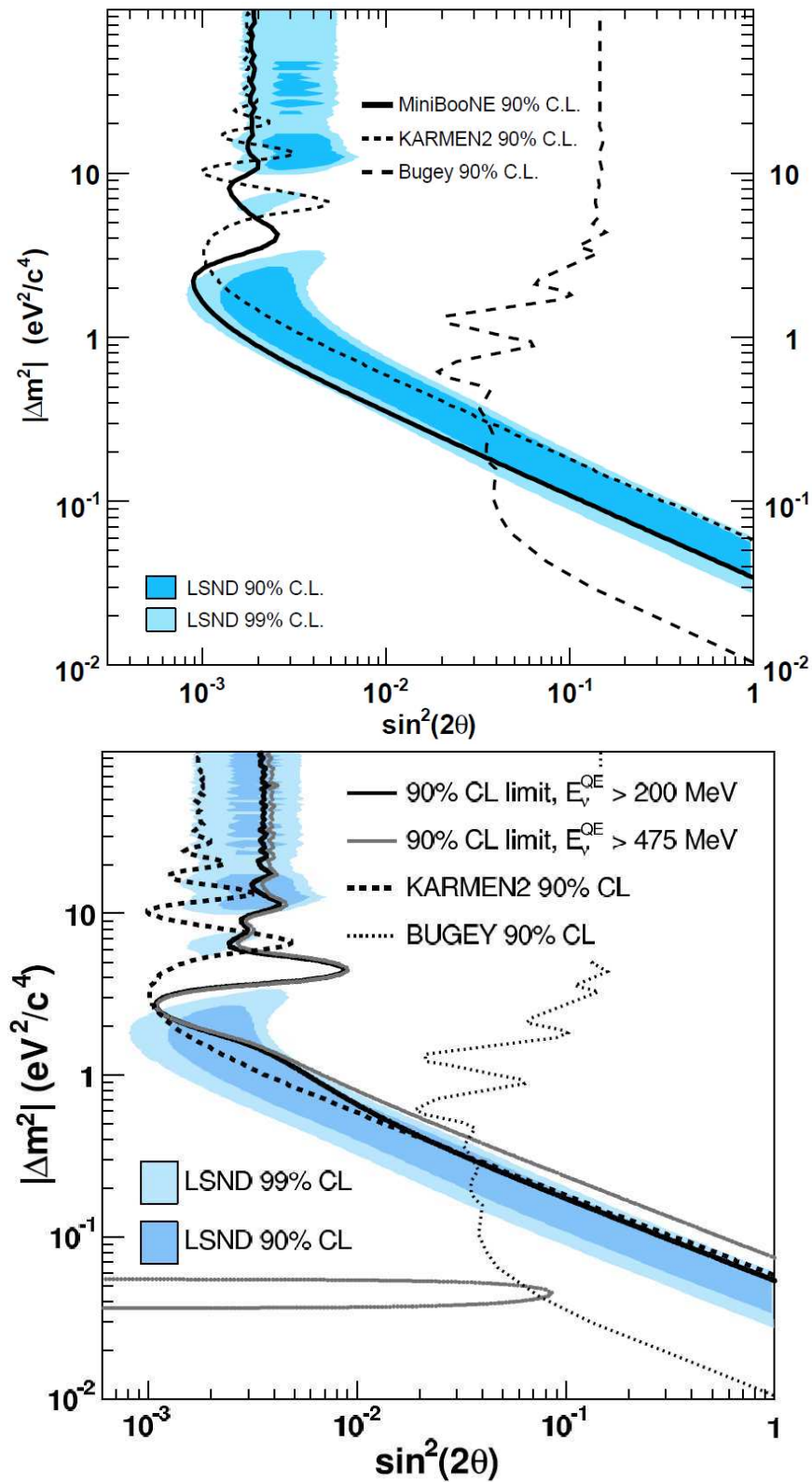
Figure 2.9: The LSND allowed regions and the MiniBooNE, KARMEN and Bugey 90% C.L. are shown for both neutrinos on the top and antineutrinos on the bottom. The 90% allowed region is in dark blue and the 99% region in light blue. The MiniBooNE, KARMEN and Bugey 90% C. L. are labelled. In the antineutrino plot the 2 MiniBooNE lines are different energy ranges for neutrinos considered in the analysis. Top plot from [58]. Bottom plot from [59].

Chapter 3

The MINOS Experiment

3.1 Overview of the MINOS Experiment

MINOS stands for Main Injector Neutrino Oscillation Search and is a long-baseline neutrino oscillation experiment. It makes use of an intense mainly muon-neutrino beam produced by the NuMI facility at the Fermilab near Chicago, Illinois. It searches for neutrino oscillations by the use of 2 detectors; the Near Detector at ~ 1 km propagation distance and the Far Detector 735 km away.

Using the data collected in the Near Detector a prediction of the energy spectrum of neutrinos that is expected at the Far Detector can be made. This prediction can then be compared with the actual neutrino energy spectrum measured at the Far Detector. If the prediction and measured neutrino energy spectra disagree, a fit to an oscillation model can be performed to determine the oscillation parameters. The two detectors are as identical as is practical to reduce common systematic uncertainties.

3.2 NuMI Beam

The NuMI[1] beamline makes use of 120 GeV protons provided by the Main Injector at Fermilab. The protons arrive in a spill of 5 or 6 batches with a minimum repetition rate of 1.9 s. In the case where MINOS receives only 5 batches the spill is 8.7 μs long and the sixth batch is used to create antiprotons for use in the Tevatron collider. The typical number of protons contained in a spill is 25×10^{12}. The NuMI beam produces an average power of 400 kW. A more complete description of the NuMI beamline can be found in [60, 61].

The creation of the neutrino beam begins with the protons being directed onto a segmented water cooled graphite target. This results in the creation of a number of hadrons including many pions and kaons. These secondary mesons (mainly pions) are preferentially focused in the decay volume by the use of 2 magnetic focusing horns which create a toroidal field about the beam direction. The beam of focused pions and kaons then pass into 675 m long decay pipe angled 3.3° downwards to point at the Far Detector. For the first 2 years of the running time of MINOS (the period covered by this thesis) the decay pipe was a vacuum but recently has had helium added to prevent the decay pipe imploding due to the weakening caused by the beam. Within the decay pipe the neutrino beam is created from the decays $\pi^+/K^+ \rightarrow \mu^+ \nu_\mu$. Any mesons that have not decayed by the end of the decay pipe are stopped by a hadron absorber composed of aluminium, steel and concrete. Any muons that remain are then removed by 300 m of rock before the beam is incident on the Near Detector. The main components of the NuMI beamline are shown in Figure 3.1

A feature of the NuMI beamline is that the resulting neutrino energy spectrum is tunable by adjusting the relative position of the target and the horns.

---

[1]Neutrinos at the Main Injector
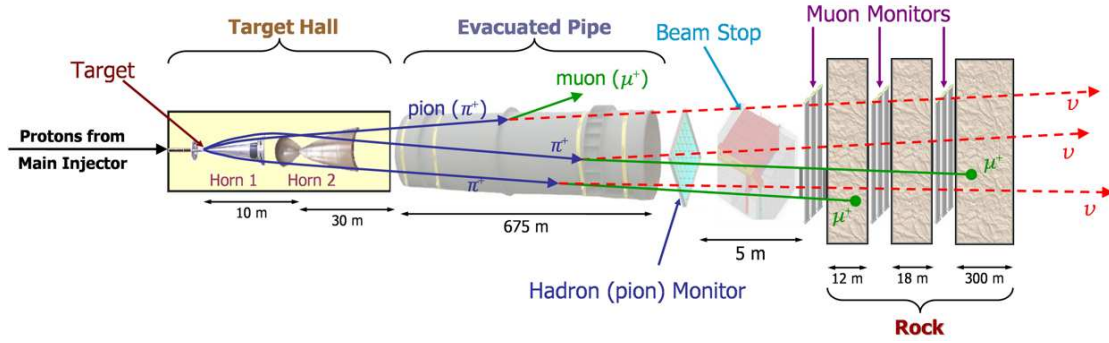
Figure 3.1: The NuMI beamline components.

This allows different energy mesons to be focused into the decay pipe resulting in different energy spectrum of neutrinos. Most of the MINOS data has been taken in the Low Energy (LE) configuration with small quantities of data taken with the position of the target adjusted relative to the horns and a higher current in the horns to provide the correct focusing. This produces neutrinos with a higher average energy than in the LE configuration. These configurations are referred to as Medium Energy (ME) and High Energy (HE) and are shown in Figure 3.2. Also shown in the Figure is the spectrum obtained when running in the Horn Off (HO) configuration. In this case the target is in the same place as the LE configuration but there is no current in the horns. There is therefore no focusing of decaying pions and consequently a large spread of neutrino energies.

The MINOS experiment has mainly taken data in the Low Energy beam configuration to maximise sensitivity to the oscillation parameters suggested by the results of the Super-Kamiokande experiment. The LE beam thus produced consists of 91.6% ν_μ with backgrounds composed of $\overline{\nu}_\mu(6.8\%)$ and $\nu_e + \overline{\nu}_e(1.6\%)$. These backgrounds are mainly due to wrong sign mesons that are travelling directly down the beam pipe and therefore not defocused by the magnetic field. There is also a smaller contribution from μ^+ decay.

The magnetic horns can focus either positive or negative pions allowing either
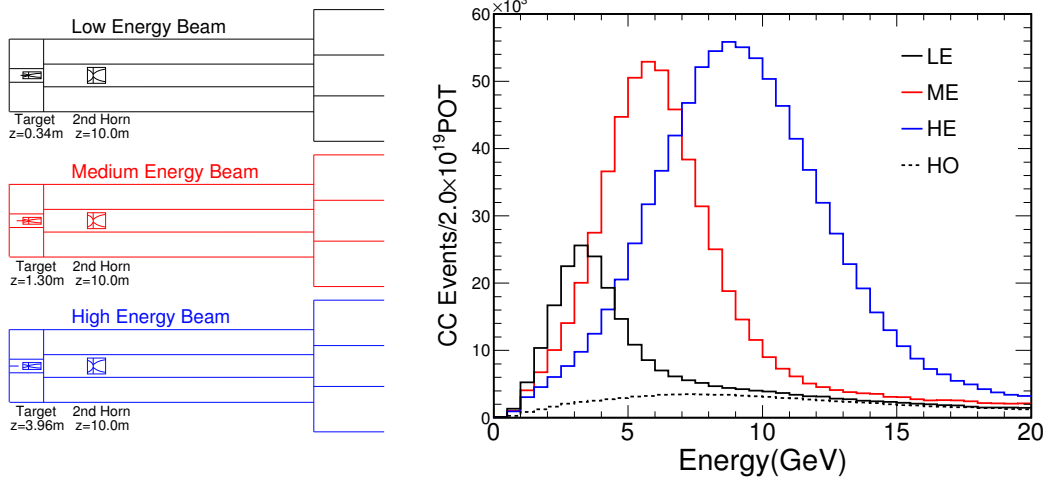
Figure 3.2: The relative positions of the target and horns and the resulting energy spectra seen at the Near Detector for Charged Current events. Low Energy Beam is in black, Medium Energy in red, High Energy in blue and Horn Off in dashed black.

a ν_μ or $\overline{\nu}_\mu$ beam to be produced. MINOS recently changed from producing a ν_μ to a $\overline{\nu}_\mu$ beam.

3.3 Data Taking

The MINOS experiment has been taking NuMI beam data since March 2005. At the time of writing it has accumulated $\sim 8.5 \times 10^{20}$ Protons on Target (POT) in 4 distinct run periods. This can be seen in Figure 3.3.

Run Period I ran until the summer of 2006. The first month of data taking used the LE, ME and HE configurations with the rest of the run being LE with 2 short periods using a different horn current. The two short periods of data taking over the summer of 2006 are HE. Run period II ran from Autumn 2006 until the summer of 2007 exclusively in the LE configuration. Short periods of HO data were taken at the end of both Run Period I and Run Period II. Run Period III again used the LE configuration and began in November 2007 and took data up
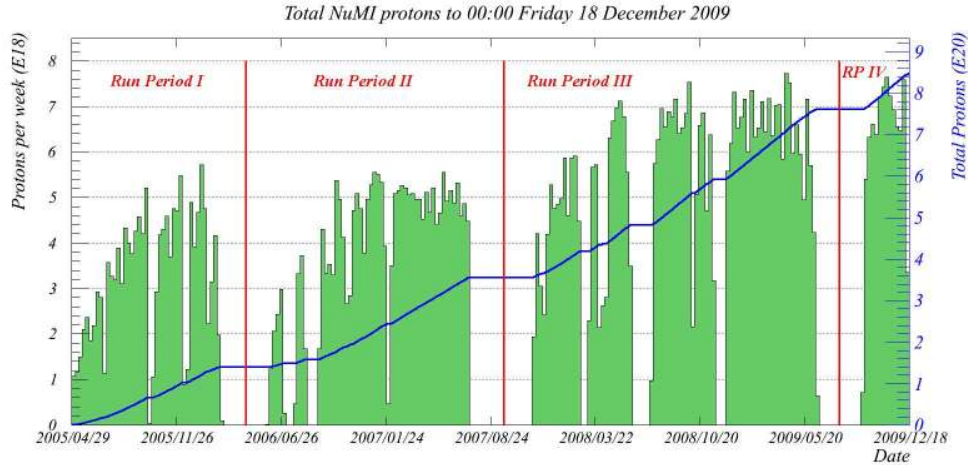
Figure 3.3: The Data Collected by the MINOS experiment up to December 2009. Green bars show the weekly amount of PoT collected. The blue line shows cumulative PoT. The Run Periods are separated by red lines.

until summer 2009. During this Run Period the decay pipe was filled with helium. Run Period IV began in Autumn 2009 and has reversed the field in the magnetic horns to investigate a $\overline{\nu}_\mu$ beam.

In this thesis only the Near Detector LE, ME, HE and HO data from Run Periods I and II are used. In addition only data collected in the LE configuration with a horn current of 185 kA is used. For reasons that will be explained in Chapter 5 only LE Far Detector data is used. This is summarised in Table 3.1.

3.4   Minos Detectors

As stated above the MINOS detectors are as identical as possible and share much common technology. The differences that are necessary are due to the different interaction rates in the detectors. The Near Detector sees approximately 10 neutrino interactions in every spill whereas the Far Detector sees only a few events per day. The Far Detector is located 705 m underground in a purpose built cavern in the Soudan Mine in northern Minnesota with a shielding of 2070 meters-water-

Beam Configuration	Target Position (cm)	Horn Current (kA)	Near Data Collected (10^{18} POT)	Far Data Collected (10^{18} POT)
LE RunI	10	185	125.1	124.0
LE RunII	10	185	165.3	193.9
LE Total	10	185	290.4	317.9
ME	100	200	1.13	n/a
HE	250	200	16.0	n/a
HO RunI	010	000	2.77	n/a
HO RunII	010	000	2.39	n/a
HO Total	010	000	5.16	n/a

Table 3.1: The data recorded in the LE, ME, HE and HO configurations in Run Period I and II used in this thesis.

equivalent. This is sufficiently far underground that the rate of cosmic muon and neutrino interactions is only ~ 0.5Hz. The Far Detector is therefore dominated by detector noise with a rate of ~ 5kHz. Thus the electronics and triggering requirements of the 2 detectors are very different as are the sizes. A detailed description of the MINOS Detectors can be found in [62].

3.4.1 Detector Design

Both detectors are steel scintillator tracking calorimeters with a magnetic field applied. The basic component of a detector is a plane of steel with scintillator mounted on the front followed by an air gap before the next scintillator/steel plane. The scintillator provides the detection medium for particles whilst the steel provides the necessary mass to induce neutrino interactions. The scintillator planes are composed of individual strips of scintillator with each alternating plane having its strips oriented orthogonally to its neighbours to allow 3-dimensional reconstruction of events.

The Far Detector needs to be as large as possible to maximise the number of observed events. The shape chosen for the planes was an 8 m diameter octagon. The entire detector is composed of 486 steel planes but is split into 2 super-modules of 249 and 237 steel planes each. The super-modules are separated by an air-gap of 1.15 m and have separately controlled magnetic coils that run through the centre of each super-module. Other than this they are identical. The front plane of each super module has no scintillator on it resulting in their being only 484 steel planes complete with scintillator. The total mass of the Far Detector is 5.4 kTonnes.

The Near Detector sees a much higher interaction rate by virtue of its proximity to the neutrino production point and therefore can be much smaller. The shape chosen for a plane was a squashed octagon with dimensions 4.8 m (horizontal) by 3.8 m (vertical).

The Near Detector is located in a cavern at the end of the NuMI beam line 100 m underground. It is composed of 282 steel planes. The magnetic coil runs through the right hand side of the detector as looked at from the beam direction. This leaves the left hand region of the detector free to detect neutrino interactions and consequently the beam is centred in this region 1.48 m to the left of the coil. Unlike the Far Detector not every steel plane has scintillator mounted on the front. Every 5th plane throughout the whole detector is fully covered in scintillator and hence these planes are referred to as fully instrumented. In the front 120 planes of the detector the 4 planes between the fully instrumented planes are covered only by a small region around the beam spot. These planes are referred to as partially instrumented. The remaining planes at the rear of the Near Detector have no instrumentation between the fully instrumented planes. This part of the detector is only for measuring muon tracks from neutrino interactions at the front of the detector. The front of the detector is used to measure hadronic shower

interactions. For this reason the front 120 planes are known as the Calorimeter Region and the back 162 planes as the Spectrometer Region. The total mass of the Near Detector is 980 tonnes.

3.4.2   Steel and Magnets

The steel that forms the bulk of the mass of the detectors is low-carbon hot rolled steel with an average density of 7.85 ± 0.3 g/cm^3. The average thickness of the planes in the 2 detectors is slightly different with the average thickness of a Near Detector steel plane being 2.563 ± 0.002 cm and a Far Detector plane being 2.558 ± 0.005 cm.

The detectors are magnetised to allow charge sign identification of particles. MINOS is one of the few neutrino experiments to have this capability. Both detectors make use of water cooled magnetic coils to provide the magnetic field. The Near Detector field is provided by a single 8 turn coil with cold conformed aluminium as the conducting material.

The Far Detector as described above is split into 2 super-modules each with its own separate magnetic coil. Each coil is composed of 190 turns of Teflon insulated copper wire. Both detector's magnets produce a similar strength field of ~ 1.3 T.

3.4.3   Scintillator

The scintillator planes in each detector are constructed in the same manner. A plane of scintillator is composed of strips of scintillating plastic with a wave length shifting (WLS) fibre embedded in it to transport the scintillator light to the read-out electronics at the edge of the detector by total internal reflection.

The strips that make a scintillator plane are 4.1 cm wide by 1 cm thick and made of scintillating plastic coated in a 0.25 mm thick layer of titanium oxide
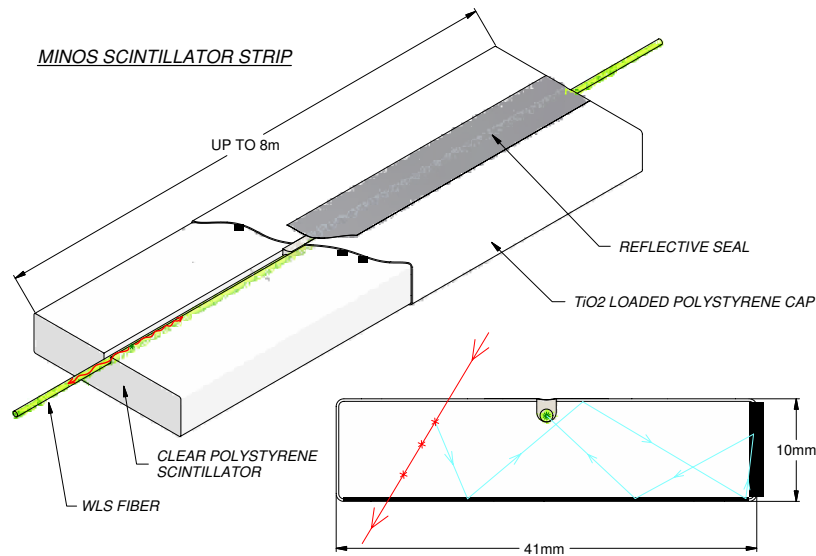
Figure 3.4: Schematic of a Scintillator strip used in the MINOS Detectors.

loaded polystyrene. The scintillating plastic is polystyrene loaded with the scintillating fluors PPO (2,5-diphenyloxazole) 1.0% by weight and POPOP (1,4-bis(5-phenyloxazol-2-yl)benzene) 0.03% by weight.

The WLS fibre is embedded in a 2.3 mm deep by 2.0 mm wide groove on the top face of a strip. To ensure efficient light collection the WLS fibre must be completely embedded in the groove. The WLS fibre itself is a 1.2 mm diameter double-clad polystyrene fibre with 175 ppm of Y11(K27) fluor. The WLS fibre shifts the scintillation light produced in the plastic from blue to green with an average wavelength of 530 nm. To prevent light leaking from the scintillator and improve the amount captured in the WLS fibre a specularly reflective strip of aluminised Mylar tape is placed over the groove after the WLS fibre has been glued in place.

The titanium oxide layer is to act as a diffuse reflector to prevent scintillation light escaping until it can be absorbed and transmitted by the embedded WLS fibre. A diagram of a complete scintillator strip can be seen in Figure 3.4.

When constructing a scintillator plane a sub set of between 13 and 28 strips are collected together into a module with a full plane being made of all the separate modules put together. Each module is encased in 0.5 mm thick aluminium and incorporates a manifold that gathers all the WLS fibres together into a single optical connector at the edge of the detector. This optical connector then links the WLS fibres to clear fibre bundles which are attached to the photo-multipliers which are in turn read out by the detector electronics.

Alternating planes have the strips aligned orthogonally to each other to allow 3-dimensional reconstruction. The strips are aligned diagonally on the faces of the detector in what are termed the u and v directions to avoid having the strips readouts at the top and bottom of the detector. The x and y directions that will normally be referred to are the horizontal and vertical directions when looking at the detector face. The longitudinal direction is always z. The size and arrangement of the Far Detector Modules is shown in Figure 3.5 and the Near Detector Modules in Figure 3.6.

3.4.4 Photo-Multipliers

The light transported by the WLS fibres is read out by multi anode Hamamatsu photomultiplier tubes (PMTs). The Near Detector uses a 64 anode PMT (Hamamatsu R5900-00-M64) and the Far Detector uses a 16 anode PMT (Hamamatsu R5900-00-M16). At both detectors a voltage of ~ 800 V is applied providing gains of 0.8×10^6 in the Near Detector and 1.0×10^6 in the Far Detector. The PMTs are mounted in light tight steel enclosures that not only provide light protection but also shielding from magnetic fields.

In the Far Detector each anode has 8 different fibres attached to it. The strips these fibres are coming from are separated by distance of $\sim$ 1m. In the
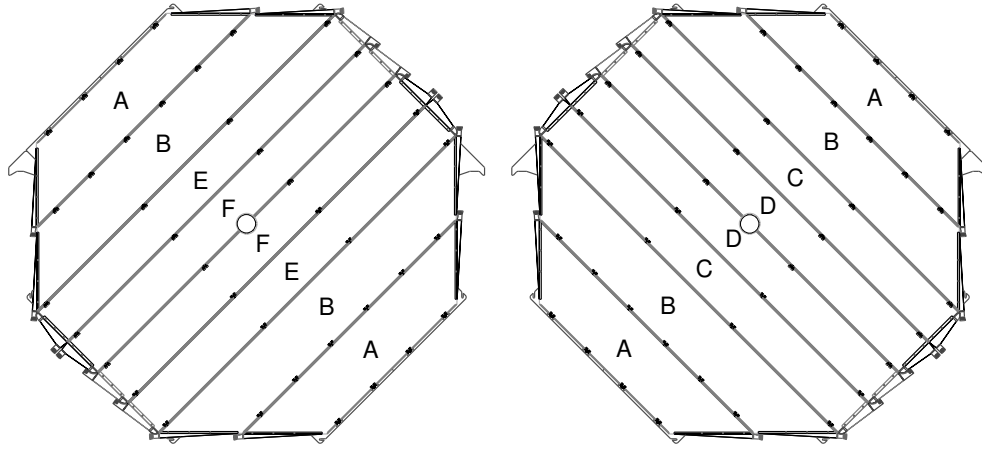
Figure 3.5: Scintillator Module pattern for the Far Detector. The u planes are on the left and the v planes on the right. The letters A-F denote the different module shapes. Modules A and B have 28 strips C-F have 20.
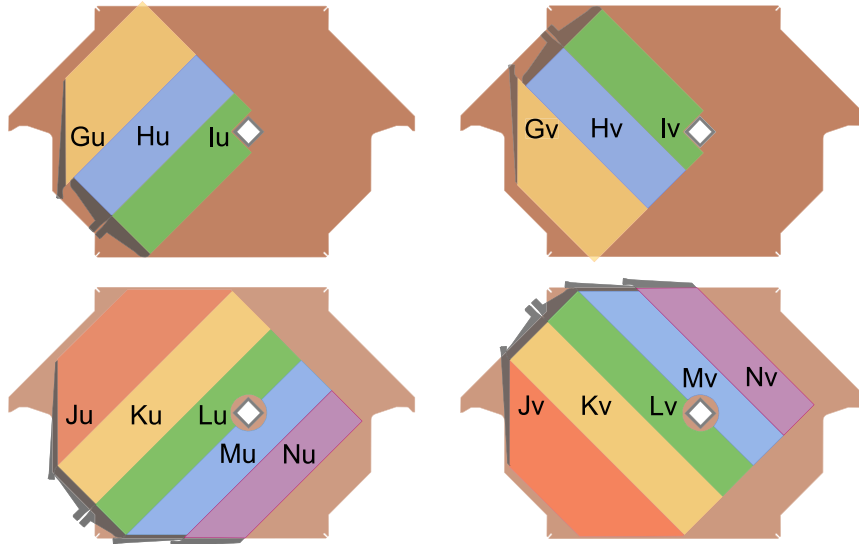
Figure 3.6: Scintillator Module pattern for the Near Detector. The Partially Instrumented planes are shown on top and the Fully Instrumented on the bottom. The u orientation planes are on the left and the v on the right. The letters G-N denote the different module shapes with 16 in total. The beam is centred midway between the coil hole and the left hand side of the Near Detector.

Far Detector strips are read out at both ends with a different combination of fibre connections at each end. Using this information and the hits detected in neighbouring planes the eightfold ambiguity as to which strip was really hit can be resolved.

In the Near Detector the strips are read out at only one end with the other end having a reflecting seal. In the calorimeter section of the Near Detector each fibre is read out by only 1 PMT anode. In the spectrometer region each 4 anodes are summed together and the result read out by a single electronics channel. The strips these fibres are attached to are also separated by distance of $\sim$ 1m.

There are advantages to using multi-anode PMTs including reduced cost and requiring less space and electronics but problems can occur. It is possible for charge to drift into neighbouring anodes causing a low pulse height hit to be detected on a strip that had no actual activity. This effect is known as cross-talk and is fairly well understood.

3.4.5   Electronics

As as has been previously stated the greatest difference between the Near and Far Detectors are the different interaction rates. This results in very different electronics requirements. This is therefore the major distinguishing feature between the detectors.

Far Detector

In the Far Detector each photo multiplier is connected to a VA32_HDR11 chip manufactured by IDE AS Corp. This chip provides a charge sensitive pre-amplifier, a shaper and sample/hold for each channel and is followed by an analogue output multiplexer.

The first stage of the VA readout is the VA Front End Boards (VFBs) located on the PMT housings. There are 3 VA chips on each VFB along with the associated support circuitry. These VFBs are connected to a VARC Mezzanine Module (VMM). These carry out all analogue portions of the final readout including signal receiving and digitisation. Each VMM can service 2 VFBs. The VMMs are serviced by the VA Readout Controllers (VARCs). These take care of trigger time stamping and control of the VA chips. A VARC can contain up to six VMMs and thus each VARC can control 36 PMTs and therefore 576 individual anodes. The VARCs are housed in VME crates with 3 to a crate. The signal is ultimately passed from the VME crates to the Data Acquisition System (DAQ)

The VFBs also house a discriminating chip called the ASDLite which takes the dynode signal from the PMTs and produces an output if the signal is greater than a tunable threshold. This threshold is set at $\sim 1/3$ of the mean amplitude of a single photoelectron. If this threshold is exceeded it begins the read out process by sending the signal from all 16 anodes to the VARC for digitisation. This dynode trigger is thus the lowest level trigger for VA chip readout.

Near Detector

The interaction rate at the Near Detector means that unlike the Far Detector the readout must be continuous without deadtime. To match the 53.1MHz frequency of the RF cavities in the Main Injector the readout is digitised with a timing resolution of 18.8 ns. The digitisation is achieved using a QIE (Charge to Current Encoder) chip utilising one per PMT anode.

The output signal of the QIE chip is split into 8 binary weighted ranges $(I/2, I/4, I/8...)$ by a current splitter with each part being integrated onto a different capacitor. The minimum unsaturated capacitor therefore corresponds to

the signal size and in this way increases the dynamic range of the output. During the next RF cycle the current splitter integrates the total charge of the previous cycle. In the cycle following that the signal is converted to a digital signal by an ADC and a fourth cycle is required to reset the capacitors. Thus to allow for continuous readout each QIE has 4 current splitters that integrate a cycle at a time.

The QIE, ADC and a FIFO (First In First Out) buffer to store the data from the cycle are all mounted together on a small circuit board called a MENU[2]. This allows the current splitters to share the same ADC.

MENUs are grouped together onto MINDERs[3] with 16 to a MINDER. The MINDER board is responsible for timestamping the signals and provides power and control for the MENUs for calibration purposes. The signal from the FIFO is passed to a MASTER[4] board which are housed in VME crates with up to 8 in a crate. These calibrate the MINDER signals by the use of look up tables and ultimately pass the signal to the DAQ.

3.5 Light Injection

As a way of monitoring the stability of the PMTs and electronics and to evaluate the single photo-electron gain the MINOS detectors incorporate a system of LEDs that can shine UV light of a known wavelength and chosen intensity onto the WLS fibres in the module manifold as the fibres exit the detector. This light therefore simulates scintillation light from the detector and is termed Light Injection (LI). The LI system operates in 2 modes. The first is an hourly check on the gains of the PMTs by flashing them with a known amount of light. The second is to

---

[2]MINOS Electronics for Neutrinos
[3]MInos Near DEtector Readout
[4]MINOS Acquisition, Sparsifier and Time-stamper for Event Records

calibrate for the non-linearity of the PMTs and electronics when exposed to high light levels ($>$ 100 photo electrons). The intensity of the LEDs is monitored by PIN photodiodes that are read out at the same time as the detector PMTs.

3.6 Triggering

All hits produced in the detectors that satisfy the requirements mentioned above are read out. It is up to the offline triggers to decide which are used for reconstructing events. There are many triggers to decide if data should be recorded in the Detectors and they fall into 3 categories: triggers based on coincident timing with beam spills, triggers based on clusters of activity in the detectors to record out of spill events and special triggers for debugging and calibration. In principle each spill can record multiple events and the record of a trigger is therefore termed a snarl.

Whenever a beam spill takes place a spill trigger is sent to the Near and Far Detectors. At the Near Detector the signal is sent from the Main Injector and all the data that takes place during the spill gate is recorded together as a single snarl.

At the Far Detector no such direct signal is available and so a remote spill trigger is sent. The Near Detector will already have been triggered by the spill trigger and the output data given a time stamp. This time stamp is then sent via the internet to the Far Detector which is synchronised to the Near detector by the use of GPS clocks. A 100μs window centered around this time stamp is then opened for the Far Detector to record data. Unfortunately the noise rate in the Far Detector from dark noise due to spontaneous emission in the WLS fibres and the PMTs is too great ($3 - 6$kHz) to allow this data to be recorded in an

untriggered way. To mitigate against this a VARC is required to receive at least 2 dynode triggers within 400ns of each other from the 36 PMTs it services before digitisation will take place, a process referred to as the 2/36 trigger. All data that passes the 2/36 trigger in the 100μs window is recorded.

In addition to these real spill triggers some fake spill times are randomly generated between real spills. These fake spill triggers are treated exactly as real spills and provide a random sample of detector activity for use in estimating detector backgrounds.

The out of spill time triggers rely on detector activity to initiate data recording. This allows events due to cosmic interactions to be stored as well as allowing data taking to take place should the link to the Near Detector be lost. There are 3 such triggers:

- The Plane Trigger requiring 4 out of 5 contiguous planes to be hit

- The Energy Trigger requiring 4 contiguous planes with a summed PH greater than 1500 ADC with at least 6 hits on those planes

- The Activity Trigger requiring activity on any 20 planes in the detector

3.7   MC Software

The MINOS experiment uses the data gathered at the Near Detector to make a prediction of the expected spectrum recorded at the Far Detector. However there is only so much that data alone can reveal. To examine systematic errors present and interpret the data according to theoretical models requires the use of simulated data. Like most particle physics experiments the data is simulated by the use of Monte Carlo (MC) techniques and is named such. Simulating data in MINOS is a complex task and requires simulation of every aspect of the experiment.

The first element to require simulation is the NuMI beam. For the MC considered in this thesis the production of hadrons from the target is simulated by the FLUKA package. The results of which are used as the input to the GEANT3 [63] based GNUMI framework. This simulates all the other components of the NuMI beam line. The ν_μ flux produced by the GNUMI simulation is used directly in the technique described in Chapter 5.

The simulation of the neutrino events in the detectors is performed in a package called GMINOS. In GMINOS the results of a neutrino-nucleus interaction in the detectors are simulated by a Fortran based package called NEUGEN [64] using the MODBYRS-4 cross-section model. Any long lived particles produced in an interaction are transported through the geometry of the detectors by a GEANT3 based model. The energy deposited by the physics processes that these particles undergo as they are transported through the detector is simulated by the GCALOR [65] package

The response of the detectors to the energy deposits is simulated by two C++ packages developed specifically for MINOS: PhotonTransport and DetSim. PhotonTransport simulates the generation of photons from the energy deposits in the scintillator provided by GMINOS. It also handles the transport of the photons to the PMTs by the reabsorption and reflection down the WLS fibres and provides details of the photo electrons produced at each PMT photocathode. DetSim simulates the amplification of the photo electrons in the PMTs and the subsequent response of the front end electronics and the data acquisition. The output from DetSim can be passed to the reconstruction and analysis code exactly like the data recorded from real spill events.

3.8   Reconstructing Events

The raw output that comes from either the real data or MC simulation has to be assembled into neutrino interaction events in a process called reconstruction. This aims to take the raw hits in the detector and determine whether they were part of a muon track or a hadronic shower and then combine tracks and showers together into whole events.

The simplest unit of data is termed a digit which is a record of the pulse height, time and location of a single detector digitisation.

These digits are then assembled into strips. A strip corresponds to digits that all happen in the same scintillator strip within a time window and are meant to correspond to a single energy deposition process. In the Far Detector there will be a separate digit from each end of the fibre which are combined into a strip. In the Near Detector successive digits in time are summed together into a single strip. Strips are the most basic unit of event reconstruction considered in this thesis.

Reconstructed strips that are close in space and time are grouped together into slices which are meant to represent the energy deposition from a single neutrino interaction. In the Near Detector due to the high event rate a single snarl will in general contain many slices. In the Far Detector with its lower event rate the chances of 2 neutrino interactions in the same snarl are essentially 0. It is therefore very unusual for there to be more than one slice per snarl and often indicates a reconstruction failure.

Strips within a slice are further reconstructed into the 2 components of an event: tracks and showers.

Track reconstruction takes place in 2 stages: track finding and track fitting. To find a track linear clusters of strips from each view that are near to each other are assembled together. The assembled track candidates from each view are then

combined to form a full track in 3 dimensions. The track fitter then runs over the complete assembled track using a Kalman fitter technique to determine the charge sign and curvature of the track in the magnetic field and the start (vertex) and end points of the track. This allows the momentum of the track to be calculated in 2 ways. For those tracks that stop in the detector the momentum can be determined by the range of penetration. For those tracks that exit the detector the momentum can be determined by the curvature in the magnetic field. The resolution of the energy calculated is 6% using range and 10% using curvature

Shower reconstruction looks for clusters of strips in a slice in the same area of the detector and combines them into a shower. A shower can be due to a number of sources such as electrons from ν_e CC interactions, delta rays from muon tracks and neutrino-nucleon interactions. The shower reconstruction estimates the energy of the shower and the vertex at which it was produced. The energy resolution of reconstructed showers is $55\%/\sqrt{E}$ for hadronic showers and $23\%/\sqrt{E}$ for electromagnetic showers.

The final step is the event reconstruction. This takes reconstructed tracks and showers close in time and space and associates them together as an event. An event represents the energy deposited in the detector due to a single neutrino interaction. An example would be a ν_μ CC interaction resulting in a track caused by the muon and a shower from the nucleon interaction being associated together at the neutrino interaction point. This event vertex is the best estimate based on the component track and shower vertices. Not all events have a track and a shower. NC events feature only a neutrino nucleus interaction and therefore often are only composed of a shower although they may have a track reconstructed erroneously. This is discussed further in Chapter 4.

3.9 Neutrino Flux Tuning

The agreement between the fully reconstructed MC spectrum provided by the simulation described above and the recorded data is not exact. Deviations of up to 30% are observed in the high energy tails of CC selected spectra. The simulation of the hadron production from the target is therefore tuned to improve the agreement between the data and MC [66]. The tuning takes place by adjusting a number of parameters used in the Near Detector MC simulation, in particular the longitudinal and transverse momentum of the original parent production in the NuMI target. An empirical parameterisation of the hadron production yield as a function of these momenta is used along with additional parameters related to the beam and detector modelling to reweight the events in the detector. A fit between the Near Detector CC selected data and MC spectra is then performed to determine the value of these parameters. The fit is performed on the spectra produced in 7 different beam configurations. These are the 4 beam configurations described in Section 3.2 and 3 further beam configurations. Two of these have the target in the same position as the LE and HO configuration but with horn currents of 170 and 200 kA. The other beam has a target position of 100 cm and a horn current of 200 kA. The result of the fit is used to provide a weight for each simulated event. With the result of the fit to the Near Detector data in place these weights can also be calculated and applied to the Far Detector simulation. Throughout this thesis whenever data and MC are compared the MC simulation is re-weighted by the results of this tuning.

3.10   MINOS Physics Goals and Achievements

The MINOS experiment was primarily designed to measure the atmospheric oscillation parameters Δm_{32}^2 and $\sin^2 2\theta_{23}$. Taking the ν_μ beam produced by the NuMI facility and measuring the spectrum at the Near Detector allows a prediction of the observed spectrum at the Far Detector. Any ν_μ disappearance seen can be fitted for oscillation parameters. The baseline and energy are such that the 2 flavour approximation described in section 2.3.2 is valid here. The result of the most recently published MINOS result [67] is shown as Figure 3.7.
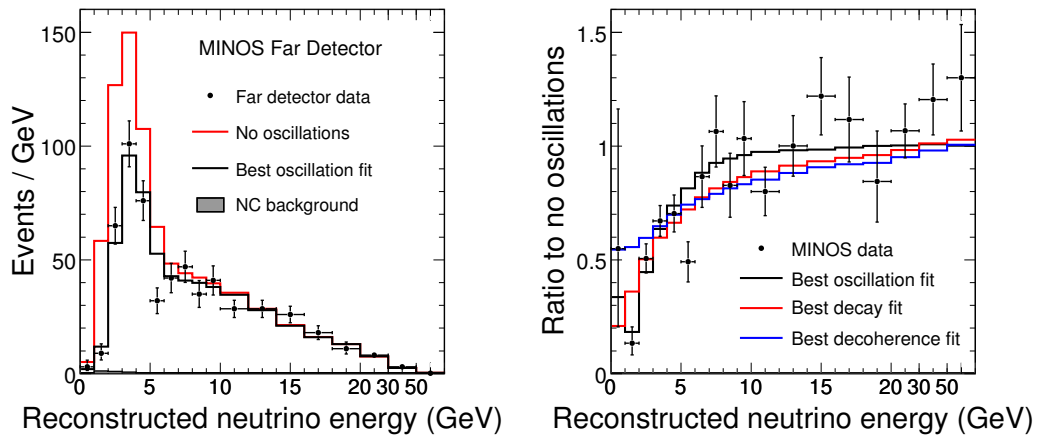
Figure 3.7: The latest MINOS result. The Left hand plot shows the data as points, the unoscillated prediction in red and the best fit to oscillations in black. The right hand plot shows the ratio of data to unoscillated prediction in black points and the ratio of the best fit to oscillations to the unoscillated spectrum in black line. Also included are the best fit to 2 other models of neutrino disappearance decay in red and decoherence in blue. Figure taken from [67].

The left hand plot shows the measured Far Detector spectrum compared to the unoscillated prediction for ν_μ CC events. As can be seen there is an energy dependent deficit in ν_μ CC events that can be explained by oscillations. This idea is shown more clearly in the right hand plot of Figure 3.7. This is the ratio of

the measured spectrum and best fit to the unoscillated spectrum. This ratio is equivalent to a measurement of the survival probability $P\left(\nu_\mu \to \nu_\mu\right)$. With the depth of the dip being governed by the size of the mixing angle $\sin^2 2\theta_{23}$ and the energy at the dip being related to the size of Δm_{32}^2. The best fit results are $\Delta m_{32}^2 = 2.43 \pm 0.13 \times 10^{-3}$ eV^2 at 68% C. L. and $\sin^2(2\theta_{23}) > 0.90$ at 90% C. L. Also shown are the fit to 2 other possible explanations of neutrino disappearance: decoherence and neutrino decay. The Figure shows that oscillations provide a better explanation than either of the other 2 models which are disfavoured at 3.7σ for neutrino decay and 5.7σ for neutrino decoherence.

Although MINOS was designed for this measurement it is capable of making other measurements. The high statistics Near Detector data set has been used to accurately measure neutrino cross sections [68]. The detectors are also capable of measuring cosmic neutrinos. Analysis of the oscillation parameters has been found to be consistent with oscillations and CPT conservation [69]. Further analyses on cosmic muons have been published showing the ratio of μ^+ to μ^- [70] and the seasonal variation in the rate of cosmic ray muons [71].

As mentioned in section 2.4.4 the value of the mixing angle θ_{13} is small but unknown with only a confidence limit being set. MINOS is capable of making a measurement of θ_{13} by searching for $\nu_\mu \to \nu_e$ oscillations which would manifest itself as ν_e appearance at the Far Detector. The result of the latest MINOS ν_e appearance analysis [72] is shown in Figure 3.8.

The MINOS detector is not optimised to search for ν_e events and they show up in the detectors only as electro-magnetic showers. With the resolution of the MINOS detectors it is difficult to differentiate between electromagnetic and hadronic showers. Consequently the background from Neutral Currents events is high. The Figure shows that there is a 1.5σ excess of ν_e events over the background
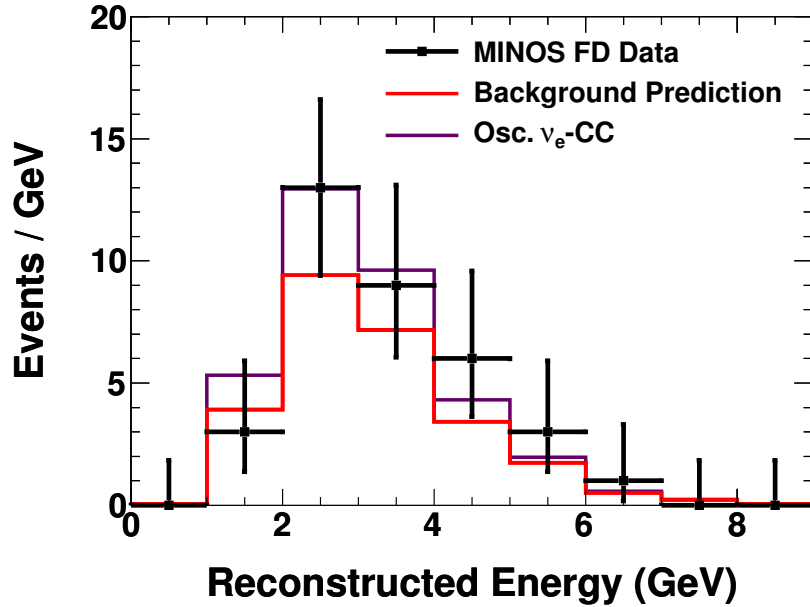
Figure 3.8: The Far Detector spectrum from the latest MINOS ν_e appearance result. The red line shows the expected number of background ν_e events. The black points show the data. The purple area shows the best fit to the data with ν_e appearance. Figure taken from [72].

with the best fit for oscillations to explain this excess shown. This allows a limit to be placed on the value of $\sin^2(2\theta_{13})$ comparable to the CHOOZ limit as can be seen in Figure 3.9.

Examination of Equation 2.15 shows that θ_{13} is always associated with the complex phase δ and as such is shown as a function of δ in the Figure. The limit on θ_{13} is dependent on the atmospheric mixing parameters. In the MINOS analysis these values were fixed to the MINOS best fit values from the analysis described above at $\Delta m^2_{32} = 2.43 \times 10^{-3}$ eV^2 and maximal mixing $\sin^2(2\theta_{23}) = 1.0$.

The Figure shows that in the Normal Hierarchy the MINOS best fit is comparable to the CHOOZ limit. An update of the MINOS ν_e appearance analysis using greater statistics will appear in the near future.
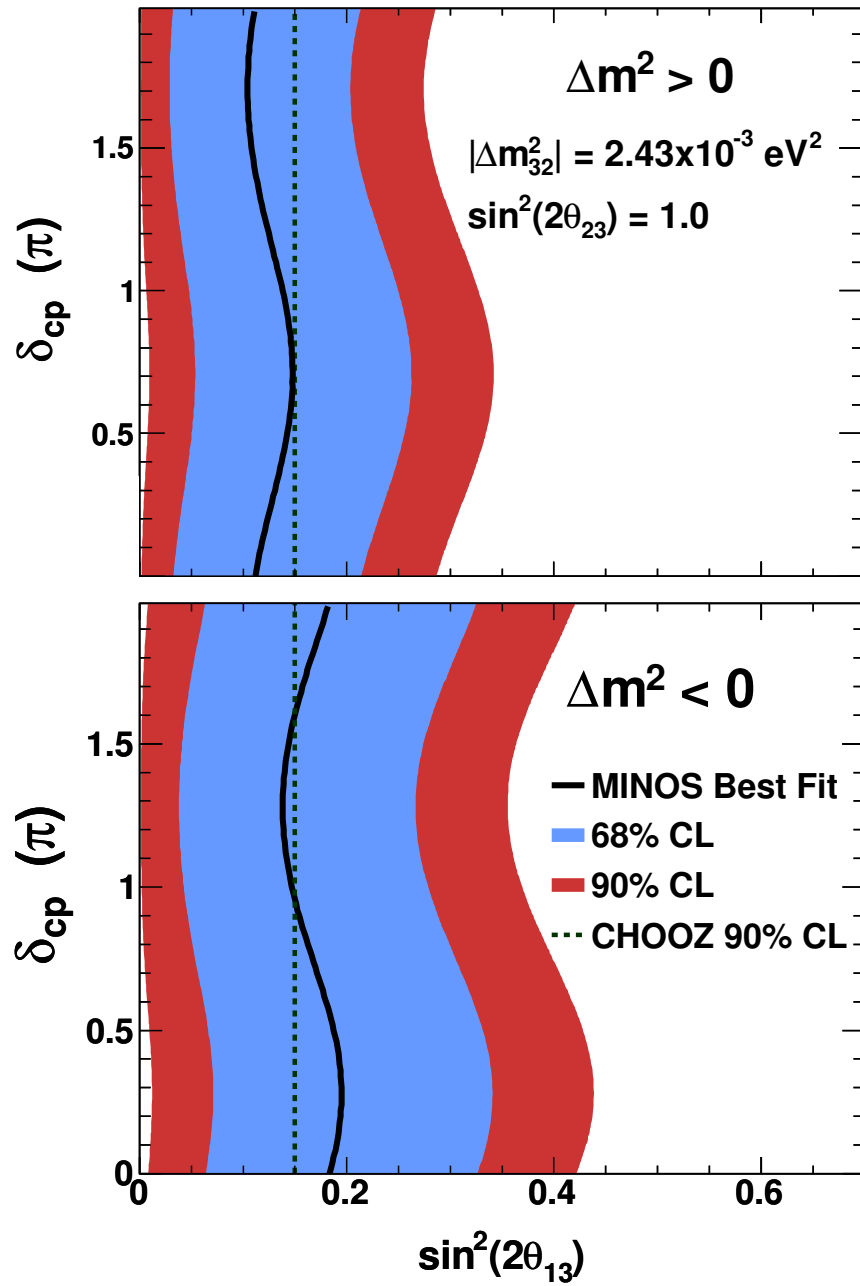
Figure 3.9: The limits set on θ_{13} by the MINOS and CHOOZ experiments. The CHOOZ upper limit is shown as the dotted line. The MINOS best fit is shown as the solid line. The blue area is the MINOS 68% C.L. and the red area the 90% C.L. The top plot shows the limits for the Normal Hierarchy and the bottom plot for Inverted Hierarchy.

In MINOS, because the detectors are magnetised, the sign of any muons produced can be determined by the curvature in the magnetic field. In this way a disappearance analysis can be performed on the 7% $\overline{\nu}_\mu$ background in the beam. Any difference in oscillations between ν_μ and $\overline{\nu}_\mu$ is an indication of CPT violation. The MINOS experiment has performed such an analysis [73] with the result shown in Figure 3.10.

The figure shows that the result is not a strong one with only a small area of parameter space being excluded at 3σ. It is however in agreement with the MINOS ν_μ oscillation result. As has been discussed above a beam of $\overline{\nu}_\mu$ can be produced by changing the magnetic field in the focusing horns. MINOS is currently taking data with a $\overline{\nu}_\mu$ beam and an analysis based on this data will provide a more accurate test of CPT conservation.

A further analysis that can be performed in the MINOS experiment is a search for sterile neutrinos. As described in section 2.4.5 the LSND anomaly can be explained by the existence of a sterile neutrino. MINOS can search for oscillations to steriles by the measurement of Neutral Current interactions. As has been shown the spectrum of ν_μ CC interactions in the Far Detector is depleted by $\nu_\mu \rightarrow \nu_\tau$ oscillations. However it is expected all flavours of active neutrino will still interact via the NC interaction. Therefore the Neutral Current spectrum should agree with the prediction. Any deficit in the predicted Neutral Current spectrum could be as a result of oscillations to a sterile neutrino. The subject of this thesis is a search for sterile neutrinos. The next Chapter will outline the way NC events are identified in the detectors with subsequent Chapters explaining how the Far Detector prediction is made, the specific models being used to search for sterile neutrinos and the results of the analysis.
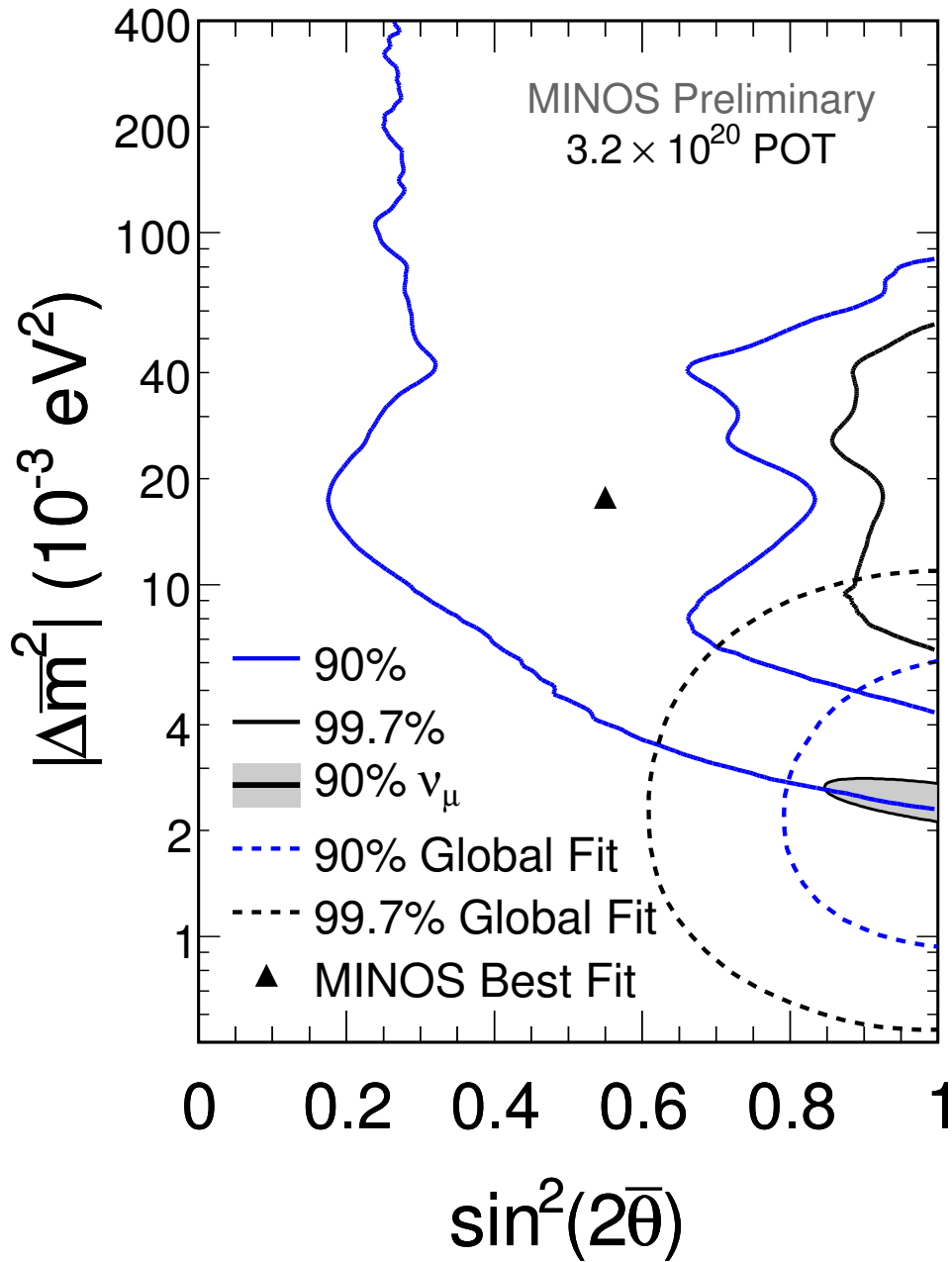
Figure 3.10: The result of the $\overline{\nu}_\mu$ disappearance analysis in MINOS. The Black line shows the 99.7% allowed region. The Blue Lines show the 90% allowed region. The black triangle is the best fit point. The result of global fits to other data are shown as dashed lines. The MINOS ν_μ oscillation allowed region is shown in grey.

Chapter 4

Selecting NC Events in the MINOS Detectors

4.1 Introduction

The subject of this thesis is the search for sterile neutrinos in the MINOS data set. This obviously requires the distinction of Neutral Current (NC) and Charged Current (CC) events in the detectors.

The characteristic difference between NC and CC events is the lack of a muon in the final state. NC events show up as hadronic shower activity whereas CC events will show a muon track. However it is not as simple as saying all events with a track are CC events and all events without are NC events. Other particles such as pions and protons can create tracks that can be confused with muon tracks. In the distribution of strips seen in an event it is possible for the reconstruction code to produce tracks where none really existed. For this reason NC/CC discriminating methods focus on examining reconstructed tracks.

In this chapter such a technique is demonstrated. Firstly the data quality

requirements for the Near and Far Detectors are discussed. Next the classification of events that are easily classified is shown. The classification of the remaining events as NC or CC by a purpose built Artificial Neural Network (ANN) based on event shape and track quality variables is then presented.

4.2 Pre-selection

Not all events reconstructed in the detectors are suitable for use in physics analysis. Events are required to be in the body of the detector and satisfy various cleaning requirements. These are described below.

4.2.1 Fiducial Volume

Neutrinos interacting near the edges of the fully instrumented regions of the detectors will lose some of their energy into uninstrumented regions and lower the energy resolution of events. These events will also suffer from reconstruction problems; if a track leaves the detector soon after being created for example there may not be enough of it in the detector to recognise it as a track. For this reason a fiducial volume is defined in both detectors to ensure good energy resolution and precise event reconstruction.

Near Detector

To qualify as being in the fiducial volume in the Near Detector an event must have a vertex further than 50 cm from the edges of the partially instrumented planes. This value was optimised to ensure good shower containment. Additionally in the Near Detector, ideally only muons should penetrate into the spectrometer region as there is not enough instrumentation to allow proper shower reconstruction. The
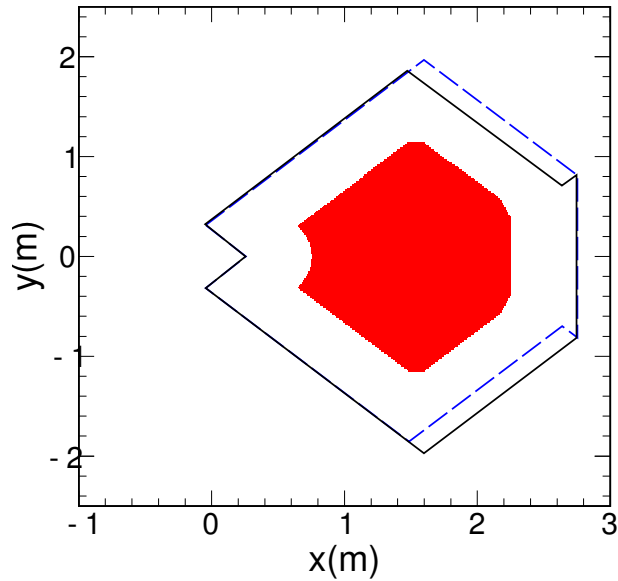
Figure 4.1: The x-y cross section of the Near Detector Fiducial Volume shown in red. The lines show the outline of the partially instrumented planes. The U-view is in dashed blue and the V-view in black.

longitudinal cuts have therefore been optimised to contain shower energy in the calorimeter. A cut of 1.7 m $< z <$ 4.7 m is required. During the reconstruction showers and tracks in an event are assigned their own vertex in the detector. If the event builder puts a track and shower together to form an event an event vertex is produced from the shower and track vertices. For events with a well defined track (meaning where the track in the event crosses more planes than the shower in the event) the track vertex is the best estimate of the true interaction vertex and is therefore used. Otherwise the event vertex is used. The x-y cross section of the Near Detector fiducial volume is shown as Figure 4.1.

Far Detector

As all the Far Detector planes are fully instrumented, to qualify as being in the Fiducial Volume in the Far Detector an event must have a vertex > 50 cm from
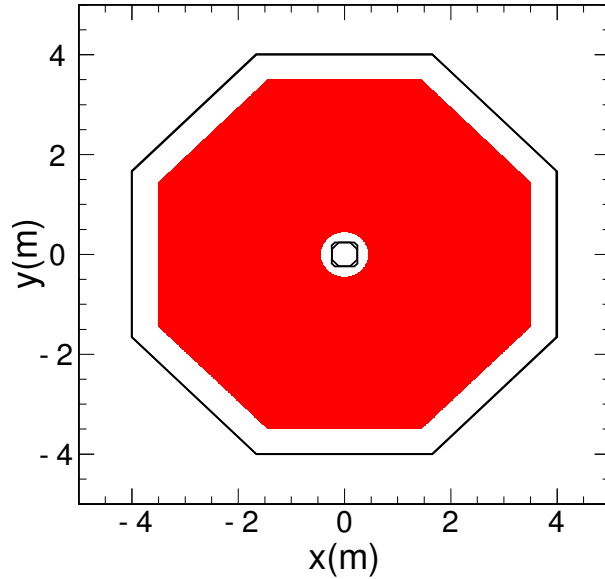
Figure 4.2: The x-y cross section of the Far Detector Fiducial Volume shown in red. The lines show the outline of the planes and the coil hole.

the edges of the planes. In addition as the coil runs through the middle of the Far Detector planes it is also required that the vertex be > 45 cm from the centre of the coil hole. The Far Detector is split into 2 super-modules and therefore there are 2 sets of longitudinal cuts, one for each super-module. In super-module 1 a cut of 0.23 m $< z <$ 13.6 m is required and in super-module 2 a cut of 16.1 m $< z <$ 28.8 m. This leaves $\sim$ 1.2 m at the back of a super module for good shower containment. Similarly to the Near Detector events with a well defined track use the track vertex, otherwise the event vertex. The x-y projection of the Far Detector Fiducial Volume is shown as Figure 4.2.

4.2.2   Near Detector Cleaning

Due to the high event rate in the Near Detector reconstruction pathologies can result in a background that are mis-identified as NC events. As the Far Detec-
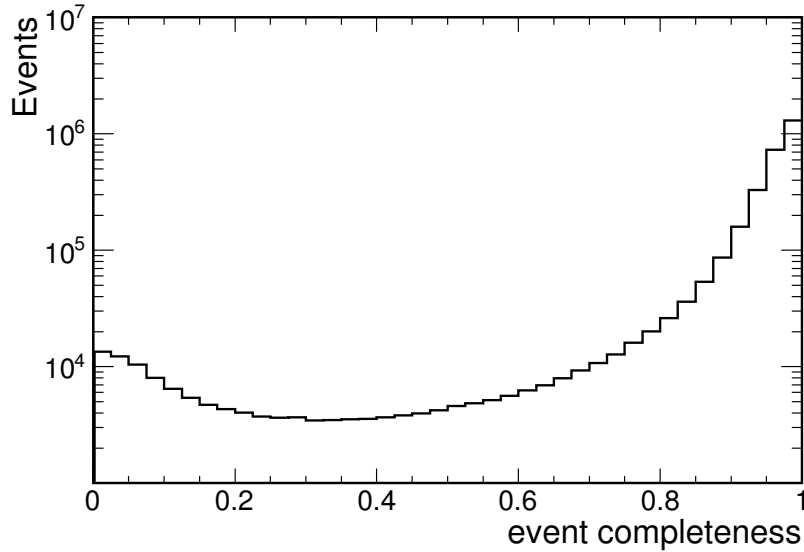
Figure 4.3: The event completeness for the Monte Carlo.

tor has no such high event rate this will lead to inter detector differences unless mitigated against. These reconstruction pathologies are seen in both data and MC. These reconstruction failures are studied using the MC simulation where the truth information of the interaction being simulated in the Near Detector is available. The measure used to determine the quality of reconstruction of an event is called completeness, which is defined as the summed reconstructed pulse height in the event attributed to the neutrino interaction using the Monte Carlo truth information divided by the total reconstructed pulse height due to this neutrino interaction.

As shown in Figure 4.3 there are a sizable number of events with completeness less than 50%. A method for removing these low completeness events is shown in [74, 75]. A brief summary is presented here. The reconstruction failures can be classified into 3 categories described below and each has its own specific set of cuts to remove them.

Split Events

These are events in which a single neutrino causes more than one event to be reconstructed. This can be due to a number of causes such as late activity neutrons or gaps in the hit strip pattern. Typically what happens is that a smaller piece of a large event is split away from the main event and two events are formed. The smaller of these will often look like a low energy NC event. These events can be mitigated against by the use of temporal and spatial cuts. If two reconstructed events are due to the same neutrino interaction it is expected that they will be close in time and/or space. Split events will be expected to be close in time. This class of events is removed by requiring that no event is closer than 40 ns in time to any other. Events due to late activity will be expected to be close in space and some time close to previous events but not as prompt as for split events. To remove this class of events if an event is closer in time to any other event than 120 ns and closer than 1 m in the z direction to the same event it is removed.

Event Migration

An event that interacts at the edges of or in the rock outside of the detector and is sufficiently large that part of its energy leaks into the detector and is reconstructed within the body of the detector is said to have migrated. This pathology often results in small events that look like NC events. There are two classes of event that can be considered leakage and are dealt with by two different sets of cuts. Events entering sideways into the detectors can cause problems for the vertex finding and reconstruction algorithms resulting in steep showers that have many strips hit but cross very few planes. A steepness measure based on the the number of strips and the number of planes in the event is evaluated and very steep events removed.

The second class of events are due to similar causes but are not as steep. To

mitigate against these events veto regions are defined at the edges of the detector. Only the calorimeter region is considered and both sides are considered separately. If there is an excessive number of strips and pulse height in these veto regions close in time to a reconstructed event then it is a good indicator that the event may have migrated. For this class of cuts the strips do not have to be reconstructed as part of the event just closer than 40 ns in time. In addition for this class of events only those without a well defined track and with reconstructed energy < 5GeV are considered. This makes the cut more specific to migrating events. If there are > 4 strips and more than 1000 ADC of pulse height in either veto region the event is removed.

Remaining Failures

The final category are for those events with low completeness that are not due to either of the above causes. If showers are diffuse then the reconstruction may fail to reconstruct it properly. The majority of such low completeness events have low numbers of strips in them. If an event has less than 5 strips then it is removed.

The effect the Near Detector cleaning has on the energy spectrum of selected NC events is shown in Figure 4.4. The plot shows that the cuts remove events of all energies but also clearly demonstrates how effective the cleaning is at removing poorly reconstructed events. As can be seen from the lowest 0.5 GeV energy bin which has been reduced from a 50% contamination to only a 7% contamination when ND cleaning is applied. The figure also demonstrates that despite being tuned on the MC the cleaning effects the data and MC in the same way.
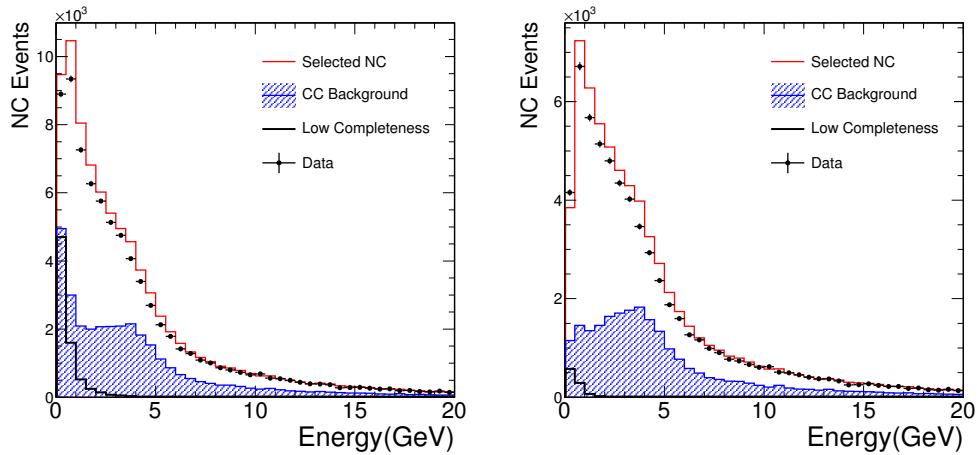
Figure 4.4: The effect of the ND cleaning on the NC selected spectrum. The left plot shows the spectrum before ND cleaning is applied. The right plot shows the spectrum after ND cleaning is applied. The red line is the NC selected MC, the blue hatched area is the CC background, the black line is the low completeness events and the black points are Data.

4.2.3   Far Detector Cleaning

The Far Detector does not suffer from the same high event rate as the Near Detector and therefore has different requirements for pre-selection. The details of the Far Detector event cleaning can be found in [76] and are summarised below for completeness.

The main backgrounds in the Far Detector are:

- Data recorded whilst the Light Injection Calibration system is flashing.

- Noise in the detector from a number of causes including noise in the electronics, the PMTs or spontaneous emission from the scintillator or WLS fibres.

- Muons from cosmic rays.

The light injection is removed by use of a specific PMT that is directly connected to the light injection system. This removes 99.99% of data recorded whilst

LI is flashing with a further series of cuts removing the remainder. As LI causes a greater amount of activity in the detector than a neutrino event, events with a large number of hits on a single plane may be due to LI. As the LI is injected from only one side of the detector, attenuation in the WLS fibres leads to an asymmetry in the recorded light output. Neutrino events tend to be more centrally located in the detector and hence have a smaller asymmetry. As only known parts of the detector are flashed at any given time examining the detector for large amounts of activity in these regions compared to other parts of the detector can indicate LI. All of the above cuts must fail for data to be classified as due to the Light injection system

As was discussed in Section 3.6 various trigger thresholds are set to remove the low intensity noise from the electronics, PMTs and the spontaneous emission noise. Any remaining noise is removed by cuts on the minimum number of strips and the ADC pulse height of an event.

The cosmic muons are expected to occur at approximately the same rate within spills as beam induced neutrinos. Most cosmic ray induced muons are well reconstructed and removed by the fiducial requirement. However as the reconstruction is designed to reconstruct beam muons coming into the front face of the detector certain cosmic pathologies can be seen. These usually manifest themselves as very steep cosmic muons and can be removed by a combination of cuts on track angles and, for events so steep they are reconstructed only as showers, by using cuts on transverse and longitudinal shower profiles. Cosmics that stop in the detector can look like beam events. To remove these the track is examined to determine whether it exits the sides of the detector and if so cuts on track directions are made to check if it is upward going.

The event rate in the Far Detector is so low that the probability of 2 beam

induced events occurring simultaneously is essentially zero. Therefore if 2 events are reconstructed together it is due to either a reconstruction failure or due to a non-beam source. To mitigate against this an event is required to contain 75% of the total deposited energy if it is to be used.

4.3   NC and CC Discrimination Method

The basis of the method is a cut based pre-classification followed by an Artificial Neural Network (ANN). The cut based part classifies easily identifiable events, with the remaining events classified by an ANN into either CC or NC events. The ANN output is such that events that are determined to be NC-like are assigned an output value of close to 0 and events that are CC-like assigned values approaching 1. The two parts of the method are combined to give an overall particle identification (PID) selection by assigning a PID value of 0 to events pre-selected as NC and 1.5 to those selected as CC.

4.3.1   ANN Pre-classification

It is good practice when designing an ANN to only train on those events in which differences are expected. There is no point in using events that can be unambiguously classified by some other means. For this reason a series of pre-classification cuts are used to remove events that are easily classified. As described above the main distinguishing feature between NC and CC events are the presence of a muon track. This results in CC events, in general, being substantially longer and having a track reconstructed more often than NC events. The pre-classification therefore focuses on the length and the number of tracks in an event.
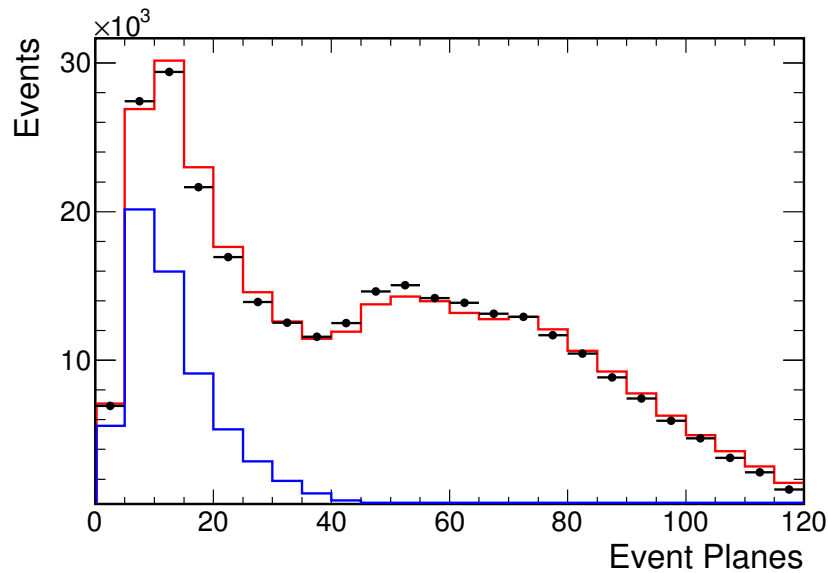
Figure 4.5: The number of planes in the event for the Near Detector. The black markers show the data. The red line shows the Monte Carlo. The hatched blue area shows the True Neutral Current events.

Event Planes Cut

An initial cut based classification of events is performed. The distribution of the planes in an event in the Near Detector is shown as Figure 4.5. As can be seen there are very few NC events with more than 40 planes and at this point the number of CC events begins to increase relative to the number of NC events. Therefore any event with greater than 40 planes is classified as a charged current event and assigned a PID selection output of 1.5.

Number of Tracks

The distribution of the number of tracks reconstructed in an event is shown in Figure 4.6. It can be seen that 72% of events without a track are NC events and only 15% of those with 1 track. However the events reconstructed with tracks cannot simply be ignored as 60.7% of all NC events are reconstructed with a
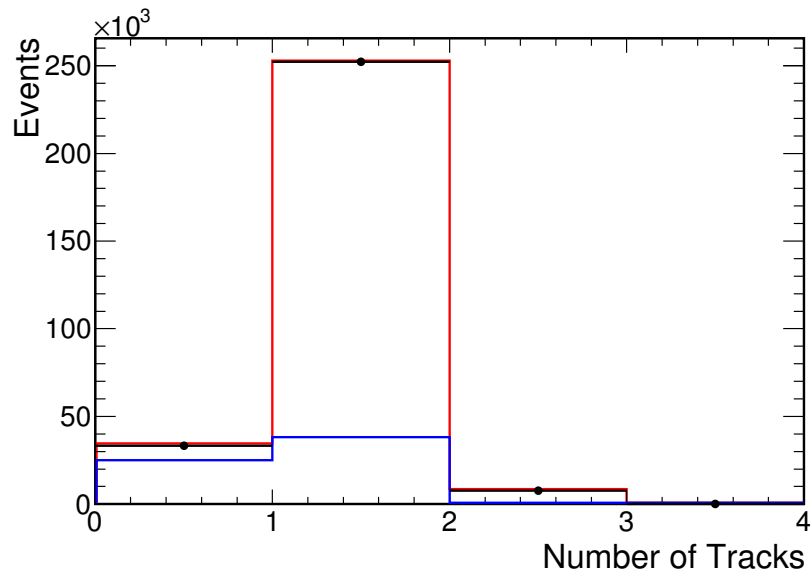
Figure 4.6: The number of tracks reconstructed in the event for the Near Detector. The black markers show the data. The red line shows the Monte Carlo. The hatched blue area shows the True Neutral current events.

track. As the topology of events with and without a track are very different the events are divided into 2 categories: events with tracks and events without. This allowed separate ANNs to be developed to take advantage of the different event shapes and to take advantage of the many more variables available relating only to the track. As will be described in Section 4.6.2 it was not possible to design an ANN for events without a track that showed any discrimination power better than simply selecting all no track events as NC. Therefore all events with no track are assigned a selection output of 0 and thus automatically classified as NC.

4.4 Artificial Neural Networks

Artificial Neural Networks are a general method for learning real valued functions based on examples. Fundamentally an ANN is a number of input nodes connected to 1 or more layers of hidden nodes connected to a layer of output nodes. Every

input node is connected to every hidden node and every hidden node is connected to every output node. All connections have a weight and each node produces an output based on the sum of its weighted inputs. These weights are determined by training on example sets of input and output parameters. Ideally the weights are calculated such that for any given set of inputs the correct value of the output nodes is produced.

A network is trained by first initialising all weights to small random values. The input nodes are then given the input values of the first training example and these are propagated through the network. The value of the output nodes determined is then compared to the values of the training example output nodes and an "error" on the outputs calculated. Usually a process called backpropagation is then applied to the error of the output nodes to calculate the error of the hidden nodes.

The weights between nodes are then updated using some chosen algorithm so that the error is reduced. The inputs for the next training example are then used and the process repeated. A full training cycle uses all the training examples and is called an epoch. The network as it is being trained should be applied to 2 separate data sets simultaneously, commonly termed the training and test data sets. The training data set is used to update the weights and the test set merely has its error calculated based on these weights. The network is considered fully trained when the test dataset error is at the absolute minimum. This avoids the risk of over-training the network whereby idiosyncratic features particular to the training sample are modelled which are not generally present.

There exist many choices for the type of node, error estimator and learning algorithm. For further details of ANNs see for example [77].

4.5 ANN Development

The network presented here is of the simple feed forward type. The defining characteristic of which is that the output of each layer goes directly to the next layer without any feedbacks or loops.

The node used in the input and hidden layers of the network presented here is of the sigmoid type. The sigmoid function takes the form:

$$\sigma(y) = \frac{1}{1 + e^{-y}}$$

Hence for a given node j with n input values x_i and corresponding weights w_i its output will be given by:

$$o_j = \frac{1}{1 + e^{-(\sum_{i=0}^{n} w_i x_i)}} \tag{4.1}$$

It has the useful properties that its output is a non linear function of its inputs. This means that any continuous function can be approximated by a linear combination of sigmoid nodes allowing it to model non linear functions [78].

In addition its output is a differentiable function of its inputs. In particular:

$$\frac{d\sigma(y)}{dy} = \sigma(y)(1 - \sigma(y)) \tag{4.2}$$

This allows it to be used in back propagation. Backpropagation involves adjusting the weights of the previous layer by the derivative of the error with respect to the weights in that layer. This is done sequentially to every layer starting from the output hence the term backpropagation.

The Network uses a cross entropy error estimator. Using this estimator for a particular training example d the cross entropy error E_d is given by:

$$E_d = - \{t_d \log(o_d) + (1 - t_d) \log(1 - o_d)\} \qquad (4.3)$$

Where t_d is the target value (1 or 0) for training example d and o_d is the probability estimate output by the network for training example d. The full error for an entire training sample is the sum of the contributions from each training example.

The use of a cross entropy error estimator is appropriate in cases such as that presented here where the training examples exhibit only boolean target values but are to be represented by a probability based on the input values.

In this case an event is either CC (1) or NC (0). The output of the ANN however will be a probability that the event is CC or NC with a value in the range 0-1 with values closer to 1 being more CC like and values closer to 0 being more NC like. For details see for example [77].

The back propagation method used was the Broyden, Fletcher, Goldfarb, Shanno (BFGS) method [79].

4.5.1 Training a Network

The training of a network proceeds as follows. Networks were trained on the full MC sample which in the Near Detector is equivalent to 2.38×10^{20} Protons on Target (POT). The events are split into 2 samples; a training and a test sample.

Of these events only some are selected for use in the training or testing samples put into the network. All events are required to be clean and within the Fiducial Volume as described above. Preliminary studies showed that networks trained on clean events that also require the completeness > 0.5 performed better than those only requiring events to be clean. Thus only events with completeness > 0.5 are
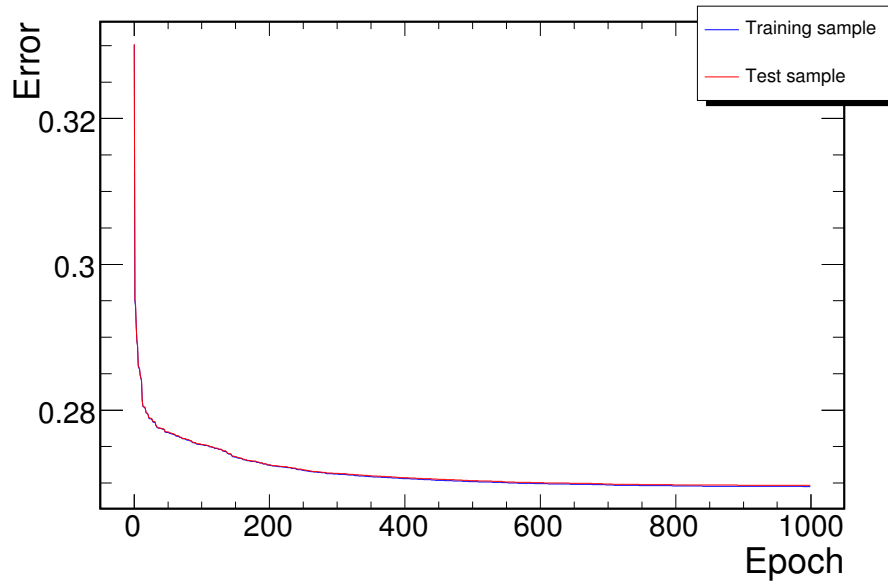
Figure 4.7: The error returned during ANN training. The error on the training sample is shown in blue, the error of the test sample is shown in red.

included in the samples.

As explained above events with no track and events with greater than 40 planes are pre-classified as neutral current and charged current respectively and are therefore not included in the training sample.

Each network was trained for 1000 epochs and the resulting error curves examined to determine if the minimum had been reached and to guard against over-training. A typical example is shown as Figure 4.7. It can be seen that the error for both training and test samples decreases as training continues. Both flatten out at 500 epochs and therefore 1000 epochs is adequate to consider the ANN fully trained.

4.5.2   Input Variables

The ANN presented here was based on existing work in [74]. Using this as the starting point further variables expected to have discriminating power were added. This was determined either by inspection or by making use of the Multivariate

Discriminate Analysis presented in [80]. This was initially developed for electron neutrino induced event discrimination but adapted for NC and CC selection. One of the outcomes of the method was to rank variables according to discrimination power.

A network would be trained as outlined above and its performance in separating NC from CC events was determined in terms of 2 figures of merit:

- $\epsilon \times \mathbf{P}$

- $\epsilon \times \mathbf{P}/(2 - \mathbf{P})$

Where ϵ is efficiency and $\mathbf{P}$ is purity.

If only the events that pass the Fiducial Volume and cleaning cuts described above are considered, the efficiency (ϵ) is defined as the number of true NC events selected divided by the total number of true NC events. The purity ($\mathbf{P}$) is calculated as the number of true NC events selected divided by the total number of selected events. Thus the efficiency is the percentage of the total number of signal events that are selected. Purity is the percentage of selected events that are signal events.

When determining a selection there is a balance to be made between ensuring good sensitivity by including as many signal events as possible whilst rejecting background events. The efficiency defined above gives a measure of how many total signal events are selected whilst the purity gives a measure of how much of the selected sample is background.

The contribution of the input variables in the network was then determined and input variables found not to be useful were removed and a new network trained. The ANN presented here is the final result of this iterative process. It takes 7 inputs with 10 hidden nodes to give a single output to classify events as either NC
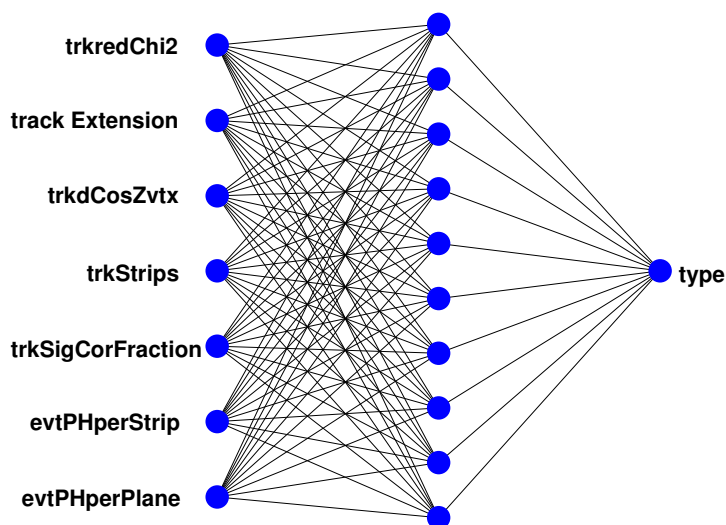
Figure 4.8: Layout of the ANN showing the 7 input variables the 10 nodes in the hidden layer and the output.

or CC. A graphic representation of the network is shown as Figure 4.8.

The 7 variables used are:

- evtPHperPlane - event pulse height per plane

- evtPHperStrip - event pulse height per strip

- trkSigCorFraction - see below

- trkStrips - total number of strips in the track

- trkdCosZvtx - the z direction cosine of the vertex

- trackExtension - trackPlanes - showerPlanes

- trkredChi2 - reduced χ^2 of the track fit

The first 2 variables are general to the whole event and are related to how the energy is distributed in the event.

The remaining 5 variables relate to the track only. Most of the definitions are trivial. The trackExtension is defined as the number of planes the shower has hit strips in subtracted from the number of planes the track has hit strips in. As NC events have short tracks compared to CC events then this has lower values for NC events. The trkredChi2 is a measure of the quality of the fit of the track returned by the track fitting algorithm. Tracks in NC events are not real muon tracks and therefore tend to have worse fits.

The trkSigCorFraction variable was originally developed for use in a k Nearest Neighbour NC/CC classification algorithm described in [81]. It is formed by taking the ratio of the pulse height of the strips in and near the track to the strips that are in the track only. As muon tracks are clean and well defined they tend to have little surrounding pulse height and therefore tend to have values of trkSigcorFraction of near 1. False muon tracks found in NC events tend to be messier and have more strips in the detector surrounding it and therefore have values less than 1.

Figure 4.9 shows the distribution of data and Monte Carlo for the input variables at the Near Detector. The agreement between data and MC is in general good.

4.6 ANN Performance

4.6.1 Events With a Track ANN

The output of the ANN is shown in the left plot of Figure 4.10. It shows the separation of NC and CC events achieved by the ANN. As expected the CC events mainly appear in the peak at PID values ~ 1 and the NC events are mainly at lower values peaking at PID values ~ 0.45. The separation is not complete as there are certain events that are indistinguishable using the ANN. The agreement between
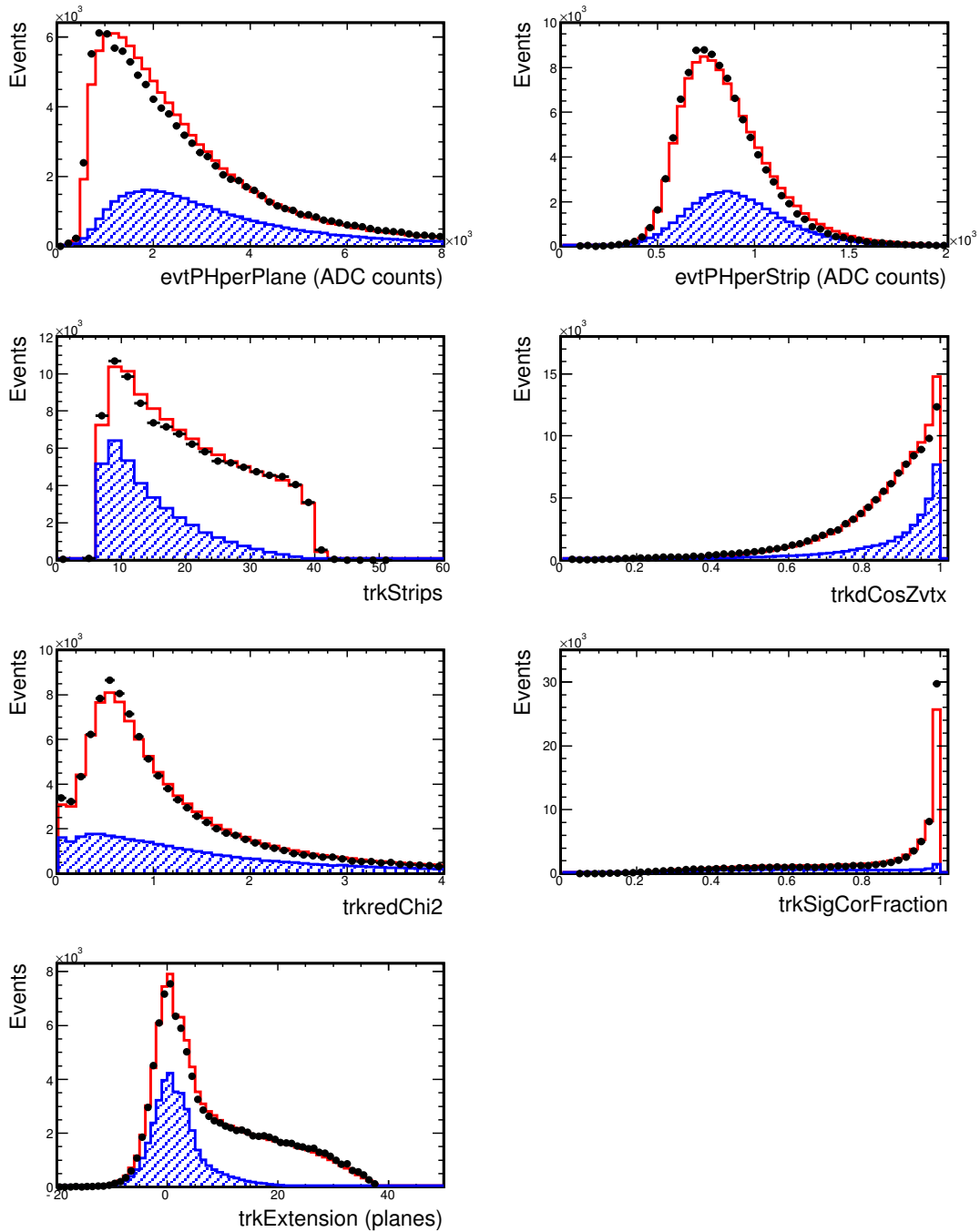
Figure 4.9: The ANN input variables in the Near Detector. The red line shows the Monte Carlo, the black points are the data and the blue hatched area is the true Neutral Current events

the MC simulation and the data seen in the left plot of Figure 4.10 is good in the overall trend but it does show an excess of MC over data of NC-like events and a deficit of selected CC events. To investigate whether this difference is due to the selection method presented or an intrinsic problem with the MC simulation a new network was trained with the evtPHperPlane variable removed. This variable was chosen as it has the worst data/MC agreement as can be seen from Figure 4.9. The new network with only 6 variables showed the same shape as the original network but with a slightly narrower NC peak and a reduced CC peak due to CC events being moved to lower values. This behaviour is expected as information has been removed from the network by the removal of the variable. Despite these changes the original and 6 variable network display a very similar overall performance in terms of efficiency and purity. Most importantly, in addition to these differences the same discrepancies between the data and MC are observed with an excess in the NC peak and a deficit in the CC peak of MC over data. This finding indicates that the cause of the discrepancy is an intrinsic problem with the MC rather than a problem with the selection method itself. This discrepancy is compensated for in the extrapolation technique described in Chapter 5.

Adding in the events classified by the pre-classification criteria gives the overall PID output shown on the right in Figure 4.10. Events are classified as either NC or CC by defining a PID cut position and classifying everything with a PID value larger than the cut position as CC and everything with a PID value less than the cut position as NC.

The optimisation of the cut position is determined by scanning the full PID range and calculating the efficiency and purity at each cut value and then calculating the figures of merit. The efficiency and purity as a function of PID separation value is shown as Figure 4.11. The cut value was chosen to optimise the value of

Figure 4.10: The output of the ANN and the PID. The red line shows the ANN or PID output value for MC events. The black dots show the Near Detector data. The hatched blue areas are the true NC events from the MC. The plots are normalised by POT. The vertical line marks the position of the cut.

$\epsilon \times \mathbf{P}/(2 - \mathbf{P})$ and is found to be at a maximum value of 0.437 at PID parameter value of 0.643 and is shown in the plots. This figure of merit is chosen as it minimises the fractional error on the number of signal events seen [76]. This is demonstrated in Appendix A.

Selected Spectra

The selected NC and CC spectra are shown in Figure 4.12. The overall selection efficiency for the method is 92.2% and the purity is 64.3%. The energy of a CC selected event is given by summing the energy of the track and shower in that event. For NC selected events without a track the event energy is the same as the shower energy. For NC selected events with a track any strips that are shared between the track and the shower are used in energy estimation. Those in the track only are ignored.

The efficiency and purity of the NC selection as a function of energy is shown
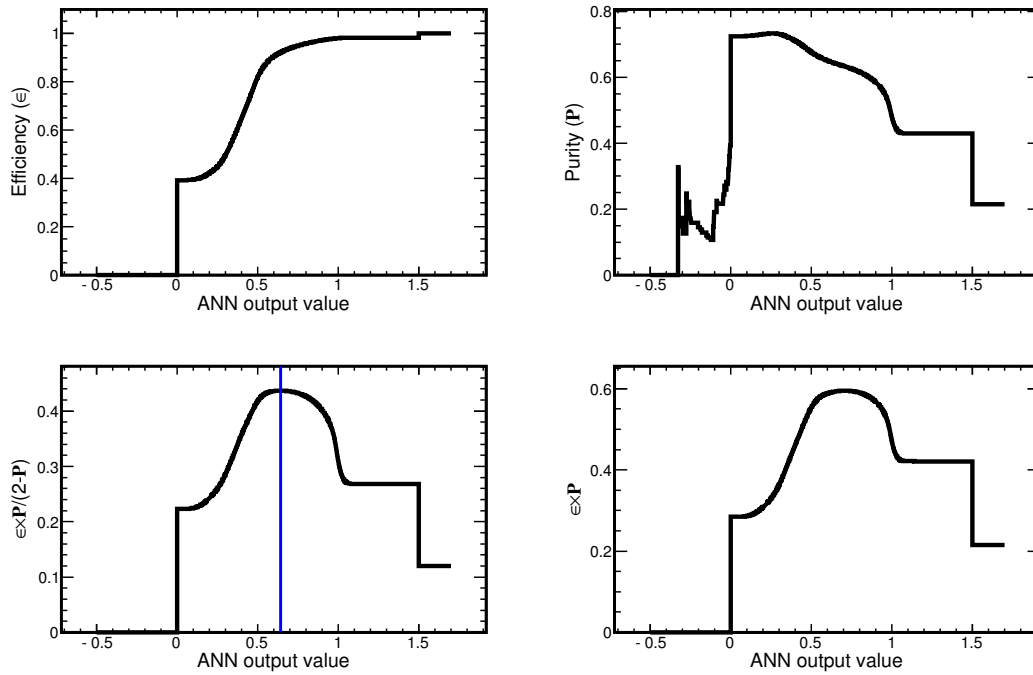
Figure 4.11: The efficiency and purity and 2 figures of merit as a function of PID. The value of the cut that maximises the figure of merit is shown.
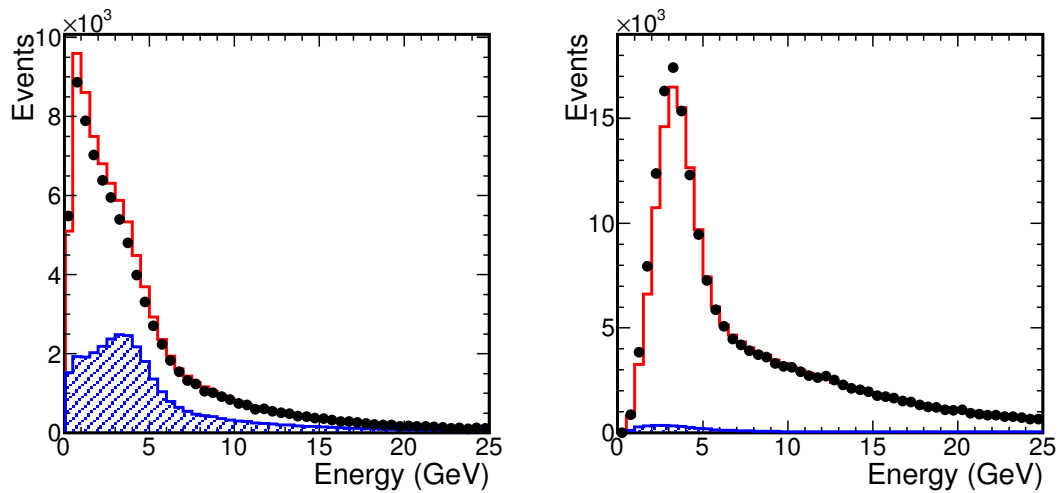
Figure 4.12: The selected NC (left) and CC (right) spectra selecting on the PID. The red line shows selected MC events. The black dots show the Near Detector data. The hatched blue areas are the selected background CC in the NC spectrum and NC in the NC spectrum.
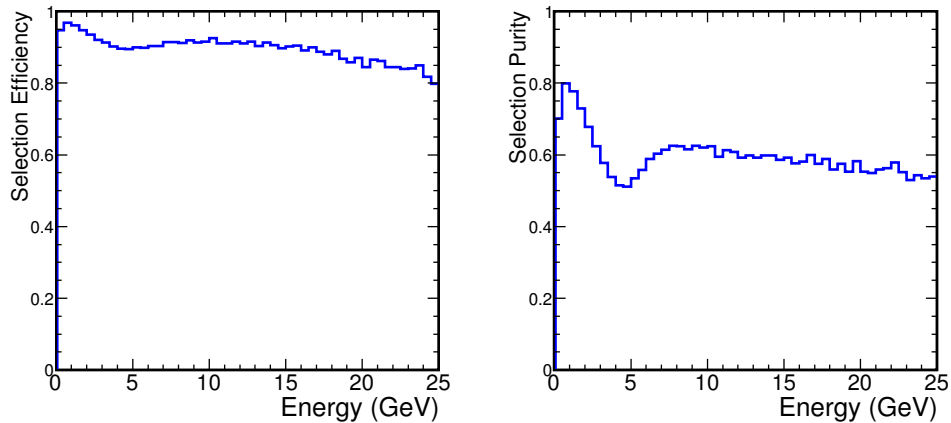
Figure 4.13: The efficiency and purity as a function of reconstructed energy.

as Figure 4.13. The efficiency is reasonably flat as a function of energy at $> 80\%$. The purity curve drops from 80% at very low energies to 50% where the peak of the CC spectrum results in the largest CC background and corresponding drop in purity at 3 GeV. At higher energies the purity increases to 60% and stays fairly constant.

4.6.2   No Track ANN

As alluded to above ANNs were designed to try and distinguish between NC and CC events reconstructed without a track. The variables used were mainly global event and shower shape quantities. Many combinations of variables were tried and the output of a typical example is shown as Figure 4.14. The efficiency, purity and figures of merit of this no track ANN as a function of cut value are shown as Figure 4.15. Which demonstrates the maximum figure of merit is to select all events. All no track ANNs developed displayed this behaviour and due to most no track events being NC, all events with no track are assigned a selection output of 0 to be automatically selected as NC. This has the advantage of increasing the statistics and maximising the sensitivity for any analysis of NC events.
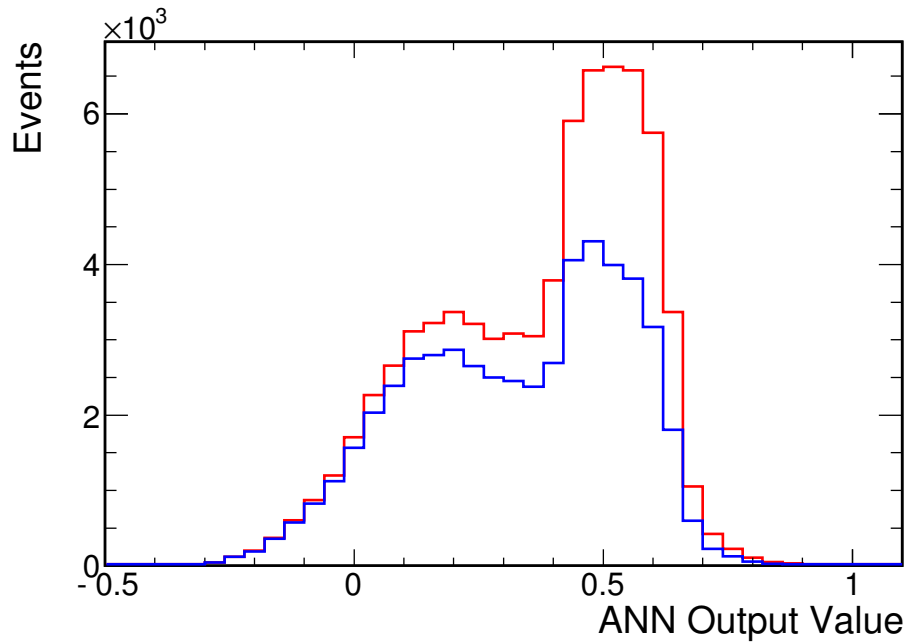
Figure 4.14: The output of the no track ANN. The red line shows the MC output with 0 being more NC like and 1 more CC like. The hatched blue area shows the true NC background

4.7   Far Detector

An analogous procedure as outlined above was performed for the Far Detector. In this case the input MC corresponded to 3.81×10^{23} POT

The output of the ANN and the total PID is shown as Figure 4.16. The plot is normalised by area. This is to mitigate against the effect of oscillations that will be present in the data and not in the MC. The difference in shape especially in the CC peak at 1 will be largely due to the presence of oscillations. Even with these considerations the agreement is good.

Efficiency and purity curves are show as Figure 4.17. As expected the Near and Far Detector networks show very similar performances. The overall efficiency is 91.1% and the overall purity is 66.0%. The maximal cut value is optimised on the nominal MC at a value of 0.633. For ease of computation and because the
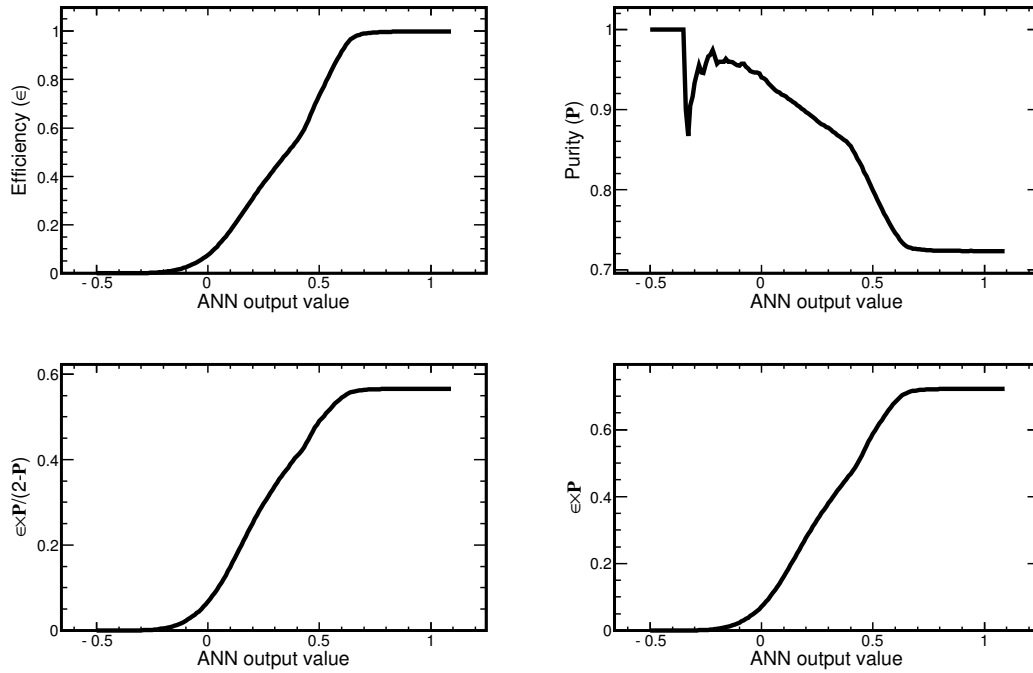
Figure 4.15: The efficiency and purity and 2 figures of merit as a function of ANN output value for a no track ANN
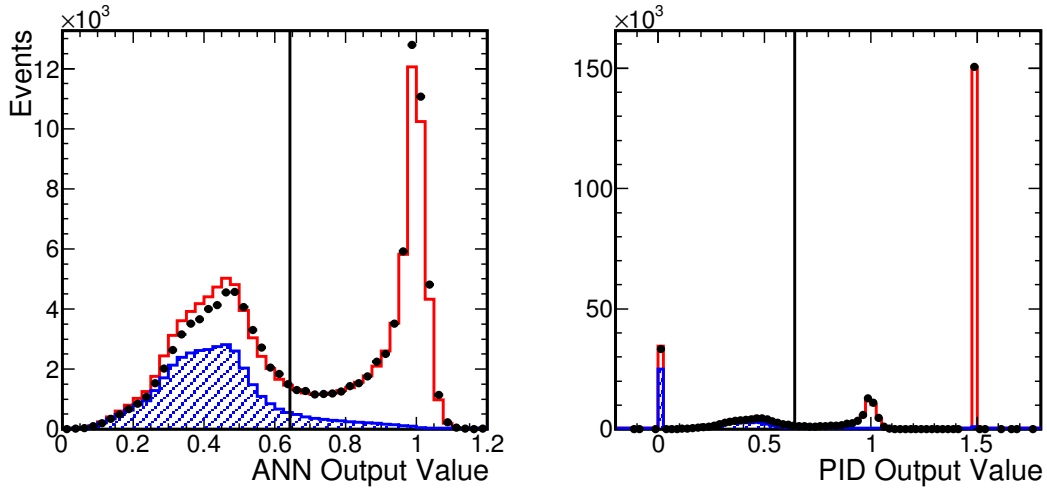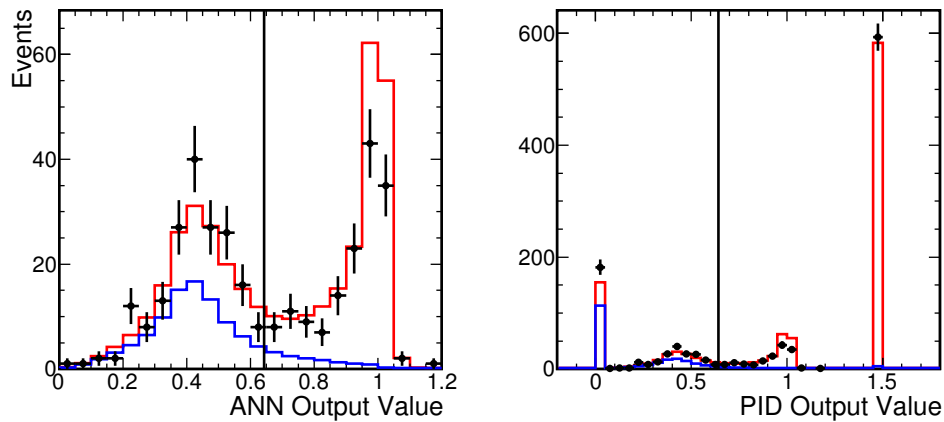

Figure 4.16: The output of the ANN and the PID. The red line shows the ANN or PID output value for MC events. The black dots show the Near Detector data. The hatched blue ares are the true NC events from the MC. The vertical line marks the position of the cut. The plot is normalised by area.
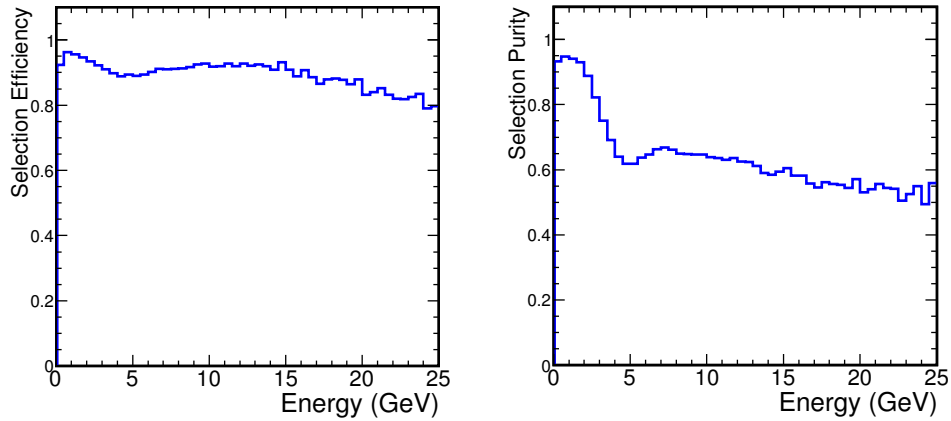
Figure 4.17: The efficiency and purity as a function of energy in the Far Detector.

figure of merit curves as a function of PID value are flat around the peak the cut value that maximises the figure of merit in the Far Detector is also used in the Near Detector. This does not change the efficiency and purity of the selection by more than a percent.

4.8 Conclusion

A procedure to select NC events in the MINOS detectors has been presented. The procedure takes place in 2 steps with a pre-classification to classify easily classified events followed by inputting into an ANN. The optimal cut position based on maximising a figure of merit of $\epsilon \times \mathbf{P}/(2 - \mathbf{P})$ for the whole PID selection was determined. This procedure has been applied to both the Near and Far Detectors. Throughout the remainder of this thesis NC and CC events have been selected using this method.

Chapter 5

Extrapolating Events between the MINOS Detectors

The major uncertainty in modelling the MINOS data is due to a lack of knowledge about the flux of neutrinos produced. As has been discussed in Section 3.9 discrepancies on the order of 30% were present before tuning the hadron production model. In this chapter we present a method that makes a Far Detector prediction based on the Near Detector measured spectrum. The core of the method is a Beam Matrix that leads to the cancellation of flux inaccuracies between the 2 detectors.

5.1 Flux Differences in the MINOS Detectors

The philosophy behind utilising 2 detectors in the MINOS experiment is to use the measured spectrum at the Near Detector to accurately predict the spectrum measured at the Far Detector in the absence of oscillations. Any differences observed between the Far Detector prediction and the measured data can be analysed by fitting various oscillation models. The major advantage of having 2 detectors is
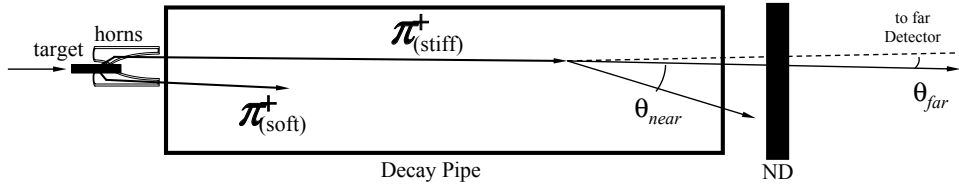
Figure 5.1: A cartoon showing the different solid angles subtended by neutrino parents decaying at different points in the decay pipe for the Near and Far Detectors. Higher energy parents travel further down the decay pipe before decaying. Figure taken from [82]

that it allows the cancellation of systematic errors common to both detectors such as the absolute neutrino flux, cross sections and track energy measurements from range.

If the flux through both detectors was identical[1] the cancellation would be exact. However the geometry of the layout of the experiment prevents this from being the case. Figure 5.1 demonstrates the different range of pion decay angles such that the resulting neutrino will pass through either the Near or Far Detector. The Far Detector subtends a very small solid angle for the decay of the parent particle. There is only one direction in which a parent can decay that will result in a neutrino that can be detected at the Far Detector.

The Near Detector by virtue of being much closer to the decay point can detect neutrinos produced in a wider range of solid angles. A specific parent can therefore produce neutrinos with a range of decay angles that will still go on to pass through the Near Detector. These neutrinos will have different energies in the Near Detector depending on the decay angle. Furthermore parents with a higher energy will, in addition to producing higher energy neutrinos, tend to decay further down the decay pipe resulting in very different solid angles to the Near Detector depending on where in the pipe the parent decays. As the angle

---

[1]aside from scale factors due to differing solid angles, detector sizes and exposures.
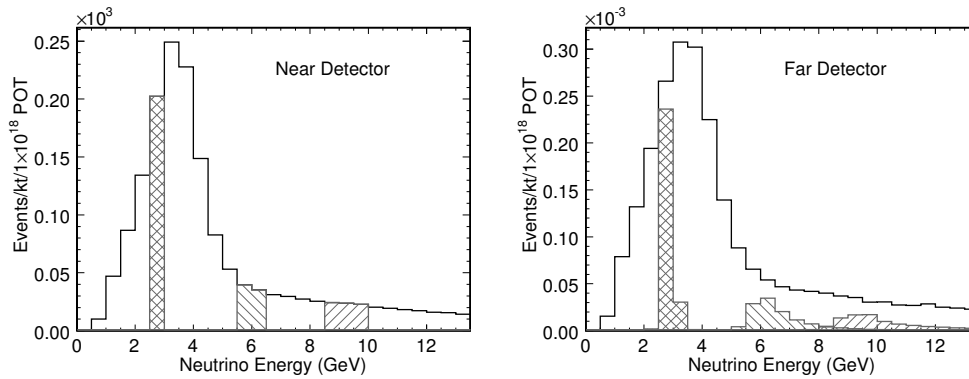
Figure 5.2: Simulated Flux in the Near(left) and Far(right) Detector. Parents that produce one of the hatched areas in the Near Detector will produce a different range of energies shown by the same type of hatched area in the Far Detector. Figure taken from [82].

the neutrino has entered the detector cannot be resolved to any real degree of accuracy the flux difference cannot be removed simply by making a solid angle cut in the Near Detector.

The effect of the decay pipe geometry in general is to lower the energy of a neutrino detected in the Near Detector relative to one detected in the Far Detector for a parent with the same energy. The neutrino will have the highest energy in the laboratory frame if it decays straight forwards. As most parents are travelling towards the Far Detector it will in general detect higher energy neutrinos for a given parent energy than in the Near Detector where decays at a small angle will still pass into the Detector. The net effect is that neutrinos from a particular parent that have an energy higher than the peak in the Far Detector end up with a lower energy in the Near Detector and are moved toward the focussing peak. Thus the Near Detector spectrum is more peaked than the Far Detector. This effect is illustrated in Figure 5.2 which shows the effect of the same parents on the simulated flux at the Near and Far Detector.

5.2   Principle of Extrapolation

To mitigate against the flux difference between the Near and Far detectors techniques have been developed to use the measured Near Detector spectrum to predict the Far Detector spectrum. This process is termed extrapolation. Many different techniques have been developed for this purpose and four such methods are outlined in [82]. Extrapolation techniques make use of 2 different procedures. The first uses the measured Near Detector data to constrain the MC prediction and then applies these corrections to the Far Detector MC to make the prediction. The second involves making a prediction at the Far Detector directly from the Near Detector by performing some conversion technique. This conversion technique will in part be based on the MC. The analysis presented here makes use of both types of techniques. The Far Detector NC and CC spectra are predicted directly from the measured CC spectrum at the Near Detector using a technique known as a Beam Matrix. The Far Detector NC prediction is then augmented by the results of a fit between the NC selected data and MC spectra at the Near Detector.

The Beam Matrix technique has been the primary extrapolation in several MINOS analyses [67, 82, 83]. A series of transformations derived from the MC are applied to the Near Detector CC spectrum to convert it to a Near Detector ν_μ flux. A specially constructed conversion matrix called a Beam Matrix then acts on the Near Detector flux to make a Far Detector flux prediction. This is then further converted back into a Far Detector prediction by reversing the transformations used in the Near Detector. The process used in this particular extrapolation is shown in Figure 5.3.

The steps are briefly summarised below to provide a quick overview of the analysis technique. The individual steps are then explained in greater detail in the subsequent sections.
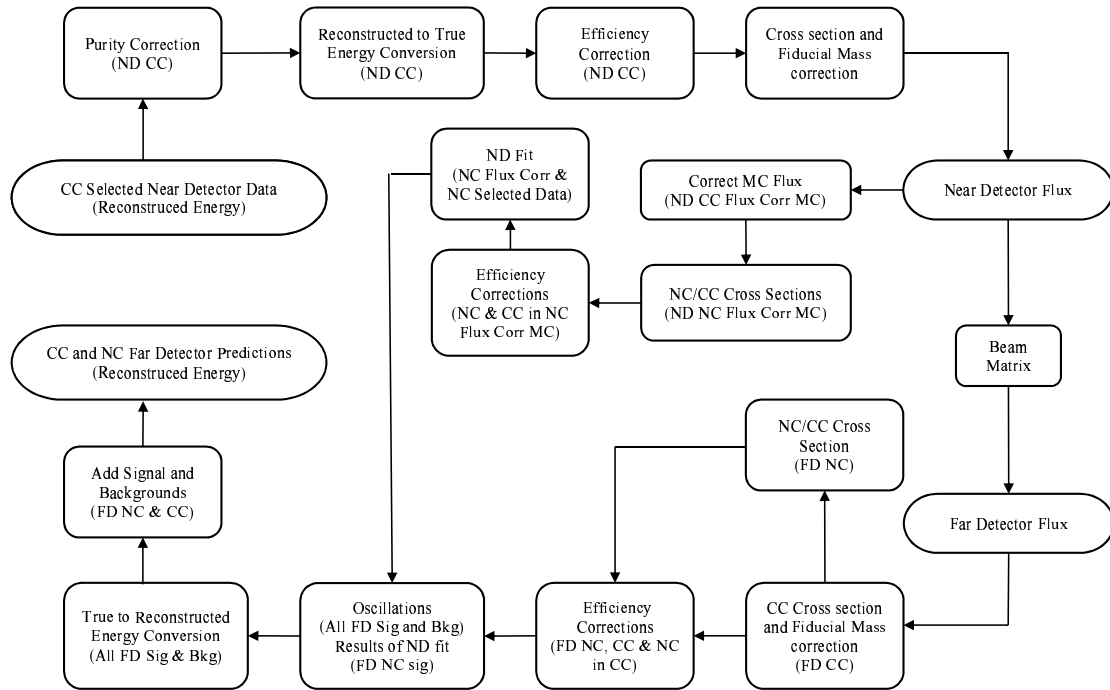
Figure 5.3: Steps outlining the extrapolation technique developed in this thesis used to make the predictions in the Far Detector.

The steps in the Beam Matrix part of the method are:

- Remove impurities from the measured Near Detector CC spectrum

- Convert the pure CC spectrum from reconstructed to true energy

- Apply Near Detector selection and acceptance efficiency corrections

- Divide by CC cross section and fiducial mass to produce a Near Detector Flux*

- Apply Beam Matrix to Near Detector Flux to obtain Far Detector Flux

- Multiply by CC cross sections and Far Detector fiducial mass

- Multiply by the ratio of NC/CC cross sections to obtain the predicted rate of NC events

- Apply Far Detector selection and acceptance efficiency corrections to NC and CC spectra

- Apply any oscillations in true energy to Signal NC, CC and all Backgrounds**

- Convert from true energy to reconstructed energy for all signal NC, CC and backgrounds.

- Sum all signal and backgrounds to obtain Far Detector CC and NC Predictions.

For reasons that will be discussed later only the CC spectrum can be directly extrapolated in this way.

In addition to the Beam Matrix part of the method a fit is performed between the Near Detector NC data and MC the results of which are applied to the Far Detector NC prediction. This proceeds with the following steps starting with starred expression in the list of Beam Matrix steps above.

- Near Detector Data Flux*

- Correct the MC predicted Flux using the data predicted Flux

- Multiply by cross sections and fiducial mass to obtain MC flux corrected NC rate

- Apply selection and acceptance efficiency corrections to obtain MC flux corrected NC prediction

- Perform a fit between the measured Near Detector Data and the flux corrected MC

- Apply the results of the fit to the Far Detector prediction at the ** stage in the Beam Matrix steps

All the steps in the combined Beam Matrix ND Fit extrapolation are described in detail below.

5.2.1 Selecting the NC and CC Spectrums

The ANN described in Chapter 4 is used to discriminate NC and CC events in both detectors. There are however additional requirements an event must satisfy other than the cleaning and fiducial requirements outlined in Chapter 4. For an event to be used in the extrapolation analysis it must have a reconstructed energy of < 120 GeV. As the protons from the Main Injector are delivered with this energy it is impossible for a neutrino to have energy greater than this and any event claiming so has some problem with the energy estimation in the reconstruction. In addition events selected as CC are required to have a track with a positive curvature in the magnetic field to select only μ^- from ν_μ events and not events with μ^+ from $\overline{\nu}_\mu$. $\overline{\nu}_\mu$ induced events are considered a background in this analysis as only ν_μ can be extrapolated by the Beam Matrix used here. They are added back in at the Far Detector with the other backgrounds and oscillations applied. Tracks in NC selected events are expected to be mis-identified tracks or not from muons and therefore have no sign cut.

5.3 Near Detector Transformations

5.3.1 Near Detector Purity Correction

The first correction performed on the measured Near Detector CC energy spectrum $(R_i^{N_{CC}})$ is to remove the non-ν_μ backgrounds. This is achieved using the MC to calculate the purity as a function of reconstructed energy $P_i^{N_{CC}}$, where i runs over the energy bins and N_{CC} indicates the correction is for Near Detector CC events.
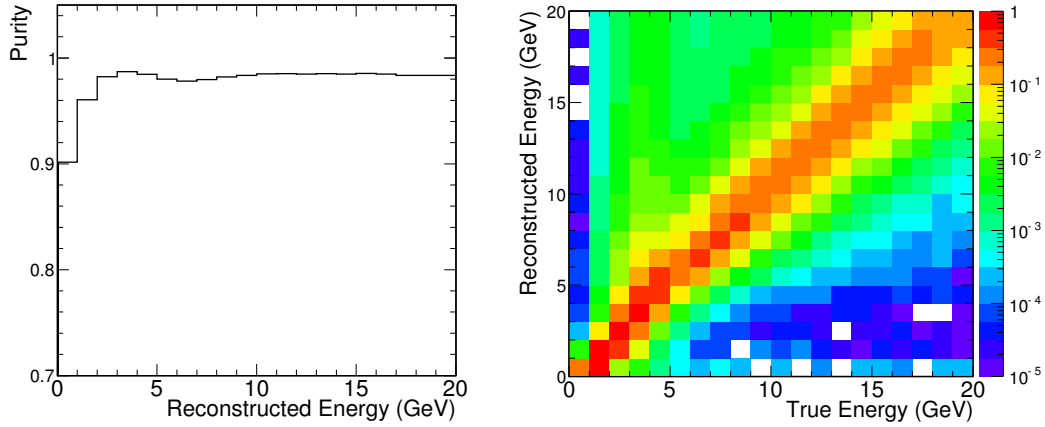
Figure 5.4: The CC Purity correction (left) and Reconstructed to True Energy Matrix (right) in the Near Detector.

This correction is calculated from the MC as:

$$P_i^{N_{CC}} = \frac{(\text{Number of CC } \nu_\mu \text{ events selected})_i}{(\text{Total number of CC events selected})_i}$$

Multiplying the CC selected reconstructed energy spectrum by this histogram gives the pure CC ν_μ energy spectrum

$$R_i^{N_{CC},P} = R_i^{N_{CC}} P_i^{N_{CC}}$$

The purity correction for the Near Detector CC events is shown in the left hand side of Figure 5.4.

5.3.2 Near Detector Reconstructed to True Energy Conversion

To transform the purity corrected energy spectrum in reconstructed energy to a spectrum in true neutrino energy $(T_i^{N_{CC}})$ requires the use of a reconstructed to true energy conversion matrix $(RT_{ij}^{N_{CC}})$. This matrix should in theory be the inverse

of the true to reconstructed conversion matrix $(TR_{ij}^{N_{CC}})^{-1}$. However applying the inverted True to Reconstructed energy matrix is non trivial. Large fluctuations in the true energy prediction will result from small statistical fluctuations in reconstructed energy in the inverted matrix. This problem is resolved by approximating the inverted matrix $(TR_{ij}^{N_{CC}})^{-1}$ with the transpose matrix $RT_{ij}^{N_{CC}}$. This approximation is valid provided that the matrix is nearly diagonal which is the case for CC events. For NC events as will be discussed later the true to reconstructed matrix is very non-diagonal and thus this conversion cannot be done this way. It is for this reason that the Near Detector NC spectrum cannot be extrapolated in the same way as the CC spectrum.

This approximate conversion matrix is constructed from the MC by filling a 2 dimensional histogram $(M_{ij}^{N_{CC}})$ with one axis (i) being the reconstructed energy and the other (j) being the true neutrino energy for each selected MC signal event. To be used as the conversion matrix this histogram has to be correctly normalised such that when applied to the reconstructed energy spectrum each event in reconstructed energy produces one event in true energy.

This normalisation is achieved by scaling every bin in a column i of reconstructed energy by a normalisation factor $N_i^{N_{CC}}$ such that the bins in each column sum to 1. The reconstructed to true conversion matrix is therefore given by

$$RT_{ij}^{N_{CC}} = \frac{M_{ij}^{N_{CC}}}{N_i^{N_{CC}}}$$

The conversion is applied by taking each bin of the pure reconstructed energy spectrum $R_i^{N_{CC},P}$ and multiplying by each bin of the column of the conversion matrix that corresponds to that reconstructed energy. This resulting product $(RT_{ij}^{N_{CC}} R_i^{N_{CC},P})$ is the contribution of the particular bin of $R_i^{N_{CC},P}$ to the j bin of the selected CC true Energy Spectrum $T_i^{N_{CC},S}$. By repeating this for every bin i

and summing the results, the CC true Energy Spectrum is calculated as:

$$T_i^{N_{CC},S} = \sum_i RT_{ij}^{N_{CC}} R_i^{N_{CC},P}$$

The reconstructed to true energy conversion matrix is also shown in Figure 5.4.

5.3.3 Near Detector Efficiency Corrections

There are 2 levels of efficiency correction applied to the selected true energy spectrum: Selection Efficiency and Reconstruction Efficiency. The Selection Efficiency corrects for the ANN not being 100% efficient in separating NC and CC events and for the effect of the cleaning outlined in Chapter 4. It corrects the selected CC spectrum to produce the spectrum of all CC events reconstructed in the Near Detector

$$E_i^{N_{CC},S} = \frac{(\text{Number of true } \nu_\mu \text{ CC events selected})_i}{(\text{total number of true } \nu_\mu \text{ CC events reconstructed})_i}$$

The resulting spectrum still needs to be corrected for the reconstruction efficiency to take account of failures in the reconstruction that result in some events that interacted in the fiducial volume of the detector not being reconstructed. Due to the possibility of events that really took place within the fiducial volume being reconstructed outside the volume it is possible for this correction to be > 1.

$$E_i^{N_{CC},R} = \frac{(\text{total number of true } \nu_\mu \text{ CC events reconstructed})_i}{(\text{actual number of true } \nu_\mu \text{ CC neutrino interactions in the fiducial volume})_i}$$

The histograms are applied sequentially to provide the spectrum of all ν_μ events
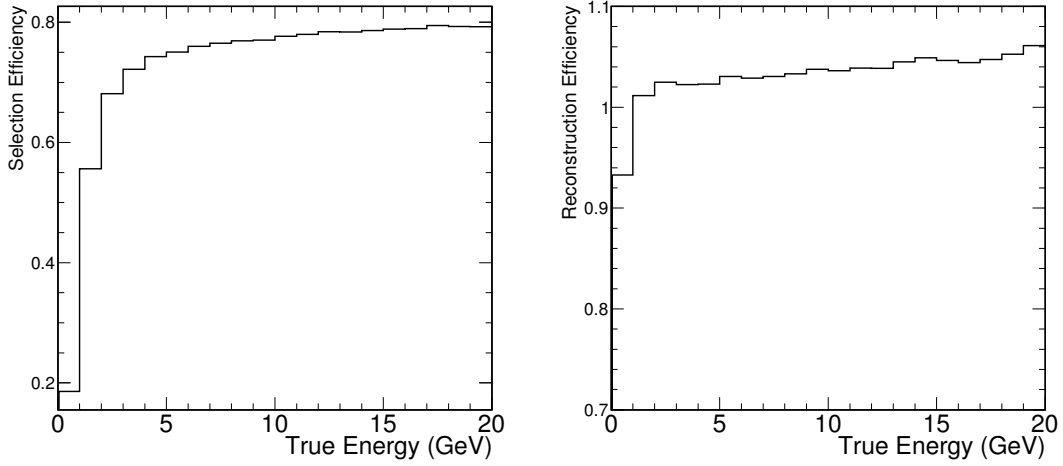
Figure 5.5: Selection Efficiency Correction (left) and Reconstruction Efficiency (right) as a function of true energy for ν_μ CC events in the Near Detector.

that interact in the Near Detector fiducial volume in true energy.

$$T_i^{N_{CC},R} = \frac{T_i^{N_{CC},S}}{E_i^{N_{CC},S}} \qquad T_i^{N_{CC}} = \frac{T_i^{N_{CC},R}}{E_i^{N_{CC},R}}$$

The efficiency correction histograms are shown in Figure 5.5

5.3.4   Near Detector Flux Calculation

To calculate the ν_μ flux at the Near Detector the efficiency corrected spectrum must be corrected for cross sections and the fiducial mass. Using a proton on target (POT) exposure of P_N and a fiducial mass of M_N the flux through the Near Detector per proton on target is given by:

$$\Phi_i^{N_{CC}} = \frac{T_i^{N_{CC}}}{\sigma_{CC} M_N P_N}$$

The Near Detector Fiducial Mass is 27 tonnes and the exposure depends on the run period considered. In practice the cross section is not applied at this stage

of the extrapolation but is actually folded into the calculation of the Beam Matrix described in the next section.

5.3.5   Constructing the Beam Matrix

The Beam Matrix is constructed with reference to the decay kinematics of the neutrino parent particles provided from the Fluka05 simulation of the beam. The intended purpose is to predict the flux of neutrinos at the Far Detector given the measured flux of neutrinos at the Near Detector.

Neutrino Flux at the Near Detector

The output of the simulation of the NuMI beam contains the kinematic information of every neutrino parent particle that decayed in the decay pipe.

The parent particles that contribute most to the muon neutrino flux are positive pions and kaons with a smaller contribution from muons. These are the only parents considered in the construction of the Beam Matrix. The decays that lead to the muon neutrino flux are therefore:

$$\pi^+ \rightarrow \mu^+ + \nu_\mu$$

$$K^+ \rightarrow \mu^+ + \nu_\mu$$

$$\mu^- \rightarrow e^- + \overline{\nu}_e + \nu_\mu$$

Where the μ^- come from π^- and K^- decays. To construct the Near Detector energy spectrum from the decaying parents each parent particle is decayed in such a way that the resulting neutrino travels towards a randomly chosen point within the fiducial volume of the Near Detector (r_N). Each parent is decayed in this way

10 times. Thus a range of decay angles (and hence resulting neutrino energies) in the Near Detector is covered for each parent.

Once r_N is known the energy of the neutrino can be calculated. In the centre of mass (CM) frame of the parent the Neutrino energy $E^{CM}_{\nu_\mu,N}$ is found from the results for 2 body decay neglecting the neutrino mass:

$$E^{CM}_{\nu,N} = \frac{m_\mu - m_p}{2m_p}$$

Moving into the lab frame the angle between the parent and neutrino direction of flight is given by:

$$\cos\theta = \frac{(r_N - r_d) \cdot \mathbf{p_p}}{|r_N - r_d||\mathbf{p_p}|}$$

Where r_d stands for the parent decay point and $|\mathbf{p_p}|$ is the parent 3 momentum.

Equating invariants leads to an expression for the lab energy of the neutrino in terms of the CM energy as follows

$$E_p E_{\nu,N} - \mathbf{p_p} \cdot \mathbf{p_\nu} = E^{CM}_p E^{CM}_{\nu,N} - \mathbf{p^{CM}_p} \mathbf{p^{CM}_\nu}$$

$$E_p E_{\nu,N} - \cos\theta |\mathbf{p_p}||\mathbf{p_\nu}| = m_p E^{CM}_{\nu,N} - 0$$

Rearranging, dividing by m_p and using that $E_{\nu,N} = |\mathbf{p_\nu}|$, $\gamma = E/m$ and $\beta = |\mathbf{p}|/m\gamma$ gives:

$$E_{\nu,N} = \frac{E^{CM}_{\nu,N}}{\gamma_p(1 - \beta_p \cos\theta)}$$

In this way the true energy in the Near Detector of every neutrino from a parent decay can be calculated.

The probability that a parent will decay to result in a neutrino passing through the Near Detector is related to the angular distribution of the parent decays. Pions

and kaons are spinless and therefore decay isotropically in their own rest frames. This is usefully expressed as

$$\frac{\mathrm{d}N}{\mathrm{d}\cos\theta_{CM}} = \frac{1}{2} \tag{5.1}$$

Where N is the number of decays, θ_{CM} is the angle between the neutrino momentum and an arbitrary axis in the CM frame and the $\frac{1}{2}$ is a result of properly normalising.

Muon Spin Calculation

For neutrinos due to muon decay the situation is complicated by the muon spin causing the angular distribution $\mathrm{d}N/\mathrm{d}\cos\theta_{CM}$ to be no longer isotropic. The muons are themselves produced with a neutrino in 2 body pion or kaon decay[2]. The ν_μ produced must be left handed. The spin of the muon must be aligned so that angular momentum will be conserved. This means in the muon rest frame the muon spin is opposite to the direction of the incoming pion.

It can be shown (for example in [84]) that in the muon rest frame the normalised angular distribution of decays, as a function of the angle between the momentum of the produced neutrino and the muon spin θ_{CM}^π (and hence the pion momentum which is in the opposite direction to the muon spin) is:

$$\frac{\mathrm{d}N_\mu}{\mathrm{d}\cos\theta_{CM}^\pi} = \frac{1}{2}\left(1 - \frac{1-2x}{3-2x}\cos\theta_{CM}^\pi\right) \tag{5.2}$$

Where $x = E_\nu/E_\nu^{\mathrm{MAX}}$ with E_ν being the energy of the neutrino and E_ν^{MAX} being the maximum possible energy of the neutrino ($m_\mu/2$ in this case).

---

[2]For simplicity a pion decay will be assumed.

Transforming into the Laboratory Frame

The angular distributions have been calculated in the parent rest frame. To be used in constructing the Beam Matrix they must be transformed into the lab frame. This can be achieved using the transformation

$$\frac{\mathrm{d}N}{\mathrm{d}\cos\theta} = \frac{\mathrm{d}N}{\mathrm{d}\cos\theta_{CM}} \frac{\mathrm{d}\cos\theta_{CM}}{\mathrm{d}\cos\theta} \tag{5.3}$$

$\frac{\mathrm{d}N}{\mathrm{d}\cos\theta_{CM}}$ has been calculated in Equations 5.1 and 5.2. Defining θ as the angle between the neutrino and parent momentum and again treating the neutrinos as massless so that $E_\nu = |\mathbf{p}_\nu|$ then it follows that:

$$\cos\theta = \frac{p_\|}{E_\nu} \qquad \cos\theta_{CM} = \frac{p_\|^{CM}}{E_\nu^{CM}} \tag{5.4}$$

An expression for $\cos\theta_{CM}$ as a function of $\cos\theta$ can then be obtained by performing the Lorentz transformations from the CM to lab frame as follows:

$$p_\|^{CM} = \gamma_p \left(p_\| - \beta_p E_\nu \right) \qquad E_\nu^{CM} = \gamma_p \left(E_\nu - \beta_p p_\| \right)$$

Where γ_p and β_p refer to the parent in the lab frame. Substituting these expressions into Equation 5.4 expression and dividing by E_ν gives

$$\cos\theta_{CM} = \frac{\cos\theta - \beta_p}{1 - \beta_p \cos\theta}$$

Leading to the desired result:

$$\frac{\mathrm{d}\cos\theta_{CM}}{\mathrm{d}\cos\theta} = \frac{1}{1 - \beta_p \cos\theta} + \beta_p \frac{\cos\theta - \beta_p}{(1 - \beta_p \cos\theta)^2} \tag{5.5}$$

$$= \frac{1 - \beta_p^2}{(1 - \beta_p \cos\theta)^2} \tag{5.6}$$

$$= \frac{1}{\gamma^2 (1 - \beta_p \cos\theta)^2} \tag{5.7}$$

Where in the final step $\gamma^2 = (1 - \beta)^{-2}$ has been used.

Hence for pion or kaon decay the angular distribution of neutrino decays can be obtained by substituting Equation 5.7 and Equation 5.1 into Equation 5.3 to obtain:

$$\frac{\mathrm{d}N}{\mathrm{d}\cos\theta} = \frac{1}{2\gamma^2 (1 - \beta_p \cos\theta)^2}$$

and using Equation 5.2 for muon decay to get:

$$\frac{\mathrm{d}N}{\mathrm{d}\cos\theta} = \left(1 - \frac{1 - 2x}{3 - 2x} \cos\theta_{CM}^\pi\right) \frac{1}{2\gamma^2 (1 - \beta_p \cos\theta)^2}$$

Near Detector Flux

Having obtained the angular distributions of the parent decays in the previous section the probability of a parent decaying to produce a neutrino that will reach the Near Detector can now be calculated.

To obtain the flux at the Near Detector the probability that a particular parent k decays to produce a neutrino that passes through a slice of the Near Detector face such that it will have a particular Near Detector energy (E) is:

$$P_k(\nu \text{ travel through slice}) = \frac{1}{2\pi} \int_{slice} \frac{\mathrm{d}N}{\mathrm{d}\cos\theta} \mathrm{d}\Omega_E$$

Where Ω_E is the range of solid angles for which the neutrino will have the correct energy and $\mathrm{d}\Omega_E$ indicates that the integration takes place only over this range of solid angles.

By choosing random points in the Near Detector Fiducial volume and decaying parents towards that point the above integral is effectively being evaluated numerically. As was mentioned previously each parent is decayed 10 times with each decay being treated as due to a unique parent. This approach is valid provided the sample of parents is large enough that there are many other kinematically similar parents for each parent used.

The flux per unit area of neutrinos of the correct energy through the Near Detector slice for a parent is then given by:

$$F_k = \frac{P_k}{\Omega_E} = \frac{1}{2\pi} \frac{\mathrm{d}N}{\mathrm{d}\cos\theta}\bigg|_{\cos\theta_k}$$

The rate of neutrinos passing through a unit area A in the Near Detector slice due to parent k is therefore $F_k A$. If in particular we choose the unit area A to be the same as when the calculation of the Far Detector flux is performed it will usefully cancel when the final Beam Matrix is normalised. To find the total rate of neutrinos due to every parent rather than just parent k, F_k must be summed over all parents. It should be noted that the parent can be decayed to anywhere within the fiducial volume and not just into a particular slice. The flux through a slice will vary with the distance z into the detector the slice is at. This is due to the different range of decay angles resulting in neutrinos with different energies at different z. This means that what is actually being calculated is the flux averaged over the entire fiducial volume. This is the desired result as this is what is measured from the data.

The result that will be required later is not the total neutrino flux due to all

parents that would be obtained by summing F_k for all parents, but the flux of neutrinos of a certain energy, that will belong in an energy bin i. This can be found by only summing over the parents that produced a neutrino in the Near Detector with that energy.

The flux at the Near Detector for neutrinos of a given energy i is therefore

$$N_i = \sum_k F_k A = \frac{1}{2\pi} \sum_k \left. \frac{\mathrm{d}N}{\mathrm{d}\cos\theta} \right|_{\cos\theta k} A \tag{5.8}$$

Neutrino Flux at the Far Detector

In a similar way the contribution of each parent to the flux at the Far Detector can now be calculated. As the Far Detector is 735 km away the solid angle subtended to a decaying parent in the decay pipe is negligible. Thus the range of decay angles between the parent and neutrino which will allow it to reach the Far Detector is consequently very small. The kinematics of this mean that for a given parent the energy of the neutrino at the Far Detector is essentially always the same value regardless of where it decays. The same analysis as performed in the Near Detector applies here resulting in the neutrino at the Far Detector having energy

$$E_{\nu,F} = \frac{E_{\nu,F}^{CM}}{\gamma_p(1 - \beta_p \cos\theta_C)}$$

where θ_C is the angle in the lab frame between the parent momentum and the centre of the Far Detector.

Far Detector Neutrino Flux

Having obtained the angular distributions of the parent decays in the previous section the probability of a parent decaying to produce a neutrino that will reach the Far Detector can now be calculated. In particular the probability that the neutrino

passes through an area A on the front face of the Far Detector $P(\nu_\mu \text{travels to } A)$ is calculated.

$P(\nu_\mu \text{travels to } A)$ is obtained by integrating the relevant normalised angular distribution over the solid angle subtended by A to the decay point:

$$P(\nu_\mu \text{travels to } A) = \frac{1}{2\pi} \int_A \frac{dN}{d\cos\theta} d\Omega$$

The $\frac{1}{2\pi}$ is a normalisation factor to make the integral one and makes use of the fact that the angular distribution has no dependence on the azimuthal decay angle. As the Far Detector is so far away the solid angle subtended by A (Ω_A) is very small and therefore the angular distribution can be assumed to be constant over A. The integral can then be approximated by:

$$\begin{aligned} P(\nu_\mu \text{travels to } A) &= \frac{1}{2\pi} \frac{dN}{d\cos\theta} \Big|_{\cos\theta=\cos\theta_C} \Omega_A \\ &\approx \frac{1}{2\pi} \frac{dN}{d\cos\theta} \Big|_{\cos\theta=\cos\theta_C} \frac{A}{d_{FD}^2} \end{aligned}$$

Where d_{FD}^2 is the distance from the decay point to the Far Detector.

Constructing the Beam Matrix

Using the results obtained in the previous sections the Far Detector flux due to each parent can be calculated.

To make the Beam Matrix a 2-dimensional histogram is used with an x-axis of neutrino energy in the Near Detector and a y-axis with the neutrino energy in the Far Detector.

The histogram is filled by taking a parent that has produced a neutrino of a certain energy in the Near Detector and finding the column of the 2 dimensional

histogram that corresponds to that energy. For this parent the energy of the neutrino that parent would produce if decayed to the Far Detector is found and the corresponding entry in the row for that Far Detector neutrino energy is filled with the probability that this neutrino will pass through the Far Detector.

The contribution from the entire parent sample is then found by repeating this process for every parent used to produce the flux.

As was previously mentioned the cross section for CC events is folded into the construction of the Beam Matrix. This is achieved by multiplying by the cross section evaluated at the parent energy as the parent fluxes are filled. This evaluation is done by interpolating between the nearest cross section calculations for a given parent energy. The cross section calculations are provided with a resolution of 0.1 GeV.

After every parent has been used to fill the histogram the total neutrino flux at the Far Detector produced by the input simulated parent flux can be found by summing over the fluxes in each column.

When using this 2-dimensional histogram as the Beam Matrix it must be corrected to be consistent with the flux measured at the Near Detector. If the sum of the parents that contributed to a particular column i in Near Detector Energy energy is N_i and the input measured Near Detector flux that is to be converted to the Far Detector flux has M_i events of that energy then each entry in the ith column must be scaled by the M_i/N_i ratio for that column before the columns are then summed to provide the Far Detector prediction. In the application of the Beam Matrix M_i is obtained from the result of applying the transformations in the Near Detector described earlier. N_i is evaluated by taking the expression calculated in Section 5.3.5 for the flux of neutrinos for the Near Detector of the appropriate energy and summing them.
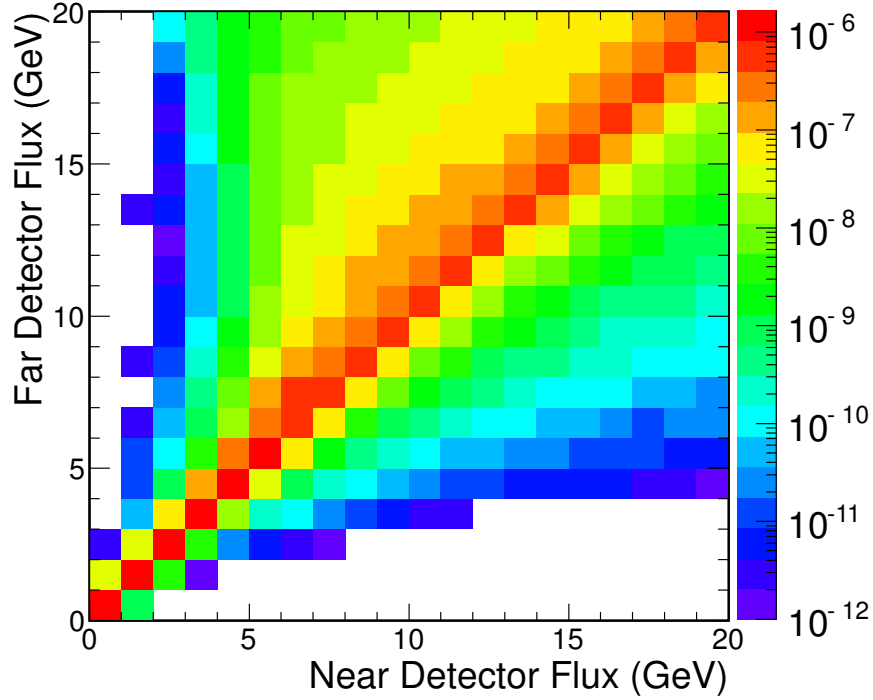
Figure 5.6: The Beam Matrix to convert a Near Detector neutrino flux to a Far Detector neutrino flux. The full Beam Matrix energy range is 0 to 120 GeV.

Every column of the two dimensional histogram described earlier can now be scaled by dividing by N_i. This results in a histogram normalised such that each column of Far Detector flux corresponds to one neutrino in the Near Detector. The factor of A from the Far Detector probability has been cancelled by dividing by N_i. The 2 dimensional histogram has now become the desired Beam Matrix to predict a Far Detector flux from a Near Detector flux. The Beam Matrix is calculated for the full energy range 0 to 120 GeV and the low energy region is shown as Figure 5.6. The region shown (0 to 20 GeV) is mainly due to pion decays. The kaon decays generally contribute at higher energies.

5.3.6   Applying the Beam Matrix

Now that the Beam Matrix (BM_{ij}) has been constructed a prediction of the Far Detector CC ν_μ flux Φ_i^{FCC} can be found by application of the Beam Matrix to the Near Detector CC ν_μ flux Φ_i^{NCC}. In this context it is useful to consider Φ_i^{NCC} as being the average measured flux of neutrinos passing through a slice of the Near Detector fiducial volume in any given energy bin i. Φ_i^{FCC} can then be obtained by multiplying each column of the Beam Matrix by Φ_i^{NCC} and summing the results to give:

$$\Phi_j^{FCC} = \sum_i \Phi_i^{NCC} BM_{ij}$$

Where j runs over the Far Detector energy bins and i runs over the Near Detector energy bins. As the Near Detector Flux was normalised to an exposure of 1 POT so will the Far Detector Flux prediction.

5.4   Far Detector Transformations

With a prediction of the Far Detector flux the operations performed at the Near Detector can be performed in reverse to provide a Far Detector prediction. The major difference in the Far Detector is that fitting for the expected neutrino oscillations will affect the predictions of both signal and background events.

Representing the mass of the Far Detector as M_F and the POT exposure at the Far Detector as P_F, the true energy spectrum of all ν_μ CC events that interact in the Fiducial Volume at the Far Detector can be calculated as:

$$T_i^{FCC} = \Phi_i^{FCC} \sigma_{CC} M_F P_F$$
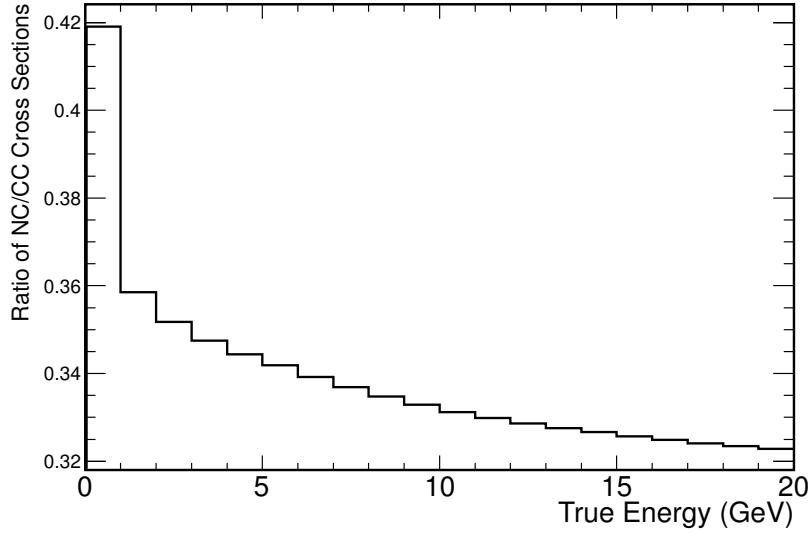
Figure 5.7: Ratio of NC/CC Cross Section as a function of true energy for events at the Far Detector.

The mass of the Far Detector fiducial volume has been calculated as 3.73 kt and the POT exposure depends on the run period being used.

5.4.1 Predicting the NC Rate from the CC Rate

Using the CC rate a prediction of the NC rate at the Far Detector can be obtained. The predicted true energy spectrum of all ν_μ NC events that interact in the Fiducial Volume can be found from

$$T_i^{F_{NC}} = T_i^{F_{CC}} \frac{\sigma_{NC}}{\sigma_{CC}}$$

The ratio of cross sections as a function of true energy is shown as Figure 5.7. Performing the transformations used at the Near Detector in reverse for the NC events will provide a prediction for the NC spectrum.
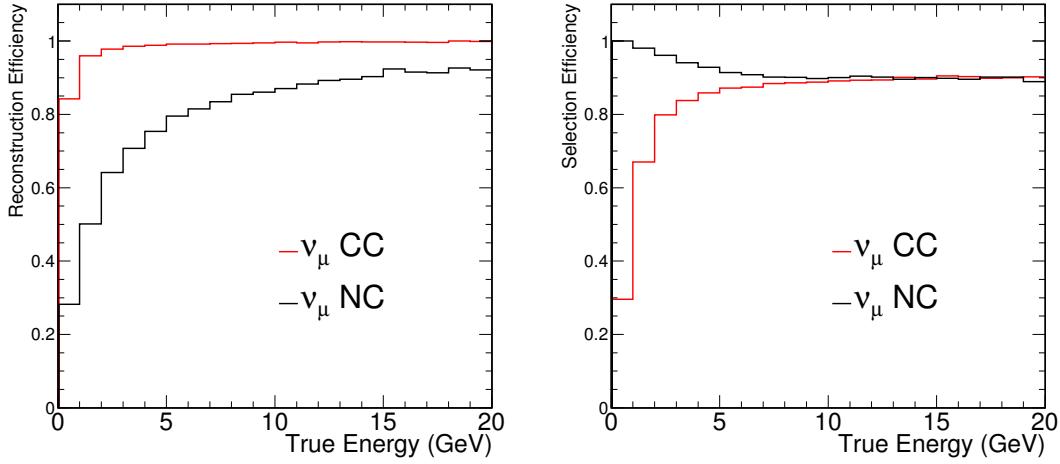
Figure 5.8: Reconstruction Efficiency (left) and Selection Efficiency Correction (right) as a function of true energy for NC(black) and CC(red) events at the Far Detector.

5.4.2 Efficiency Corrections

As in the Near Detector two steps of Efficiency correction are applied in the Far Detector but in this case for both NC and CC spectra. The reconstruction efficiency is calculated as:

$$E_i^{F_{NCC},R} = \frac{(\text{total number of true } \nu_\mu \text{ NCC events reconstructed})_i}{(\text{actual number of true } \nu_\mu \text{ NCC neutrino interactions in the fiducial volume})_i}$$

Where NCC will from now on be used to refer to either NC or CC events. The reconstruction efficiency corrections are shown in the left side of Figure 5.8. As can be seen in the Figure the corrections are quite different. This is a reflection of the reconstruction algorithm being less efficient at finding NC events and a reflection that the NC events are effected by the Far Detector Data Cleaning outlined in Chapter 4 to a much greater extent than the CC events.

The selection efficiency is defined as:

$$E_i^{F_{NCC},S} = \frac{(\text{number of true } \nu_\mu \text{ NCC events selected})_i}{(\text{total number of true } \nu_\mu \text{ NCC events reconstructed})_i}$$

The selection efficiency corrections for both NC and CC events are shown in the right side of Figure 5.8. The corrections are again quite different for NC and CC events. This correction shows that low energy CC events are hard to distinguish from actual NC events. The efficiency corrections are again applied sequentially to provide a pure selected spectra as a function of true energy

$$T_i^{F_{NCC},R} = T_i^{F_{NCC}} E_i^{F_{NCC},R} \qquad T_i^{F_{NCC},S} = T_i^{F_{NCC},R} E_i^{F_{NCC},S}$$

5.4.3 Oscillations and True to Reconstructed Energy Conversion

As all the transformations applied to the Far Detector flux up to this point are multiplicative the order in which they are applied is essentially arbitrary. Any oscillations that wish to be applied to the components of the final prediction are a function of true energy. Oscillations must therefore be applied before any true to reconstructed energy conversion. Oscillations must be applied to background events as well as signal and the procedure for this will be described later in the chapter.

For the signal events the true to reconstructed energy conversion is achieved by producing a true to reconstructed energy conversion matrix (TR_{ij}) analogous to that used in the Near Detector with the true and reconstructed energy events reversed. The application of these matrices are unaffected by the presence of oscillations due to each column of true energy being normalised to 1 event. Oscillations would effect the number of events in each bin and has thus been negated by the

normalisation. To ensure that the resolution of the oscillations is properly sampled at low energies the TR matrix has 1000 bins in true energy with a variable bin size as shown in Table 5.1.

Energy Range (GeV)	0-2	2-20	20-40	40-120
Bin Size (GeV)	0.01	0.025	0.5	2.0

Table 5.1: The binning scheme in true energy that oscillations are applied to in the Far Detector

The oscillations probabilities are calculated with the true energy at the centre of a bin and the result applied to the TR matrix. The TR matrix is then re-binned so that each axis is the same as the reconstructed energy binning scheme and the selected NCC signal spectrum in reconstructed energy is given as:

$$R_i^{F_{NCC},P} = \sum_i T_i^{F_{NCC},S} TR_{ij}^{F_{NCC}}$$

The nominal true to reconstructed energy matrices for the NC and CC signal spectra after re-binning are shown as Figure 5.9. The matrices are quite different. For CC events all the energy of the incident neutrino is deposited in the detector and therefore the reconstructed energy is a good estimate of the true energy and so the CC matrix is quite diagonal. For NC events only a portion of the neutrino energy is deposited in the detector with the rest being carried away by the neutrino. The Figure clearly shows that a neutrino with a certain true energy can contribute to any bin of reconstructed energy less than the true energy. This results in a very non-diagonal matrix. It is for this reason that the NC spectrum cannot be directly extrapolated from the Near Detector data in the same way the CC spectrum is. Constructing the reconstructed to true energy conversion matrix in the Near Detector in the way described in Section 5.3.2 will not work for the NC spectrum as this matrix will be a poor representation of the inverse matrix that
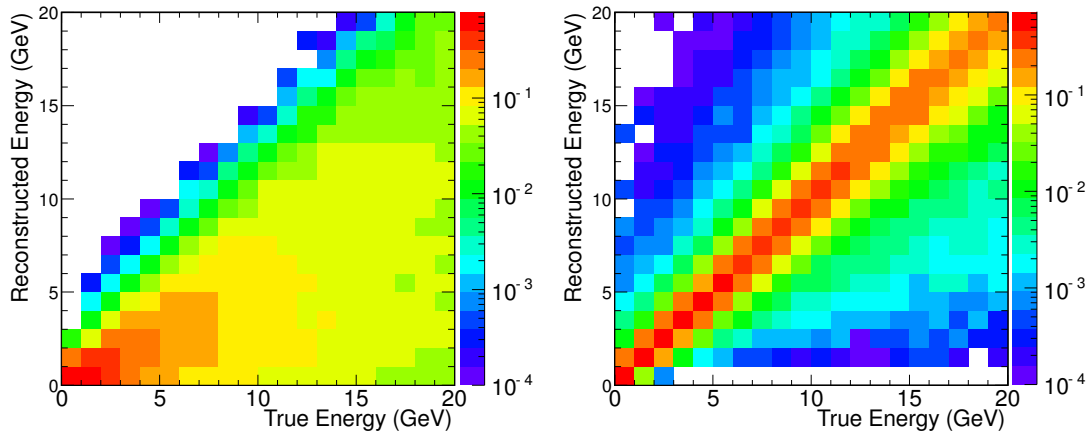
Figure 5.9: Nominal True to Reconstructed Energy Matrices for NC(left) and CC(right) events at the FD after re-binning.

does the true to reconstructed energy conversion. This is a point that will be discussed further in the section on the Near Detector fit.

Oscillating Backgrounds

The NC and CC backgrounds are treated in a similar way to the signals. Using the FD Monte Carlo a true to reconstructed energy histogram with the same variable size binning scheme in true energy is constructed for each background. The calculated oscillation probabilities are applied and the reconstructed energy predictions obtained in the same way. This is the only possible approach for ν_e and $\overline{\nu}_\mu$ originating in the NuMI beam without extrapolating these backgrounds separately. As these backgrounds form only $3(\approx 0)\%$ and $5(0.2)\%$ respectively of the total predicted NC(CC) signal at typical oscillation parameters the MC only approach is considered sufficient. The ν_τ appearance background due to oscillations leads to a background from either ν_τ NC interactions in the NC case or from ν_τ CC interactions leading to $\tau \to \mu\nu_\mu\nu_\tau$ decays[3] with the resulting μ

---
[3]The ν_τ decays this way $\approx 20\%$ of the time.

leading to mis-identified CC interactions.

This could be explicitly calculated from the ν_μ CC flux and fitted oscillation parameters but considering that it is only $\approx 1.5\%$ of the NC interactions and $\approx 0.2\%$ of the CC signal the MC only approach is considered accurate enough.

In a similar way using a non 0 value of θ_{13} will result in ν_e appearance at the Far Detector and a consequent mainly NC background. As will be described in Chapter 7, θ_{13} is either 0 or fixed 0.21 which is the CHOOZ limit at the MINOS best fit Δm^2_{32}. This is also small enough to treat with the MC only technique making up only 3% of the NC and $\approx 0\%$ of the CC prediction.

The remaining backgrounds are mis-identified signal events; either NC events in the CC spectrum or CC events in the NC spectrum. The NC background in the CC events is $\approx 0.9\%$ and is therefore treated as the other small backgrounds with an MC only prediction.

The only large background is the CC selected events in the NC spectrum. This is significant ($\approx 28\%$ of the selected spectrum at typical oscillation values) and is therefore treated differently. Using the Far Detector reconstruction efficiency corrected CC prediction a selection efficiency histogram for predicting the number of CC events in the NC prediction can be made as follows:

$$E_i^{F_{CCinNC},S} = \frac{(\text{Number of events selected as NC})_i}{(\text{total number of } \nu_\mu \text{ CC events reconstructed})_i}$$

This allows a prediction in true energy of the CC selected as NC background:

$$T_i^{F_{CCinNC},S} = T_i^{F_{CC},R} E_i^{F_{CCinNC},S}$$

Applying this to the true to reconstructed energy Matrix for the CC selected as NC background provides the background as a function of reconstructed energy.
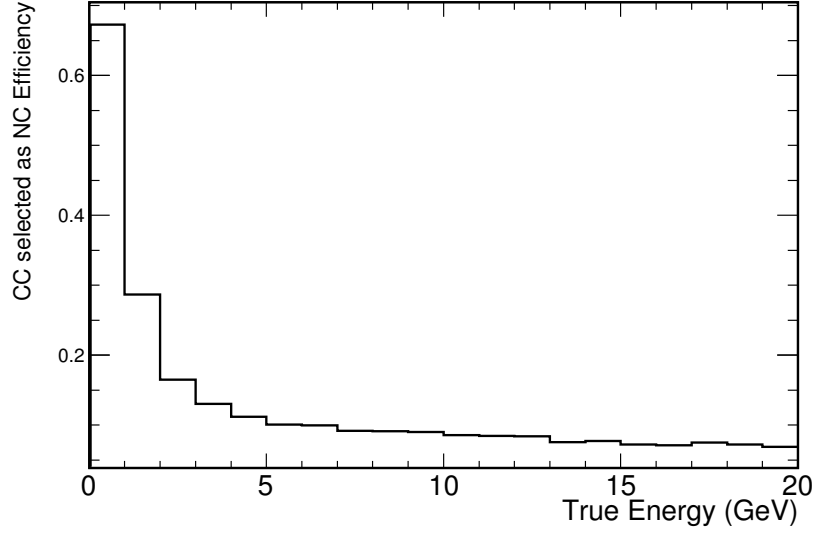
Figure 5.10: CC selected as NC Selection Efficiency.

The CC background in the NC sample selection efficiency is shown in Figure 5.10.

5.4.4 Final Predictions

The final NC and CC predictions are obtained by adding all the relevant backgrounds to the signal thusly:

$$R_i^{F_{NC}} = R_i^{F_{NC},P} + R_i^{F_{CCinNC}} + R_i^{F_{\nu_\tau NC}} + R_i^{F_{\overline{\nu}_\mu NC}} + R_i^{F_{\nu_e BeamNC}} + R_i^{F_{\nu_e OscNC}}$$

$$R_i^{F_{CC}} = R_i^{F_{CC},P} + R_i^{F_{NCinCC}} + R_i^{F_{\nu_\tau CC}} + R_i^{F_{\overline{\nu}_\mu CC}} + R_i^{F_{\nu_e BeamCC}} + R_i^{F_{\nu_e OscCC}}$$

5.5 Near Detector Fit

The Beam Matrix extrapolation technique described above makes no use of the Near Detector NC data in its prediction of the NC spectrum at the Far Detector.

To make use of this information a fit is performed to improve the agreement between the Near Detector data and MC due to differences in the NC cross sections. The result of this fit can then be applied to the predictions at the Far Detector. The work presented in this section builds upon work performed in [74].

5.5.1 Fitting Cross Sections in the Near Detector

The cross section fitting procedure in the Near Detector (NDFit) proceeds by taking the NC selected spectrum in both data and MC for 4 different beam types Low Energy (LE), Medium Energy (ME), High Energy (HE) and Horn Off (HO). described in Section 3.2. The MC spectrum has the hadron production tuning described in Section 3.9 applied to it to improve the data/MC agreement. As this tuning procedure is based on the CC events it effectively adjusts the product of beam flux and CC cross-sections. Any NC cross sections tunings are determined by the procedure outlined here.

Extracting cross section information from NC events is not easy. As was discussed in Section 5.4.3, unlike CC events the energy measured in the detector is not a good approximation of the incoming energy of the neutrino. Only the energy transferred to the struck nucleus resulting in a hadronic shower can be measured. The incident neutrino will carry away the rest of the energy. The number of NC events at a given reconstructed energy is therefore dependent on the cross section at all true energies greater than the reconstructed energy.

To compensate for neutrinos with a different true energy resulting in an event with the same reconstructed energy 2 steps are taken: Firstly the cross sections are only fitted in terms of effective scale parameters in four fairly wide energy bins. Secondly, data and MC from different beam configurations are used. The major difference in these beams is the energy of the focussed peak in the neutrino

energy spectrum.

The fit to the Near Detector NC selected reconstructed energy spectrum then proceeds by scaling the number of events in 4 ranges of true neutrino energy. The scale factor for each range then acts like an effective NC cross section correction for these energy ranges. The energy ranges used are 0-4 GeV, 4-8 GeV, 8-15 GeV and > 15GeV. These energy ranges were chosen as the first 3 approximately cover the peak of the LE, ME and HE neutrino fluxes and the last bin will cover the High Energy tail. As the HO has no focussing peak it will contribute to all energy parameters.

All the beam exposures are scaled to the same number of events. This will give each beam configuration a comparable contribution to the result of the fit and allow similar accuracies in the various fit ranges to be obtained.

5.5.2 Fitting Technique

The NC selected Near Detector energy spectra for the four different energy configurations are fitted simultaneously using a binned extended maximum likelihood method. The likelihood function ($\mathcal{L}$) is given by:

$$\mathcal{L} = \frac{e^{-N} N^D}{D!} \prod_i \frac{D!}{d_i!} \left(\frac{n_i}{N}\right)^{d_i} \quad \text{where} \quad \begin{cases} d_i = \text{number of data events in bin } i \\ n_i = \text{number of MC events in bin } i \\ D = \sum_i d_i \quad N = \sum_i n_i \end{cases}$$

(5.9)

The first term is a normalisation term which gives the probability of measuring a total number of D events from a Poisson distribution with mean N. The term contained in the product multiplies the probabilities for observing d_i events in

bin i given a Poisson expectation of n_i given that there are N total expected MC events. Bin index i runs over the reconstructed energy spectra of all four beam configurations. The fit returns the 4 parameters for the 4 energy ranges representing scale factor corrections to the NC cross-sections used in the MC simulation. The best fit values for the cross section parameters are obtained by minimising the negative logarithm of $\mathcal{L}$ using MINUIT [85].

5.5.3 Verifying the ND Fit

The fit has been tested by inputting fake data samples with the same statistics as the monte carlo with the true energy bin parameters adjusted to known values and then trying to fit these values back out. In all tests performed the correct parameters were returned. Previous studies [74] using the same technique have shown that if instead of using statistically identical MC, the fake data is shifted by the 4 true energy parameters and then the number of events in each bin is fluctuated by a Poisson probability the result of the fits returns unbiased values with spread of values consistent with the statistical fluctuations.

5.5.4 Correcting the Near Detector MC NC Flux

The intention of the ND Fit is to adjust the Far Detector predicted NC spectrum to take account of differences only present in the MC simulation of NC events. Fitting the nominal NC MC directly to the data will cause a double application of effects that lead to differences in both NC and CC spectra. As the fit parameters will be applied to the predicted Far Detector NC spectrum, which is already predicted from the CC flux at the Far Detector, any correction due to CC flux disagreements will be compensated for twice; once due to the ND fit and again in the prediction of the Far Detector NC flux.

To mitigate against this, before the fit is performed the Near Detector MC is corrected based on information provided by the CC flux prediction at the Near Detector. The purpose of this flux correction is that any scale parameters returned from the fit after this correction will be due to NC cross sections alone. As the ND fit is performed using spectra from 4 different energy configurations the flux correction procedure will need to be carried out 4 times, once for each beam configuration.

Section 5.3.1 outlined the procedure to obtain a CC flux at the Near Detector which was called $T_i^{N_{CC}}$ in the notation of that section[4]

If the exact same transformations are applied to the Near Detector CC selected MC an analogous flux for the MC can be obtained. In the nominal case this will be identical to the input MC flux but there is an important distinction when fitting for systematic errors due to the method employed for this which will be described in Section 7.4.1.

Using the predicted Near Detector CC flux and the predicted Near Detector MC flux a bin by bin correction histogram can be made:

$$F_i^{corr} = \frac{(\text{predicted flux of neutrinos})_i}{(\text{predicted MC flux of neutrinos})_i}$$

The Near Detector NC flux can then be obtained identically to the Far detector NC flux by multiplying by the ratio of cross sections

$$T_i^{N_{NC}} = T_i^{N_{CC}} \frac{\sigma_{NC}}{\sigma_{CC}}$$

and this flux can be corrected using the flux correction histogram to give the neutral current corrected flux

---

[4]Technically the flux would require the fiducial mass and POT scaling but as these will be immediately re-applied they are ignored here.
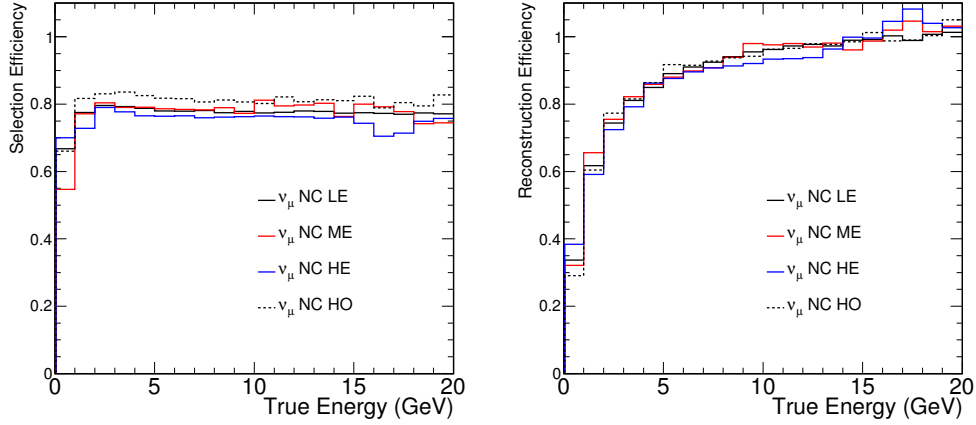
Figure 5.11: Selection Efficiency (left) and Reconstruction Efficiency (right) Corrections as a function of true energy for NC events in the Near Detector.

$$T_{MC\,i}^{Ncorr_{NC}} = T_i^{N_{NC}} F_i^{corr}$$

Where the the subscript MC is to indicate that this is a correction to the MC.

Again identically to the process used at the Far Detector the efficiency correction histograms can be constructed from the nominal Near Detector MC to allow a prediction of the NC selected, flux corrected MC, pure NC spectrum, as a function of true Energy $T_{MC\,i}^{Ncorr_{NC},S}$ to be made. The efficiency correction histograms for the Near Detector for all beams are shown in Figure 5.11. Which shows that the efficiency corrections are broadly similar for all the beam configurations.

As the fit is evaluated in true energy there is no need to convert from true to reconstructed energy or to purity correct the flux corrected selected true energy predictions.

As was mentioned above the NC selected CC background is large enough to deserve correction. For this reason the NC in CC background is also corrected for any CC flux differences using the same procedure as for the NC signal. First the MC Flux corrected CC flux prediction is made:

$$T_{MC\,i}^{Ncorr\,CC} = T_i^{N\,CC} F_i^{corr}$$

and then the reconstruction efficiency and the CC selected as NC selection efficiency corrections can be applied to give the corrected CC selected as NC background as a function of true Energy $T_{MC\,i}^{Ncorr\,CC\,in\,NC}$. The flux corrected spectra $T_{MC\,i}^{Ncorr\,NC}$ and $T_{MC\,i}^{F\,CC\,in\,NC}$ are then used to correct the Near Detector MC before the fit to the Near Detector data takes place.

The MC spectrum that is fitted against the Near Detector Data is therefore made up of the following components for each beam

$$R_i^{Ncorr\,NC} = R_{MC\,i}^{Ncorr\,NC,P} + R_{MC\,i}^{Ncorr\,CC\,in\,NC} + R_i^{N_{\overline{\nu}_\mu}NC} + R_i^{N_{\nu_e}Beam\,NC}$$

Where the $\overline{\nu}_\mu$ and ν_e components are taken from the nominal Near Detector MC. The cross section parameters being fitted for are only applied to the first term.

5.5.5   Cross Check of MC Flux Correction

To check the ND flux correction and fit are working as intended an example fit is described below. Here the data that the fit will be performed to is the nominal MC that has had the 4 true energy parameters shifted by the amounts shown in Table 5.2 for signal NC *and* CC events. This artificial example serves to demonstrate that the method works.

Energy Range (GeV)	0-4	4-8	8-15	> 15
Scale Parameter	1.08	0.985	1.18	0.933

Table 5.2: Example Scale Parameters used in demonstration of flux corrections.

As the same operation is performed to both the CC and NC signal the ND flux correction should remove the effect and the ND fit should return values of 1 for all parameters. The results of the flux correction are shown in Figure 5.12.

As can be seen fitting the nominal ND MC directly to the ND Fake Data will return the input values given in Table 5.2. As the effect will already be in the Near Detector CC flux prediction and will thus be propagated to the Far Detector NC prediction it does not then need to be re-applied due to the NDFit. The NDFit should correct for differences in the NC spectrum only. Figure 5.12 also shows the result of the flux correction procedure described above. The flux corrected NC MC is much closer to the fake data and this is what is used as the input to the fit. The reason the correction is not exact is due to the smearing between energy bins that takes place at the reconstructed to true energy conversion stage. The returned values in this case are:

- Parameter 1 (0 to 4 GeV) : 1.002 ± 0.012

- Parameter 2 (4 to 8 GeV) : 0.990 ± 0.009

- Parameter 3 (8 to 15 GeV): 1.001 ± 0.009

- Parameter 4 (over 15 GeV): 0.990 ± 0.010

Where the errors quoted are statistical. The example fitted parameters returned are consistent with 1 within errors as desired. The result of the fit is also shown in Figure 5.12. It is very similar to the flux corrected spectrum.

5.5.6   Application of ND Fit to Far Detector Prediction

The process of extrapolating the Neutral Current spectrum at the Far Detector has been outlined in Section 5.2 . The ND fit has been described in Section 5.5.
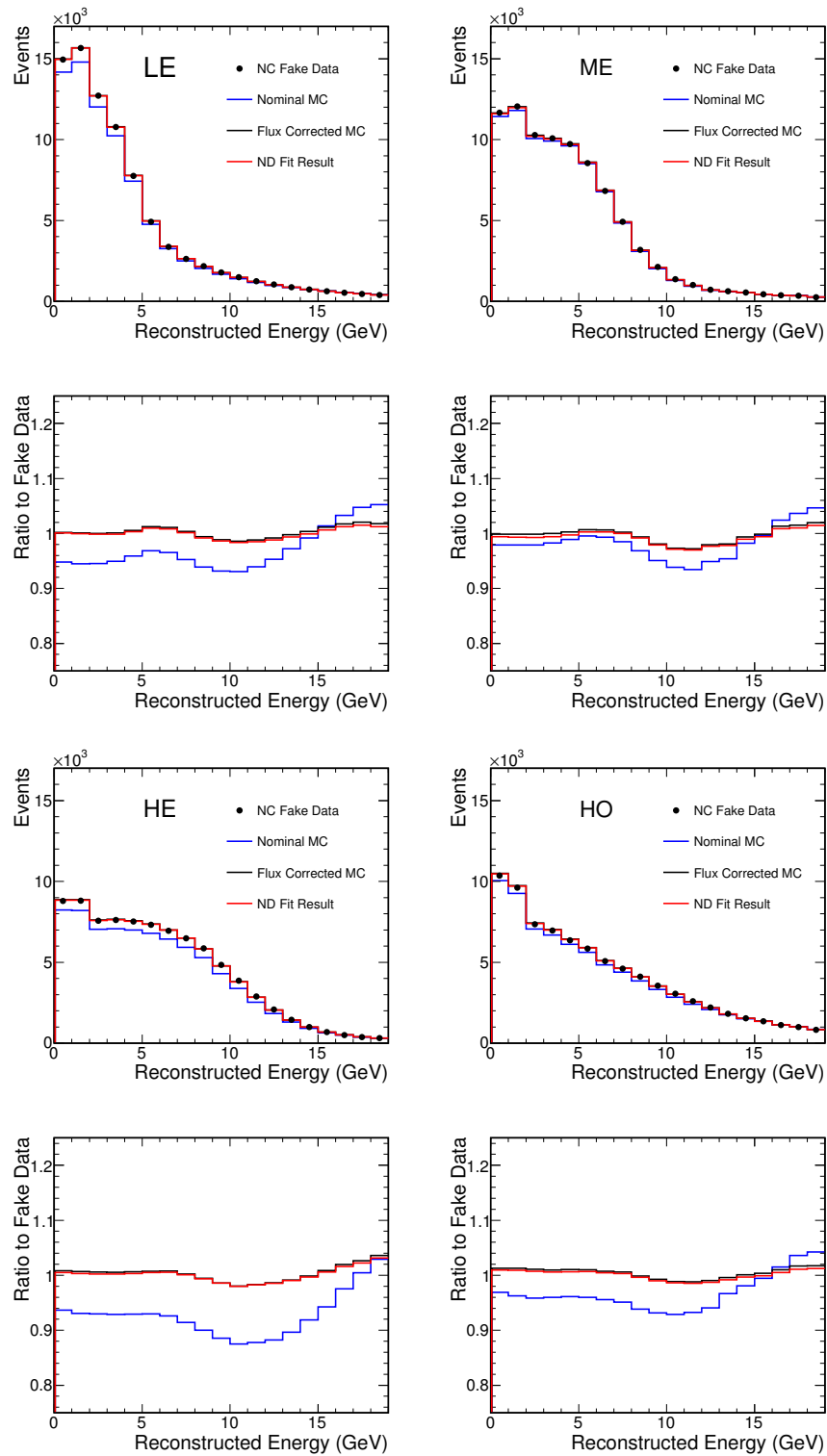
Figure 5.12: An example of the ND fit. The Fake data is shown as black points. The nominal MC before the flux correction is shown in blue. The flux corrected MC used in the ND Fit is shown in black. The Result of the ND fit is shown in Red. Note that all beams are scaled to the same number of events.

The application of the ND fit at the Far Detector is fairly trivial. As they are multiplicative factors in true energy they can be applied at any stage prior to the true to reconstructed energy conversion. In practice they are applied as part of the true to reconstructed energy Matrix by weighting the bins by the appropriate scale factor for the true energy of that bin. In addition to weighting the ν_μ NC signal in the Far Detector the NC selected as CC background in the Near and Far detector are also weighted by the scale parameters.

5.6   Cross Checking the Extrapolation Method

The most fundamental check that the extrapolation is correctly implemented is to extrapolate the nominal Near Detector Monte Carlo that has been used to make the correction histograms as a a fake data sample. The resulting Far Detector prediction should then be compared to a Far Detector fake data spectrum composed of the nominal monte carlo used to make the correction histograms in the Far Detector. The results of this Monte Carlo extrapolation are shown in Figure 5.13. The agreement is not expected to be exact as the Beam Matrix is statistically independent of both the Near and Far Detector Monte Carlo. The results of the ND fit are 1 for all parameters as would be expected as the input ND MC is identical to the input ND fake data.

Both NC and CC predictions agree very well with fluctuations $< 0.6\%$ in all energy bins and is within the statistical fluctuations expected. These fluctuations are much smaller than those expected from the actual Far Detector data so the agreement is considered adequate for use in the analysis.
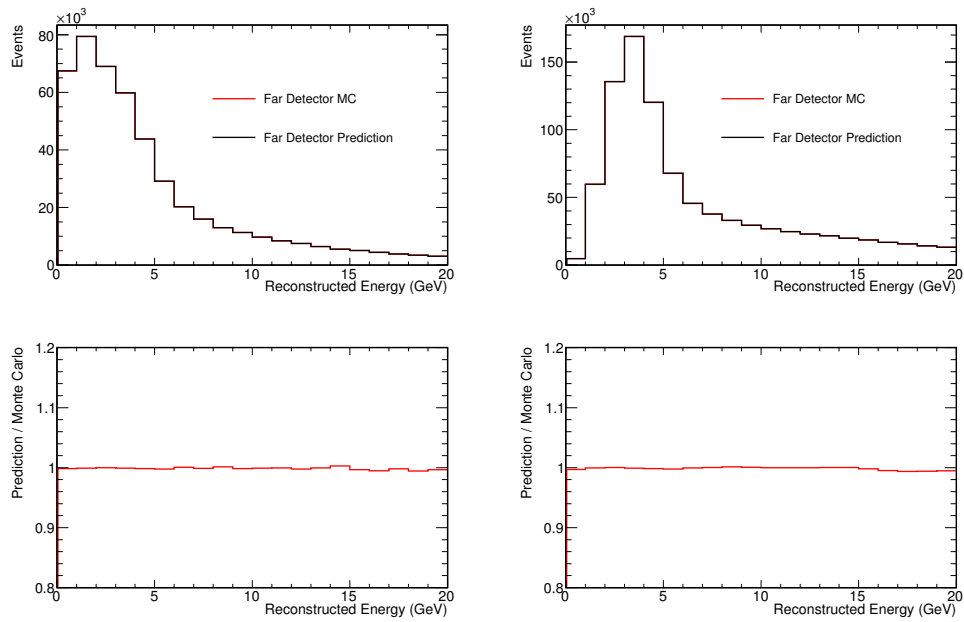
Figure 5.13: Cross check extrapolation comparing FD MC in black to extrapolated ND MC in red. The CC spectrum is on the the left and the NC spectrum on the right. The ratio of the FD prediction to the FD monte carlo is shown below the spectrum.

Chapter 6

Oscillations Including Sterile Neutrinos

The mathematical formalism for neutrino oscillations was demonstrated in Chapter 2 where it was applied to the standard model of 3 flavour neutrino oscillations. The impressive body of experimental evidence to support this theory was also presented although mention was made of the possibility of a third mass splitting and a fourth mass eigenstate. As was discussed in Chapter 2 this fourth neutrino if it exists would have to be sterile to satisfy the precise measurements of the Z width. One such way to search for sterile neutrinos is the examination of NC events. In the MINOS experiment the measured rate of CC interactions at the Far Detector is expected to be reduced due to the beam ν_μ undergoing $\nu_\mu \leftrightarrow \nu_\tau$ oscillations. However the rate of detected NC events under the assumption of 3 flavour oscillations should be the same as all flavours of neutrino equally contribute. For this reason a depletion of the NC event rate could be a possible signature of oscillations of active to sterile neutrinos. The subject of this thesis is the search for mixing between active and sterile neutrinos. In this chapter the mathematical formalism

for 4 flavour neutrino oscillations is described. The models described here have been used in [86].

6.1 Four Flavour Mixing Matrix

To allow for mixing between the three active flavours and a possible sterile flavour a 4th mass eigenstate is required. The mixing matrix then becomes a 4x4 unitary matrix instead of the 3x3 used in Section 2.3.1.

A 4x4 matrix has a possible 6 mixing angles and 6 phases. However 3 of these phases are majorana phases and not relevant to an oscillations experiment and can be ignored[1] . It is possible to express the mixing matrix as 6 rotations matrices about the Euler axes R_{ij} where ij refers to the plane in which the rotation takes place. The ordering of the rotations is arbitrary leading to many possible parameterisations of the matrix. The parameterisation presented below has been chosen to make the analysis as straight-forward as possible.

The MINOS experiment was designed to measure the atmospheric splitting Δm_{32}^2. It has no sensitivity to the much smaller mass splitting Δm_{21}^2. In this as in other analyses the mass states m_1 and m_2 are considered degenerate. A rotation of 2 degenerate mass states in the ij plane is unmeasurable and the corresponding mixing angle θ_{ij} disappears from the oscillation probabilities. A further consideration when choosing a parameterisation is that for the purposes of the analysis presented here it is desirable that the U_{e3} component of the mixing matrix should become 0 when $\theta_{13} = 0$. This will allow the the ν_e component of the 3rd mass eigenstate to be distinguished from the effects of sterile neutrinos.

For these reasons the general form of the mixing matrix used in this analysis is written as:

---

[1]see Section 2.3.1

$$U = R_{34}\left(\theta_{34}\right) R_{24}\left(\theta_{24}, \delta_2\right) R_{14}\left(\theta_{14}\right) R_{23}\left(\theta_{23}\right) R_{13}\left(\theta_{13}, \delta_1\right) R_{12}\left(\theta_{12}, \delta_3\right)$$

$$= R_{34}\left(\theta_{34}\right) R_{24}\left(\theta_{24}, \delta_2\right) R_{14}\left(\theta_{14}\right) R_{23}\left(\theta_{23}\right) R_{13}\left(\theta_{13}, \delta_1\right) \tag{6.1}$$

Where δ_k represent the CP violating phases and the removal of the final term is due to the assumption of $m_1 = m_2$ mass degeneracy mentioned above allowing θ_{12} to be set to 0.

When expressing the full mixing matrix in the form of rotations each individual rotation matrix has the form:

$$R_{ij}^{pq}(\theta_{ij}, \delta_k) = \begin{cases} \cos\theta_{ij} & p = q = i \text{ or } p = q = j, \\[2mm] 1 & p = q \neq i \text{ and } p = q \neq j, \\[2mm] \sin\theta_{ij}e^{-i\delta_k} & p = i \text{ and } q = j, \\[2mm] -\sin\theta_{ij}e^{i\delta k} & p = j \text{ and } q = i \\[2mm] 0 & \text{otherwise} \end{cases} \tag{6.2}$$

where p and q indicate the rows and columns of R_{ij}. Substituting the results of Equation 6.2 for the various rotation matrices into Equation 6.1 the mixing matrix can be written in the form:

$$U = \begin{pmatrix} U_{e1} & U_{e2} & c_{14}s_{13}e^{-i\delta_1} & s_{14} \\[2mm] U_{\mu 1} & U_{\mu 2} & -s_{14}s_{13}e^{-i\delta_1}s_{24}e^{-i\delta_2} + c_{13}s_{23}c_{24} & c_{14}s_{24}e^{-i\delta_2} \\[2mm] U_{\tau 1} & U_{\tau 2} & -s_{14}c_{24}s_{34}s_{13}e^{-i\delta_1} - c_{13}s_{23}s_{34}s_{24}e^{i\delta_2} + c_{13}c_{23}c_{34} & c_{14}c_{24}s_{34} \\[2mm] U_{s1} & U_{s2} & -s_{14}c_{24}c_{34}s_{13}e^{-i\delta_1} - c_{13}s_{23}c_{34}s_{24}e^{i\delta_2} - c_{13}c_{23}s_{34} & c_{14}c_{24}c_{34} \end{pmatrix} \tag{6.3}$$

Where $c_{ij} = \cos\theta_{ij}$ and $s_{ij} = \sin\theta_{ij}$ and only the terms that this analysis is

sensitive to and that will be used in the calculation of oscillation probabilities in the next section have been expressed in terms of their mixing angles and phases.

6.2   4 Flavour Oscillation Probabilities

Recalling Equation 2.9 derived in Chapter 2 the oscillation probability for mixing between any number of neutrino flavours is given by

$$
P(\nu_\alpha \to \nu_\beta) = \delta_{\alpha\beta} - 4 \sum_{i>j} \Re\mathfrak{e} \left[U_{\beta i} U_{\alpha i}^* U_{\beta j}^* U_{\alpha j} \right] \sin^2 \Delta ij
$$
$$
+ 2 \sum_{i>j} \Im\mathfrak{m} \left[U_{\beta i} U_{\alpha i}^* U_{\beta j}^* U_{\alpha j} \right] \sin 2\Delta ij \tag{6.4}
$$

where the notation $\Delta_{ij} = (m_i^2 - m_j^2)L/4E$ has been introduced. In Chapter 2 expansions of this expression in terms of standard model 3 flavour oscillations were considered. Here a full 4 flavour expansion is desired. This expression can be expanded to give the oscillation probabilities of any flavour but as the NuMI beam is mainly composed of ν_μ only the expansion in terms of this flavour are considered. When performing the expansion certain simplifications can be made. Firstly as was mentioned above utilising the knowledge that $\Delta_{21} \ll \Delta_{31}$ the mass eigenstates m_1 and m_2 can be considered degenerate. Thus any terms in Δ_{21} can be set to 0. Furthermore this degeneracy implies that $\Delta_{42} = \Delta_{41}$ and $\Delta_{32} = \Delta_{31}$. To avoid confusion with the atmospheric parameters which has thus far been referred to as Δm_{32}^2 this parameter will be be given the label 31.

Using these simplifications Equation 6.4 can be expanded to give the ν_μ oscillation probabilities as follows:

$$P(\nu_\mu \to \nu_\mu) = 1 - 4 \left\{ |U_{\mu3}|^2 \left(1 - |U_{\mu3}|^2 - |U_{\mu4}|^2\right) \sin^2 \Delta_{31} \right.$$

$$+ |U_{\mu4}|^2 \left(1 - |U_{\mu3}|^2 - |U_{\mu4}|^2\right) \sin^2 \Delta_{41}$$

$$\left. + |U_{\mu4}|^2 |U_{\mu3}|^2 \sin^2 \Delta_{43} \right\} \tag{6.5}$$

$$P(\nu_\mu \to \nu_\alpha) = 4\mathfrak{Re} \left\{ |U_{\mu3}|^2 |U_{\alpha3}|^2 \sin^2 \Delta_{31} + |U_{\mu4}|^2 |U_{\alpha4}|^2 \sin^2 \Delta_{41} \right.$$

$$\left. + U_{\mu4}^* U_{\alpha4} U_{\mu3} U_{\alpha3}^* \left(\sin^2 \Delta_{31} - \sin^2 \Delta_{43} + \sin^2 \Delta_{41}\right) \right\}$$

$$+ 2\mathfrak{Im} \left\{ U_{\mu4}^* U_{\alpha4} U_{\mu3} U_{\alpha3}^* \left(\sin 2\Delta_{31} + \sin 2\Delta_{43} - \sin 2\Delta_{41}\right) \right\} \tag{6.6}$$

Where α can be any of e, τ or s and the normality $\left(\sum_i |U_{\beta i}|^2 = 1\right)$ and orthogonality $\left(\sum_i U_{\alpha i} U_{\beta i}^* = 0\right)$ conditions have been used to eliminate the matrix elements corresponding to the first and second mass states.

The square of the moduli of the matrix elements can be obtained from Equation 6.3.

Examination of the mixing matrix shown at 6.3 and the probabilities in Equation 6.6 reveals that in the general mixing model under the assumptions already mentioned there are ten parameters, most of which are unknown. These are five mixing angle, three mass splittings and two CP-violating phases.

For the model to be usefully applied in the MINOS experiment further simplifying assumptions must be made. The first of which is to fix the value of θ_{13} to either 0 or the limit provided by the CHOOZ experiment. This limit is at the best fit value Δm_{32}^2 from the latest MINOS analysis to give a value of $\theta_{13} = 0.21$. When fixing θ_{13} to the CHOOZ limit value of θ_{13} the CP violating phase δ_1 is fixed to $3\pi/2$ which studies revealed to be the value that produced the largest ν_e appearance at the Far Detector. Thus θ_{13} and δ_1 are eliminated as free parameters leaving only 8. A further simplification arises due to the MINOS experiment

having no sensitivity to δ_2 and thus it can be safely set to 0. The final reduction is made by setting θ_{14} to 0 as non zero values were shown to have very little effect on the oscillation probabilities. This leaves 7 free parameters.

Before discussing specific applications of the model the potential for matter effects is considered [87]. Travelling through dense matter will lead to an alteration of the oscillation probabilities in a similar way to solar oscillations as a result of coherent NC scattering from the nucleons in that matter. Active neutrinos will acquire an effective matter potential whereas sterile neutrinos will not. These effective potentials are identical for ν_μ and ν_τ so that there is no overall effect when considering $\nu_\mu \leftrightarrow \nu_\tau$ oscillations. However in the case of $\nu_\mu \leftrightarrow \nu_s$ oscillations the matter potential difference will not be zero. This will lead to modifications in the mixing angle and oscillation length similar to that observed in the the MSW effect[2]. For normal hierarchies this will lead to a suppression of the oscillation probability (and for inverted hierarchies an enhancement) relative to $\nu_\mu \leftrightarrow \nu_\tau$ mixing. Neutrinos with an energy of > 12 GeV that have travelled through several thousand km of dense material would be expected to display such effects. The NuMI beam by contrast produces neutrinos with a peak energy of ≈ 3 GeV that travel only 735 km through the earth before detection. At this energy and distance, matter effects will only produce sub percent changes to the oscillation probabilities mainly confined to neutrino energies less than 2 GeV. These effects are therefore small enough to be considered negligible and are not considered in the analysis that follows.

---

[2]see Section 2.4.2
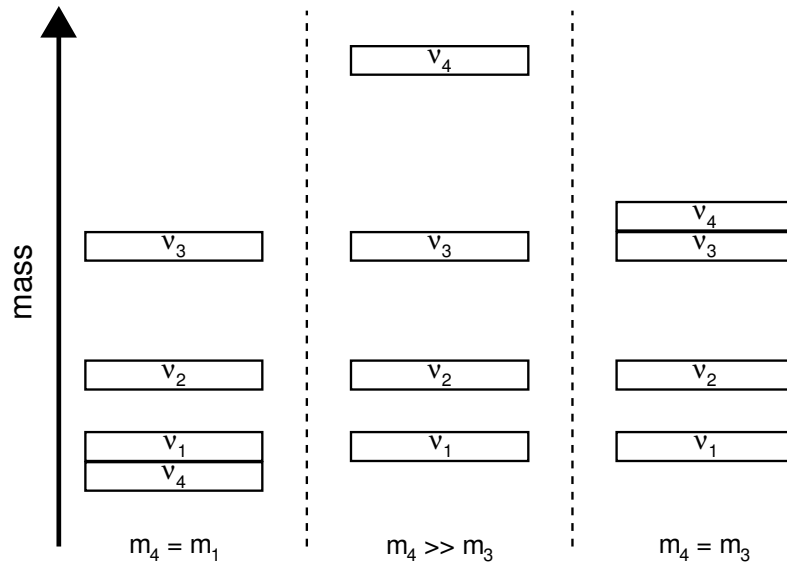
Figure 6.1: The hierarchy of mass eigenstates considered when simplifying the 4 flavour model. Figure taken from [86].

6.3 Special Cases of 4 Flavour Oscillation

To make the model phenomenologically useful certain assumptions about the mass of the 4th mass eigenstate are made so that the model relies on only one mass splitting Δm^2_{31}. Three ways to achieve single mass scale dominance are considered. Firstly the mass of the fourth eigenstate could be degenerate with the first and second mass eigenstates; secondly the mass of the fourth eigenstate could be much larger than the mass of the third eigenstate and thirdly the fourth mass eigenstate could be degenerate with the third mass eigenstate. These possible neutrino mass hierarchies are shown in Figure 6.1 and are discussed individually below.

6.3.1 Model with $m_1 = m_4$

In this case the assumption that m_1 and m_4 are degenerate is made. As the assumption that m_1 and m_2 are degenerate has already been made this therefore implies that m_2 and m_4 are degenerate. A consequence of this is that the mixing

angles can be set such that $\theta_{14} = \theta_{24} = 0.0$. In this model there is no ν_e or ν_μ component in the fourth mass eigenstate but there is a ν_s component in the 3rd mass eigenstate. This reduces the number of parameters in Equation 6.6 to 4 so that it can be written as:

$$
\begin{aligned}
P(\nu_\mu \to \nu_\mu) &= 1 - 4|U_{\mu 3}|^2 \left(1 - |U_{\mu 3}|^2\right) \sin^2 \Delta_{31} \\
P(\nu_\mu \to \nu_\alpha) &= 4|U_{\mu 3}|^2 |U_{\alpha 3}|^2 \sin^2 \Delta_{31}
\end{aligned}
\tag{6.7}
$$

The values of the matrix elements in the model when expressed as mixing angles are:

$$
\begin{aligned}
|U_{e3}|^2 &= s_{13}^2 \\
|U_{e4}|^2 &= 0 \\
|U_{\mu 3}|^2 &= c_{13}^2 s_{23}^2 \\
|U_{\mu 4}|^2 &= 0 \\
|U_{\tau 3}|^2 &= c_{13}^2 c_{23}^2 c_{34}^2 \\
|U_{\tau 4}|^2 &= s_{34}^2 \\
|U_{s3}|^2 &= c_{13}^2 c_{23}^2 s_{34}^2 \\
|U_{s4}|^2 &= c_{34}^2
\end{aligned}
$$

and substituting these expressions into Equation 6.7 gives the oscillation probabilities in terms of mixing angles as:

$$P(\nu_\mu \to \nu_\mu) = 1 - 4\cos^2\theta_{13}\sin^2\theta_{23}\left(1 - \cos^2\theta_{13}\sin^2\theta_{23}\right)\sin^2\left(1.27\Delta m_{31}^2 L/E\right)$$

$$P(\nu_\mu \to \nu_e) = \sin^2(2\theta_{13})\sin^2\theta_{23}\sin^2(1.27\Delta m_{31}^2 L/E)$$

$$P(\nu_\mu \to \nu_\tau) = \sin^2(2\theta_{23})\cos^4\theta_{13}\cos^2\theta_{34}\sin^2(1.27\Delta m_{31}^2 L/E)$$

$$P(\nu_\mu \to \nu_s) = \sin^2(2\theta_{23})\cos^4\theta_{13}\sin^2\theta_{34}\sin^2(1.27\Delta m_{31}^2 L/E) \tag{6.8}$$

A fit to this model using the MINOS data is the main result of thesis and is presented in the next Chapter.

6.3.2 Model with $m_4 \gg m_3$

In the second case it is assumed that the mass m_4 is much larger than the mass m_3. The consequence of this is that the rapid oscillations between the large mass splitting averages out so that $\sin^2\Delta_{41}$ and $\sin^2\Delta_{43} = 1/2$ and $\sin(2\Delta_{41})\sin(2\Delta_{43}) = 0$. The mass of m_4 is assumed to be $\mathcal{O}(\text{eV}^2)$ such that the rapid oscillations result in this averaging out at the Far Detector but no observable deficit of neutrinos will be seen at the Near Detector. Using these simplifications reduces the number of parameters in Equation 6.6 to 5 which can now be expressed as:

$$P(\nu_\mu \to \nu_\mu) = 1 - 4\left\{|U_{\mu3}|^2\left(1 - |U_{\mu3}|^2 - |U_{\mu4}|^2\right)\sin^2\Delta_{31} + \frac{|U_{\mu4}|^2}{2}\left(1 - |U_{\mu4}|^2\right)\right\}$$

$$P(\nu_\mu \to \nu_\alpha) = 4\Re\left\{|U_{\mu3}|^2|U_{\alpha3}|^2 + U_{\mu4}^* U_{\alpha4} U_{\mu3} U_{\alpha3}^* \sin^2\Delta_{31}\frac{|U_{\mu4}|^2|U_{\alpha4}|^2}{2}\right\} \tag{6.9}$$

Where the imaginary term in the $P(\nu_\mu \to \nu_\alpha)$ probability disappears as a consequence of the choice of $\delta_2 = 0$ and $\theta_{14} = 0$. The expressions for the matrix elements in terms of angles are unchanged by these assumptions. This model is

not considered in this thesis but has been used in MINOS publications [86] and is included here for completeness.

6.3.3 Model with $m_4 = m_3$

In the 3rd case shown in Figure 6.1 the assumption is made that $\Delta m_{43}^2 \approx 0$. Under this assumption there would be no observable mixing between the sterile and active neutrinos. This conclusion arises from considering the results from the SNO experiment [32] which demonstrate that any coupling between active and sterile neutrinos must take place in the third and fourth mass eigenstates. This would therefore require observation of oscillations at very small mass splittings which would not be possible with the baseline available to the MINOS experiment. This simplification is therefore not considered in this thesis or in related MINOS publications.

Chapter 7

Sterile Neutrino Analysis

7.1   Introduction

In this chapter the extrapolation procedure detailed in Chapter 5 is applied to the Near Detector data and the resulting predictions compared to the recorded data in the Far Detector to constrain various models.

Before examining any Far Detector data the sources of systematic uncertainties that could effect the oscillation fit results are considered. The sources of the uncertainty and the method used for determining the size of the effect on the analysis are described.

The first result presented is the outcome of the ND fit which is common to all subsequent analyses presented. Secondly a cross check standard model 3 flavour neutrino oscillation analysis is performed and a search made for active neutrino disappearance. Finally the data is fitted using the full 4 flavour formalism developed in Chapter 6.

The analysis procedure was finalised before examining any Far Detector data. This is to minimise the possibility of biasing results to any expected answer.

When performing an analysis the NC and CC spectrum for the two run periods are extrapolated separately and fit simultaneously. The binning scheme in reconstructed energy used is 1 GeV bins for events with energy from 0 to 20 GeV and then 1 bin for events with energies between 20 and 120 GeV.

The ND fit is performed only once using all the data from both run periods and the result applied to both Run I and Run II. This is to compensate for Run period II having no ME or HE data.

7.2 Fitting

A binned fit is performed between the Far Detector prediction and the observed data in the Far Detector. Maximising the likelihood function based on the contents of the bins is equivalent to maximising the likelihood ratio ($\lambda(\mathcal{O})$) [88] given by

$$\lambda(\mathcal{O}) = \mathcal{L}(\boldsymbol{e}(\mathcal{O}); \boldsymbol{o})/\mathcal{L}(\boldsymbol{o}; \boldsymbol{o}) \tag{7.1}$$

where $\mathcal{L}(\boldsymbol{e}(\mathcal{O}); \boldsymbol{o})$ represents the likelihood function of obtaining $\boldsymbol{o}$ given expectation $\boldsymbol{e}(\mathcal{O})$ and $\boldsymbol{o} = (o_1, o_2...o_k)$ and $\boldsymbol{e} = (e_1, e_2...e_k)$ are the vectors of observed and expected numbers of events in bin i and the $\mathcal{O}$ is to make explicit that $\boldsymbol{e}$ is dependent on the oscillation parameters being fitted for. Maximising Equation 7.1 is equivalent to minimising the quantity $-2\ln\lambda(\mathcal{O})$. For independent Poisson distributed o_i this yields [25]: (excluding the term in the square bracket)

$$-2\ln\lambda(\mathcal{O}) = 2\sum_{i=1}^{N} (e_i(\mathcal{O}) - o_i) + o_i\ln(o_i/e_i(\mathcal{O})) \left[+ \sum_j \frac{\Delta\alpha_j^2}{\sigma_j^2} \right] \tag{7.2}$$

Where $e_i(\mathcal{O})$ is the expected number of events and o_i is the observed number of events in bin i. If o_i is 0 then the second term of the first summation is 0.

This likelihood function has the property that it asymptotically obeys a χ^2 distribution and can therefore also be used for goodness of fit tests.

The expression in square brackets describes the penalty term applied to any systematic uncertainties used in the fit. $\Delta\alpha_j$ describes the shift from the nominal value of the j-th uncertainty and σ_j the uncertainty associated with that error. When including systematic uncertainties in the fit $\mathcal{O}$ now represents the effects of oscillations and systematics. These uncertainties are described in the next section. As the systematic errors were evaluated using the 4 flavour model, only the four flavour analysis uses systematic error parameters in the fit. The cross check 3 flavour analysis fit makes no use of systematic uncertainties in the fit and treats the systematic errors in a different way. In this way the fitting technique is demonstrated to be bias free when fitting for systematics uncertainties.

7.3 Systematic Errors

There are many sources of error that could lead to incorrect best fit values being returned from the fitting function. These errors can lead to inaccuracies in the Far Detector prediction in many different ways. Some of the errors will shift the event energies, some will change the number of selected signal events, some will change the predicted number of background events. The various systematic errors, expected to impact on the analysis are described below along with the methods used to estimate the size of the error.

7.3.1 Relative Normalisation

The inter-detector normalisation has many contributing causes that have been studied in [89]. The first is how well the live time and proton on target (POT)

counting of the detectors relative to each other is known. The uncertainty in the live time is essentially negligible and 2 separate methods of counting the POT using the values from the processed files and from the data base agree to 0.32%. This is therefore used as the systematic error for this source.

The fiducial mass of the Far Detector is not precisely known due to the 0.2% uncertainty in the thickness and density of the steel and scintillator. A check on the Near Detector was made by dividing the fiducial volume into halves in x, y and z. This reveals a difference in the number of events in each half of 0.53%, 0.14% and 0.43% respectively with each being seperately used as a systematic. The largest contribution to the relative normalisation is the estimate of a possible difference between the efficiency of reconstructing events at the Near and Far Detector that is unmodelled in the MC. This was checked for by a scanning exercise performed in [90], in which events were examined by eye to find any that were missed by the reconstruction. The result is an inter detector difference of 3%. Further checks on the detectors that would only effect NC event reconstruction such as detector noise and scintillator light mis-modelling were revealed to be negligible in a study performed in [91].

Adding all the sources of relative normalisation error in quadrature gives an overall normalisation error of 3.2%

7.3.2   NC Background in the CC Spectrum

The uncertainty on the NC background in the CC spectrum due to mis-modelling is estimated by the process of taking well constructed CC events in Data and MC and removing the muon track to leave only the hadronic shower. These events are then put through the reconstruction software to study the efficiency of reconstructing events in Data and MC. This allows for a more direct comparison between data

and MC. This has been evaluated in [92] as a 25% uncertainty on the number of background NC events in the CC selected spectrum. This systematic uncertainty is not expected to have a large impact on the analysis as this background is very small.

7.3.3 CC Background in the NC Spectrum

Two separate studies to estimate the uncertainty on the CC background in the NC spectrum are described in [93]. The first involved comparing the NC selected data to the MC divided into true NC and CC events as a function of reconstructed energy. The initial NC selection was made using a simple cuts based method [86] and then the events selected in each energy bin are examined in terms of the ANN presented in Chapter 4. A fit between the MC and the data is then performed by separately scaling the true NC and CC components of each ANN PID spectrum obtained for each energy bin. The result of this analysis was the CC background in the NC spectrum required to be scaled up by up to 20%, although in general it was less than this.

The second study uses the data and MC from the 4 beam configurations used in the NDFit described in Section 5.5. The method assumes that the ratio of the number of true CC(NC) events in the LE configuration to the number of true CC(NC) events in any of the other 3 configurations is the same in the data and the MC.

The total number of NC selected events in the Low Energy configuration N^{LE} can be written as the sum of the NC and CC components:

$$N^{LE} = N_{NC}^{LE} + N_{CC}^{LE} \tag{7.3}$$

For an alternate configuration the number of selected NC and CC events may be written as:

$$N^{Alt} = r_{NC}^{Alt} N_{NC}^{Alt} + r_{CC}^{Alt} N_{CC}^{Alt} \tag{7.4}$$

Where $r_{NC} = N_{NC}^{Alt}/N_{NC}^{LE}$ and $r_{CC} = N_{CC}^{Alt}/N_{CC}^{LE}$ are determined from the MC simulation

Solving Equations 7.3 and 7.4 yields the solutions:

$$N_{LE}^{CC} = (N^{Alt} - r_{NC}^{Alt} N^{LE})/(r_{CC}^{Alt} - r_{NC}^{Alt})$$

$$N_{LE}^{NC} = (N^{Alt} - r_{CC}^{Alt} N^{LE})/(r_{NC}^{Alt} - r_{NC}^{Alt}) \tag{7.5}$$

The final uncertainty on N_{LE}^{CC} results from taking the weighted average of the solutions of Equation 7.5 obtained with each of the other 3 beam configurations

This process gives an error on the N_{LE}^{CC} component of $\approx 10\%$.

The final value used in the analysis was chosen such that it was consistent with the two different estimation techniques summarised above. Therefore an uncertainty of 15% on the number of CC background events in the selected NC spectrum is used.

7.3.4   Far Detector Cleaning

The Far Detector cleaning designed to separate real spill events from detector noise and cosmic ray induced events was outlined in Section 4.2.3. The noise and cosmic ray cleaning effects events with different energies and are consequently estimated by 2 different systematic errors. These are discussed in [76]. The noise systematic error (which includes the effect of the fiducial cut on reconstruction efficiency)

mainly effects events with a low reconstructed energy (E). It is estimated at 7.8% for $E < 0.5$ GeV and 1.5% for 0.5 GeV $< E < 0.75$ GeV. The cosmic ray cuts effect events at all energies and the systematic error on the efficiency is estimated with the functional form $0.161 \exp(-E/6.96 \text{ [GeV]})$.

7.3.5 Near Detector Cleaning

The Near Detector cleaning designed to remove reconstruction pathologies was outlined in Section 4.2.2. The uncertainty associated with this cleaning is discussed in [74]. The major impact of this cleaning comes from the cut on the number of strips. As the data/MC agreement is poor in this variable in the region of interest the uncertainty in the Near Detector cleaning is estimated as half of the difference made by adjusting the strip cut by ± 1. The cleaning only really effects events with low reconstructed energy E and the error is estimated as 15.2% for $E < 0.5$ GeV, 2.9% for 0.5 GeV $< E < 1.0$ GeV and 0.4% for 1.0 GeV $< E < 1.5$ GeV.

7.3.6 ANN Selection Efficiency

As was seen in Chapter 4 the agreement between data and MC in the selection parameter is good but not exact. This disagreement could lead to uncertainties in the measured parameters in an oscillation fit. This systematic is estimated from the size of the observed disagreement between data and MC. The number of events in the Near Detector Data PID distribution is integrated as a function of PID separation parameter up to the nominal cut value of 0.633. The MC PID distribution is then integrated in the same way until the number of events selected is the same as that found in the Near Detector MC. The value of PID parameter this corresponds to is 0.661. The difference between these 2 cut values of 0.028 is taken to be the 1σ value of systematic uncertainty for the ANN selection Efficiency.

7.3.7   Hadronic Energy Measurement

There is a chain of conversions and calibrations performed that take the measured detector response to a hadronic shower and calculate a conversion factor that will estimate the resulting shower energy. This conversion factor could be incorrect in 2 separate ways. Firstly the relative conversion factor between the 2 detectors could be wrong. Examination of the calibration chain in [94] estimates this effect at 3%. This uncertainty is termed the relative hadronic calibration.

Secondly the absolute conversion factor between detector response and hadronic energy could be incorrect in both detectors in the same way. This could be due to a combination of effects. Studies of the calibration chain performed in [94] estimate the uncertainty on the absolute energy scale at 5.7%. This calibration study is made using muon tracks from cosmic rays thus any differences due to the modelling of the hadronic showers between data and MC will be a further source of systematic uncertainty. The modelling of hadronic showers was studied in [95]. Various effects in the intra-nuclear rescattering were considered. Intra-nuclear rescattering is where low energy pions in the final state interact with nucleons before being detected. The effects that were studied included pion branching ratios and cross sections for pion absorption. Further effects considered were the formation times and changes to the hadronisation models used in the generation of hadronic showers. The result of this study is a true energy dependent (E_t) systematic uncertainty. This is combined with the 5.7% calibration uncertainty to give the overall absolute hadronic energy error as:

$$5.7\% \oplus 8.2\% \qquad E_t < 0.5 \text{ GeV}$$

$$5.7\% \oplus 2.7\% + 3.7\% \exp(-0.25E_t) \qquad 0.5 < E_t < 10 \text{ GeV}$$

$$5.7\% \oplus 3\% \qquad E_t > 10 \text{ GeV}$$

7.3.8   Track Energy

The momentum of muons that stop in the detector are measured from the distance travelled in the detector. The momentum of muons that exit the detector are measured from the curvature in the magnetic field. Studies performed in [96] have shown that the uncertainty in the measured momenta of muons is 2%. As only the CC events make use of the muon momentum in the energy estimation of an event this error only effects the CC spectrum.

7.3.9   Cross Section Uncertainties

The cross sections for interactions in the detectors used in the MC simulation are provided by NEUGEN [64]. The uncertainties in these cross sections are therefore estimated by adjusting some of these NEUGEN cross section parameters.

Quasi-elastic scattering and resonant production dominate the cross section at low ($\lesssim 1$ GeV) energies. Therefore the first parameters adjusted are the axial vector masses for quasi-elastic scattering (M_A^{QE}) and resonant production (M_A^{RES}). These are each described by a single parameter in NEUGEN. A study described in [97] provides the $\pm 1\sigma$ uncertainties in these values as 0.1485 for M_A^{QE} and 0.168 for M_A^{RES} which is 15% in both cases. These two parameters are scaled at the same time in a systematic error termed CCMA.

At high energies (> 10 GeV) deep inelastic scattering (DIS) processes dominate. In NEUGEN the resonance to DIS transition region cross sections are adjusted in terms of various different neutrino interactions via KNO_{ijk} parameters. A KNO_{ijk} parameter is a scaling parameter that alters the multiplicity distribution of the final state hadronisation in neutrino nucleon interactions.

For each KNO parameter $i = 1, 2$ determines whether the interaction was CC or NC, $j = 1 - 4$ labels whether the interaction was ν or $\overline{\nu}$ on either proton or neutron and k is the final state multiplicity. The only parameters found to have any influence on the analysis are KNO_{112} and KNO_{122} which refer to CC $\nu - p$ multiplicity 2 interactions and CC $\nu - n$ multiplicity 2 interactions respectively. A study performed in [97] estimates the uncertainty on both these parameters as 33%. These two parameters are scaled at the same time in a systematic error termed KNO_{112122}.

7.3.10 Beam Tuning Uncertainty

The beam tuning process described in Section 3.9 adjusts a set of parameters to improve the modelling of the hadron production from the target. These parameters have errors associated with them and hence the result of the beam tuning has an error associated with it. This is described in [66]. In addition to the parameters in the tuning other effects not related to the hadron production are included in the error estimation such as uncertainties in the horn currents, and misalignment of the horns and target. All these effects are combined together for either the plus or minus sigma values to produce an error band for the neutrino flux. The size of the $\pm 1\sigma$ errors can be seen in Figure 7.1.
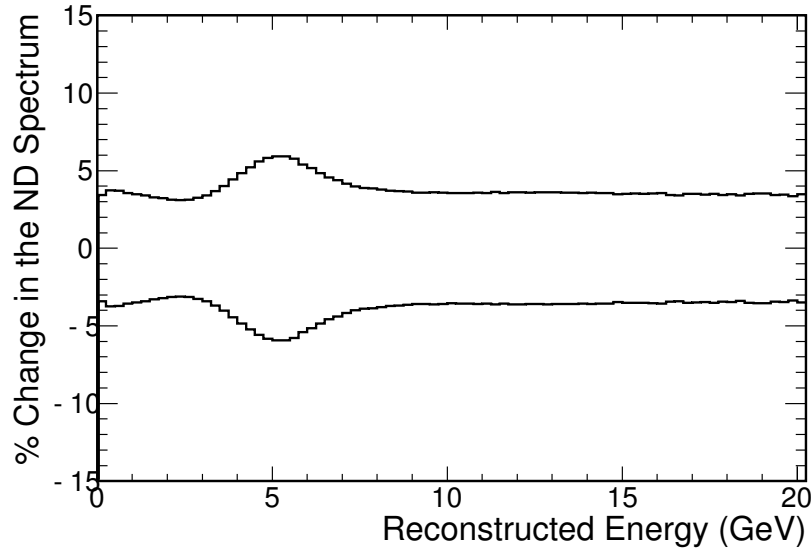
Figure 7.1: The error band for the beam tuning parameters as a function of reconstructed energy for Near Detector ν_μ interactions.

7.4 Effects of Systematic Errors

The effect of the systematic errors described above on the analysis is determined using the following procedure. For the systematic error being considered a high statistics fake data set is made for the Near and Far Detector by adjusting the nominal MC by the $\pm 1\sigma$ error. In addition the Far Detector fake data set has oscillations applied to it. The entire extrapolation chain and fit to the oscillation parameters is then carried out with the fake data set in the place of the real data. The difference between the oscillation parameters returned for a fake data set and the parameters returned for the fit to the nominal spectrum is taken as an indicator of the effect of that particular systematic error on the analysis. For the purposes of this study the 2 components that make up the CCMA and KNO_{112122} systematic are both adjusted in the same direction when creating the $\pm 1\sigma$ fake data sets.

The oscillation model used is the $\Delta_{41} = 0$ with oscillation parameters $\Delta m_{32}^2 =$

2.43×10^{-3} eV^2, $\theta_{13} = 0$, $\theta_{23} = 0.6$ and $\theta_{34} = 0.3$. The nominal fit returns the input value. The sizes of the resulting systematic shifts and the effect on the fit to the oscillation parameters are shown graphically in Figure 7.2 and tabulated in Table 7.1.

Examining the effect the different sources of systematic uncertainty produce, demonstrates the approach of using 2 detectors and the beam matrix is very successful at correcting for sources of uncertainty that effect both detectors such as the beam tuning, KNO$_{112122}$ and PID cut.

Systematic errors that only effect one detector such as relative normalisation and energy scale have a larger effect as information between the 2 detectors cannot compensate for them. All of the relative errors are applied to the Far Detector with the exception of the Near Detector cleaning. This error effects low energy bins where the signal for oscillations is expected and hence causes a large shift in fitted parameters.

The sources of uncertainty that lead to the biggest shift in the fitted oscillations are the normalisation, Near Detector cleaning and the CC background in the NC spectrum. These will be used as nuisance parameters in the 4 flavour fit for sterile oscillations.

7.4.1 Fitting with Systematic Errors

The 3 biggest systematic errors are included as nuisance parameters in the fit as described in Equation 7.2. The method for incorporating the systematic errors in the fit is as follows. For each systematic that is to be used in the fit the MC is adjusted by $\pm 1\sigma$. The full extrapolation chain including the ND Fit is then performed on the adjusted MC. Ratios are formed between the $\pm 1\sigma$ systematic adjusted MC spectrum predictions and the spectrum produced using the nomi-
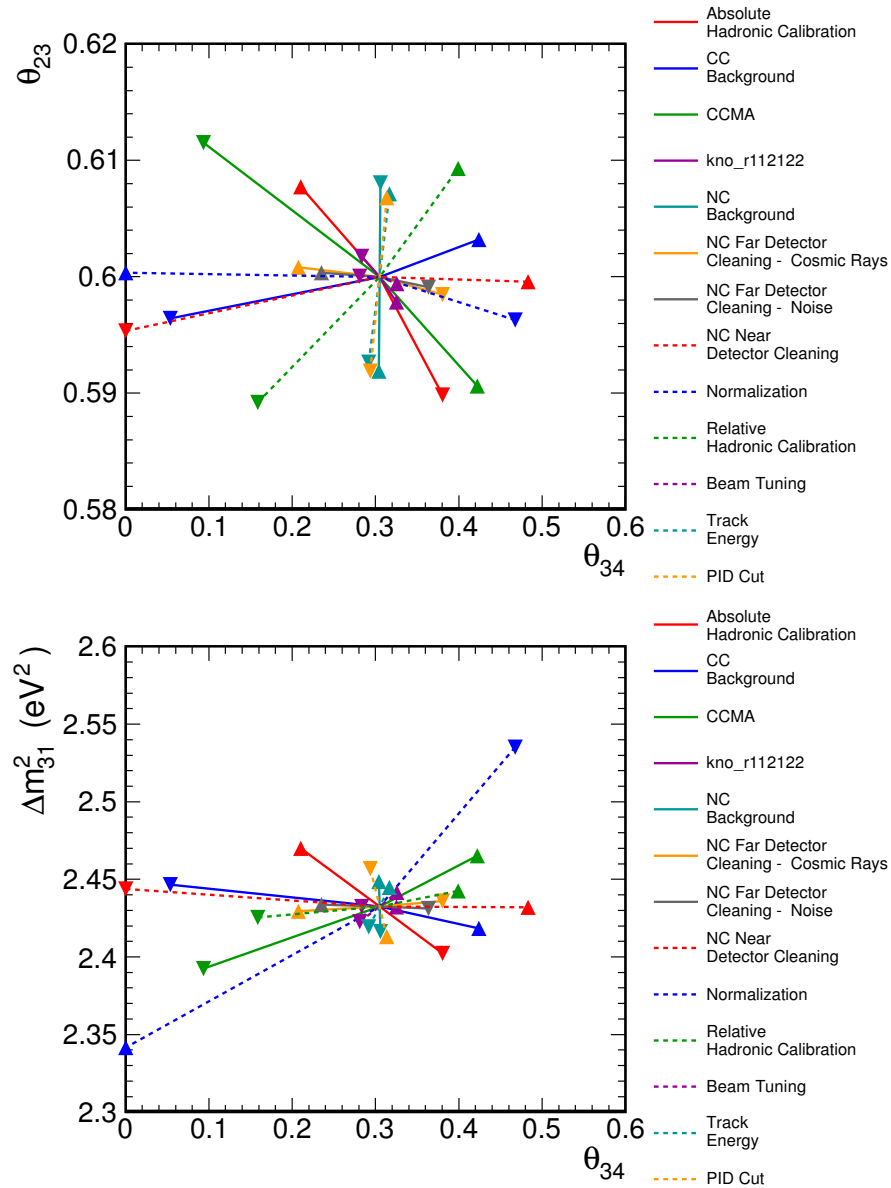
Figure 7.2: The shifts in oscillation parameters due to each systematic uncertainty considered. Input parameters are $\Delta m_{31}^2 = 2.43 \times 10^{-3}$ eV^2, $\theta_{23} = 0.6$ and $\theta_{34} = 0.3$ with θ_{13} fixed to 0.0. The direction of the triangle (up or down) marking the point indicates whether the shift is $\pm 1\sigma$.

Systematic	Shift	Δm^2_{32}	θ_{23}	θ_{34}
Absolute Hadronic	$+\sigma$	0.0400	0.0077	-0.0898
Energy	$-\sigma$	-0.0277	-0.0102	0.0802
CC Background	$+15\%$	-0.0116	0.0032	0.1241
	-15%	0.0165	-0.0036	-0.2463
CCMA	$+15\%$	0.0352	-0.0094	0.1221
	-15%	-0.0376	0.0115	-0.2063
KNO_{112122}	$+33\%$	0.0023	-0.0022	0.0249
	-33%	0.0026	0.0018	-0.0166
NC Background	$+25\%$	0.0186	-0.0081	0.0040
	-25%	-0.0137	0.0081	0.0058
NC Far Detector	$+\sigma$	-0.0006	0.0008	-0.0926
Cleaning - Cosmic Rays	$-\sigma$	0.0060	-0.0015	0.0805
NC Far Detector	$+\sigma$	0.0037	0.0004	-0.06490
Cleaning - Noise	$-\sigma$	0.0011	-0.0009	0.06338
NC Near Detector	$+\sigma$	0.0019	-0.0004	0.1830
Cleaning	$-\sigma$	0.0139	-0.0047	-0.3000
Normalisation	$+3.2\%$	-0.0885	0.0004	-0.3000
	-3.2%	0.1052	-0.0037	0.1679
Relative Hadronic	$+3\%$	0.0126	0.0093	0.0994
Energy	-3%	-0.0045	-0.0108	-0.1413
Beam Tuning	$+\sigma$	0.0116	-0.0005	0.0257
	$-\sigma$	-0.0074	0.0000	-0.0190
Track Energy	$+2\%$	0.0148	0.0071	0.0167
	-2%	-0.0105	-0.0073	-0.0081
PID Cut	$+\sigma$	-0.0168	0.0068	0.0132
	$-\sigma$	0.0270	-0.0081	-0.0061

Table 7.1: The shifts in the fitted sterile oscillation parameters due to systematic errors. The estimated 1σ values are also shown. Those with only $\pm\sigma$ are described in the text. Input parameters are $\Delta m^2_{32} = 2.43 \times 10^{-3}$ eV^2, $\theta_{23} = 0.6$ and $\theta_{34} = 0.3$ with θ_{13} fixed to 0.0.

nal MC. The prediction at any desired value of a systematic uncertainty is then determined by using these ratios to interpolate between the three spectrums by forming an appropriate ratio for the effect of that systematic error at that value.

Multiplying the prediction by this ratio then gives the prediction with the effect of that systematic included. This technique is described in greater detail in [98]. It has been validated as accurate enough and whilst not as correct as re-evaluating the entire prediction at the different values of systematic errors each time it is computationally much quicker.

To prevent the systematic being adjusted to unrealistic values to improve the fit, the systematics that are being fitted for have penalty terms applied in the fit. This is shown in Equation 7.2.

7.5   Results of ND Fit

Regardless of the oscillation model that is being considered the spectra recorded at the Near Detector are the same. This means that the result of the ND fit that is applied will be the same in all the oscillation analyses that follow. The spectra at the Near Detector for the 4 beam configurations are show in Figure 7.3. In addition to the data and nominal MC, the result of the CC flux correction and the result of the fit for each beam configuration are also shown.
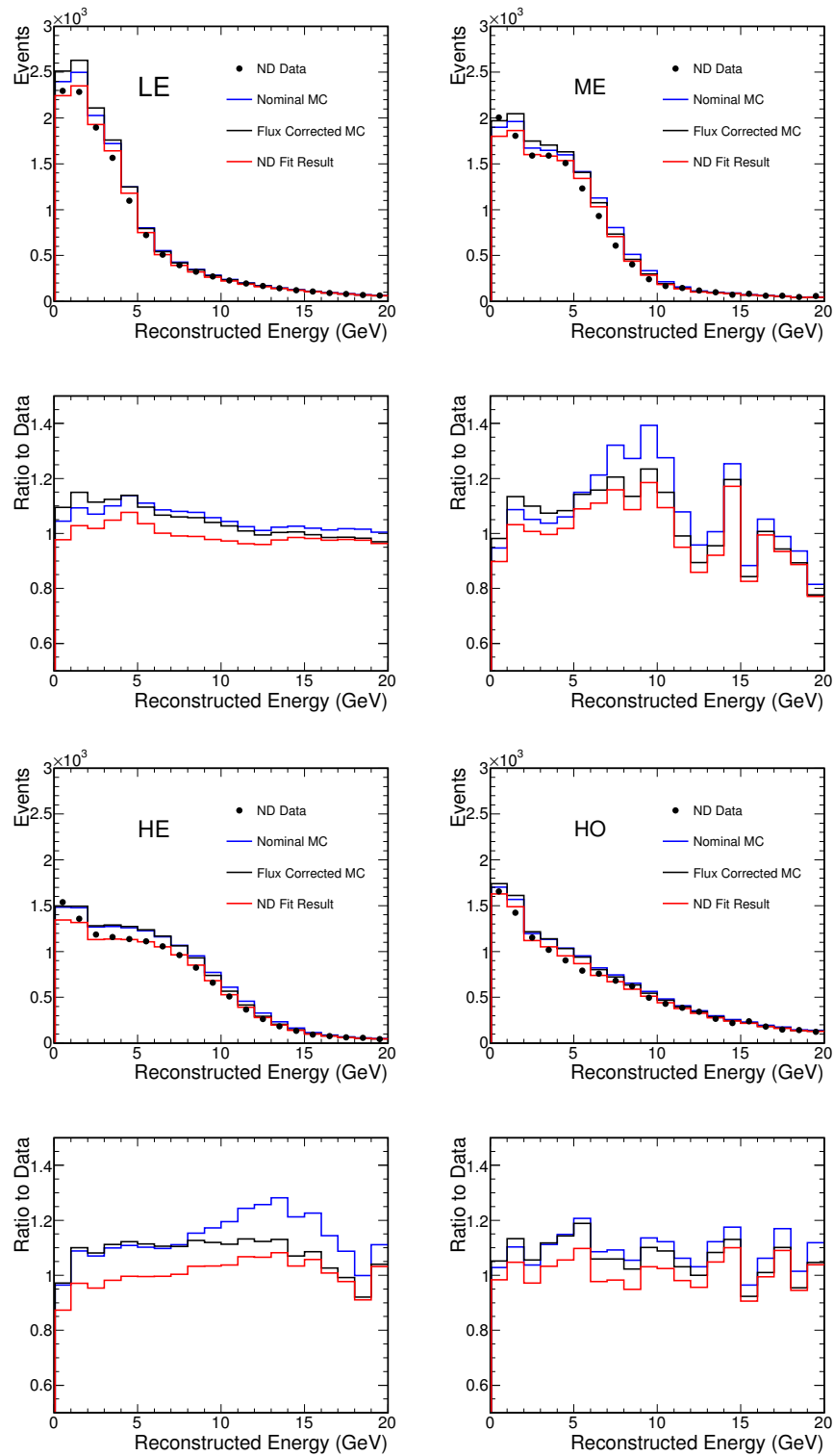
Figure 7.3: The result of the ND Fit. The data is shown as black points. The nominal MC before the flux correction is shown in blue. The flux corrected MC used in the ND Fit is shown in black. The result of the ND fit is shown Red. Note that all beams are scaled to the same number of events.

The Nominal MC is in general much higher than the data. The flux correction improves the agreement at medium to high energies in all beam configurations but tends to slightly worsen agreement at lower energies. The parameters returned from the fit are therefore quite large:

- Parameter 1 (0 to 4 GeV) : 0.815 ± 0.028

- Parameter 2 (4 to 8 GeV) : 0.923 ± 0.021

- Parameter 3 (8 to 15 GeV): 0.801 ± 0.024

- Parameter 4 (over 15 GeV): 0.987 ± 0.026

Where the errors quoted are statistical. The result of the fit suggests that the NC prediction at the Far Detector needs to be scaled down by $\approx 9\%$ across all energy bins. These corrections are applied to the Far Detector prediction before fitting as described in Section 5.5.6. Due to the nature of the process relevant systematic errors that effect the result of the ND Fit will effect the Far Detector in the same way and thus the effects should cancel. These parameters are therefore applied directly to the Far Detector.

7.6   Three Flavour Oscillation Results

As a cross check of the extrapolation procedure and as a first search for evidence of sterile neutrinos the Far Detector predictions are fitted to standard three flavour oscillations. The only parameters used in the fit are the mass splitting Δm_{32}^2 and the mixing angle θ_{23}.

Despite only the CC spectrum having sensitivity to three flavour oscillations the fit is performed to the NC and CC spectrums simultaneously to test the
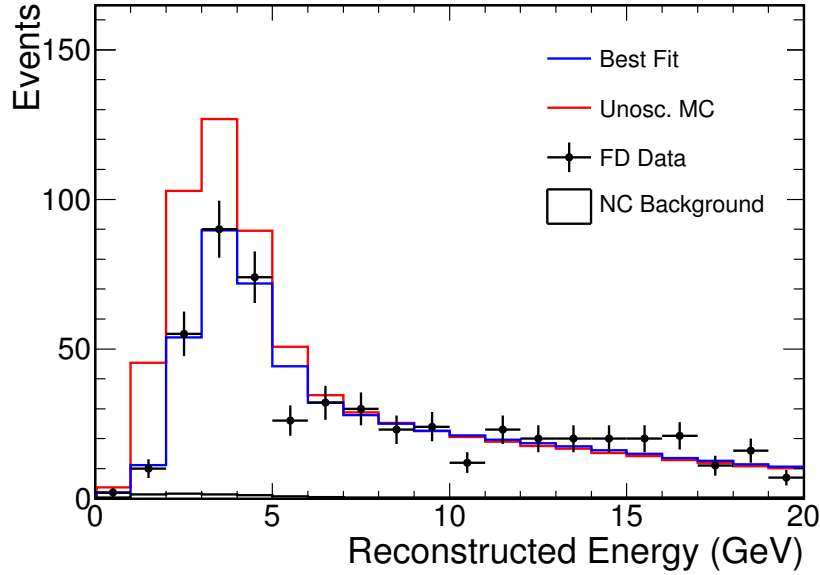
Figure 7.4: The CC prediction for three flavour oscillations. The Far Detector Data is shown in black points with statistical errors. The unoscillated MC is shown in red. The best fit to oscillations is shown as a blue line with the shaded areas showing the systematic uncertainties.

analysis procedure[1]. The best fit spectrum has a $\chi^2/DOF = 90.4/82$ with fitted values:

- $\Delta m_{32}^2 = (2.39_{-0.15}^{+0.23}) \times 10^{-3}$ eV^2

- $\theta_{23} = 0.727_{-0.11}^{+0.22}$

These results are in excellent agreement with previously published MINOS analyses [67].

The CC spectrum resulting from the 3 flavour fit is shown as Figure 7.4.

To look for active neutrino disappearance the best fit predicted NC spectrum at the Far Detector can then be compared to the measured data to determine if the overall measured flux of neutrinos agrees. As has been mentioned before

---

[1]Fits to the CC spectrum only produce almost equal parameters

the NC selection is almost 100% efficient at selecting ν_e events as NC events. Therefore a non 0 value of θ_{13} will result in ν_e appearance at the Far Detector and a consequent change in the selected NC spectrum. To account for this effect the data was also fitted to a three flavour model including a value $\theta_{13} = 0.21$. This value is obtained using the limit of the CHOOZ experiment and the Δm^2_{32} of the latest published dedicated MINOS CC analysis. As the measured mass splitting here is very nearly the same, and that analysis was optimised for the measurement on this result, this is considered adequate. Additional studies showed that the maximum ν_e appearance occurred with the value of the CP violating parameter $\delta = 3\pi/2$. This was then also used in the fit. The result of a non zero θ_{13} is to add many events to the NC spectrum and a very small number to the CC spectrum. As the NC spectrum contains almost no sensitivity to 3 flavour oscillations the result of the fit with $\theta_{13} = 0.21$ is expected to be very close to the fit with $\theta_{13} = 0.0$. This is indeed the case with the Δm^2_{32} and $\sin^2 2\theta_{23}$ agreeing $< 1\%$.

To account for the effect of systematic uncertainties associated with the prediction a process similar to the procedure used to evaluate the effect of the systematic errors in Section 7.4 is employed. For each systematic a fake data sample is produced by adjusting the nominal MC spectrum by the $\pm 1\sigma$ values from Table 7.1 and oscillating the Far Detector fake data. The extrapolation is then performed using the fake data and the error due to that systematic uncertainty is obtained from the difference between the fit and the data in the Far Detector. The errors are assumed to be uncorrelated and are therefore added in quadrature on a bin by bin basis to produce the systematic envelope.

The NC spectrum of the 3 Flavour oscillation prediction is shown as Figure 7.5.

The predictions with and without the ν_e appearance are shown. The errors on the data points are statistical and the shaded areas show the error due to the
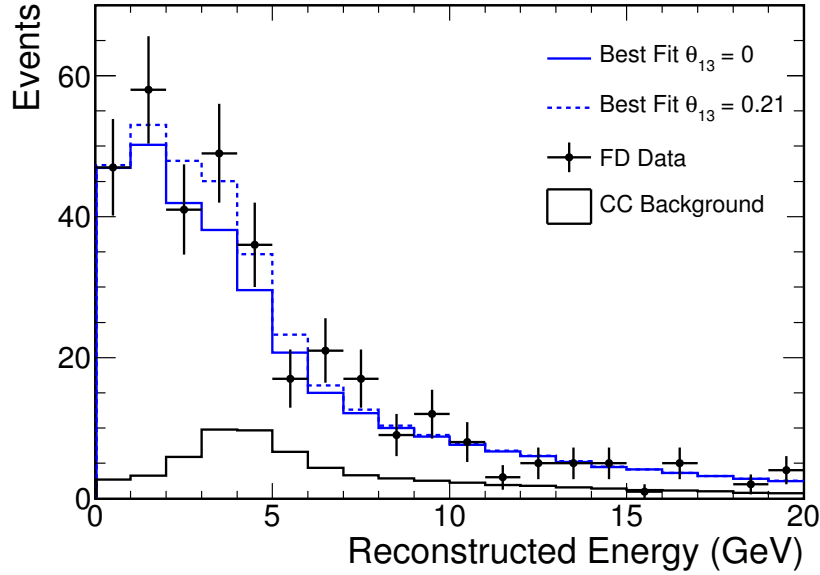
Figure 7.5: The NC prediction for three flavour oscillations. The Far Detector Data is shown in black points with statistical errors. The best fit to oscillations with $\theta_{13} = 0$ is shown as a blue line with the shaded areas showing the systematic uncertainties. The dashed blue line shows the best fit to oscillations with $\theta_{13} = 0.21$.

systematic uncertainty. These are only shown for the no ν_e appearance case for clarity of presentation but the size of the errors for the $\theta_{13} = 0.21$ case are very similar to those of the $\theta_{13} = 0.0$ case. There are 363 events recorded in the Far Detector with an expectation of $340.45 \pm 18.4(\text{stat.})\pm16.5(\text{syst.})$ for no ν_e appearance and $367.02 \pm 19.1(\text{stat.})\pm17.8(\text{syst.})$ with ν_e appearance This corresponds to a 1.2σ deficit or a 0.2σ excess of events respectively.

To quantify any active neutrino disappearance the measured number of expected to observed events is calculated as:

$$R = \frac{N_{data} - B_{CC}}{S_{NC}} \tag{7.6}$$

Where N_{data} is the measured number of data events, B_{CC} is the predicted

background from CC interactions from all flavours and S_{NC} is the predicted NC signal. Table 7.2 shows the numbers of events from Figure 7.5 used in the calculation of R. Also shown in the table are the R values obtained and the associated errors. The first error is statistical and the second error systematic. The R values are consistent with no active neutrino disappearance. These values correspond to maximum depletion in the NC rate at 90% confidence of 4% for no ν_e appearance and 15% for including ν_e appearance.

$\theta_{13} =$	N_{data}	S_{NC}	$B_{CC}^{\nu_\mu}$	$B_{CC}^{\nu_\tau}$	$B_{CC}^{\nu_e}$
0.0	363	238.0	78.2	6.1	18.2
0.21	363	237.5	77.3	5.6	46.7
0.0	$R = 1.09 \pm 0.08 \pm 0.07$				
0.21	$R = 0.98 \pm 0.08 \pm 0.07$				

Table 7.2: Number of events and R values for the no ν_e and ν_e appearance. The first error on R is statistical and the second systematic.

7.7 4 flavour neutrino oscillations

As outlined in Chapter 6 a model has been developed to search for oscillations between active and sterile neutrinos. The case considered here is where the mass splitting $\Delta m_{41}^2 = 0$. The fit is performed using the 3 systematic errors with the largest effect on θ_{34} as nuisance parameters. These are the normalisation, Near Detector NC cleaning and the uncertainty on the CC background in the NC spectrum.

Similarly to the three flavour analysis θ_{13} is not fitted for but is fixed at either 0.0 or at the CHOOZ limit at 0.21. Again the data from the 2 run periods is extrapolated separately.

The best fit oscillation parameters returned from the fit are shown in Table 7.3:

$\theta_{13} =$	χ^2/DOF	Δm^2_{31} (eV^2)	θ_{23}	θ_{34}	Norm	CC Bkg	NC Clean
0.0	89.4/81	$2.44^{+0.23}_{-0.14}$	$0.755^{+0.19}_{-0.12}$	$0.00^{+0.35}$	0.02	0.020	-0.40
0.21	86.7/81	$2.46^{+0.21}_{-0.14}$	$0.849^{+0.12}_{-0.19}$	$0.00^{+0.60}$	0.01	-0.004	-0.05

Table 7.3: Best fit oscillation parameters for 4 flavour oscillations. The errors shown include statistical and systematic components.

The best fit is for $\theta_{34} = 0$ and therefore no sterile oscillations. The systematic uncertainties used in the fit are all fitted to well within their 1σ values.

The energy spectra obtained as a result of the fit are shown in Figure 7.6. The resulting 68 and 90% confidence limit contours are shown in Figure 7.7. The one dimensional projection of the $\Delta\chi^2$ between for the three parameters is shown in Figure 7.8

7.8 Discussion

As can be seen there is no evidence for oscillations to sterile neutrinos. The predicted spectrum of Neutral Current interactions under the assumption of Standard Model 3 flavour oscillations agrees with the measured data and a more sophisticated fit to a four flavour oscillation model that incorporates sterile neutrinos return zero mixing as the best fit value. Indeed the opposite is almost true in that there appear to be more NC interactions in the Far Detector than predicted although not by any significant amount. The results presented here are in good agreement within errors to the analysis presented in [86] which uses the same data sample and models described in this thesis with a different NC selection and extrapolation method.
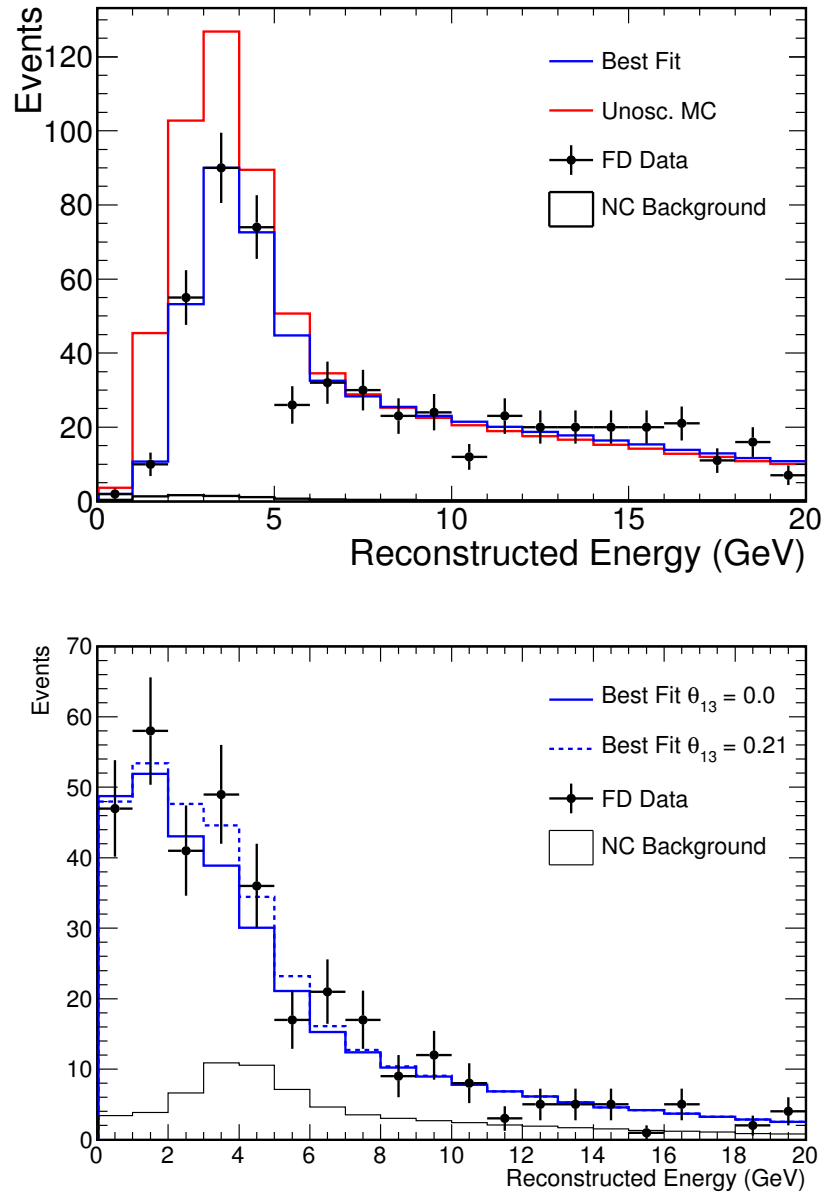
Figure 7.6: The best fit NC and CC spectrum to the 4 flavour oscillation model. Data with statistical errors are shown as points. The best fit with $\theta_{13} = 0.0$ is shown in solid blue. The best fit with $\theta_{13} = 0.21$ in the NC spectrum is shown as the dashed blue line. The unoscillated prediction in the CC spectrum is shown in red.
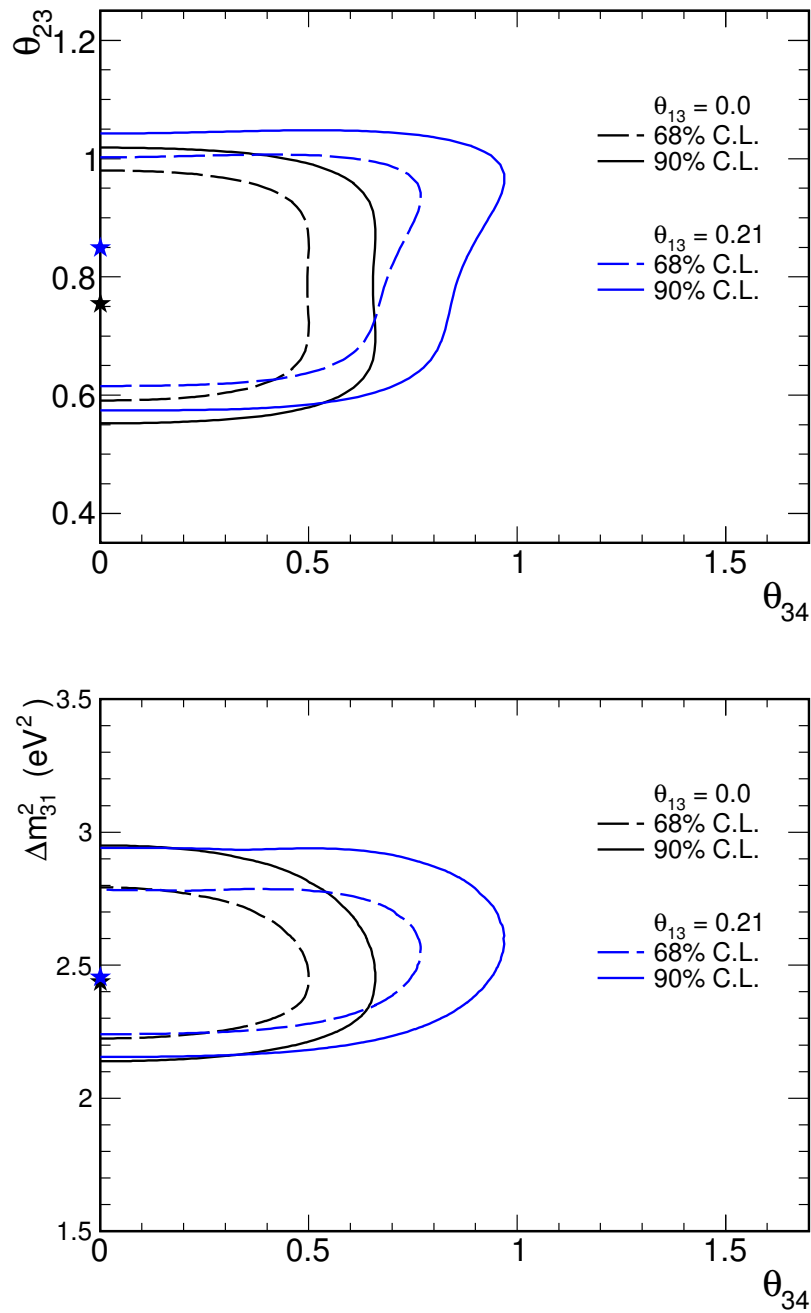
Figure 7.7: The 68% (dashed line) and 90% (solid line) contours for the 4 flavour model fit. The top contour is Δm^2_{31} against θ_{34} The bottom contours is θ_{23} against θ_{34} The black lines show the $\theta_{13} = 0.0$ model the blue lines the $\theta_{13} = 0.21$ model.

Figure 7.8: One dimensional $\Delta\chi^2$ projections for 4 flavour model. Black lines for $\theta_{13} = 0.0$ and blue lines for $\theta_{13} = 0.21$

Chapter 8

Conclusion and Outlook

MINOS has been operating since early 2005 and has so far collected 7×10^{20} protons on target worth of data. T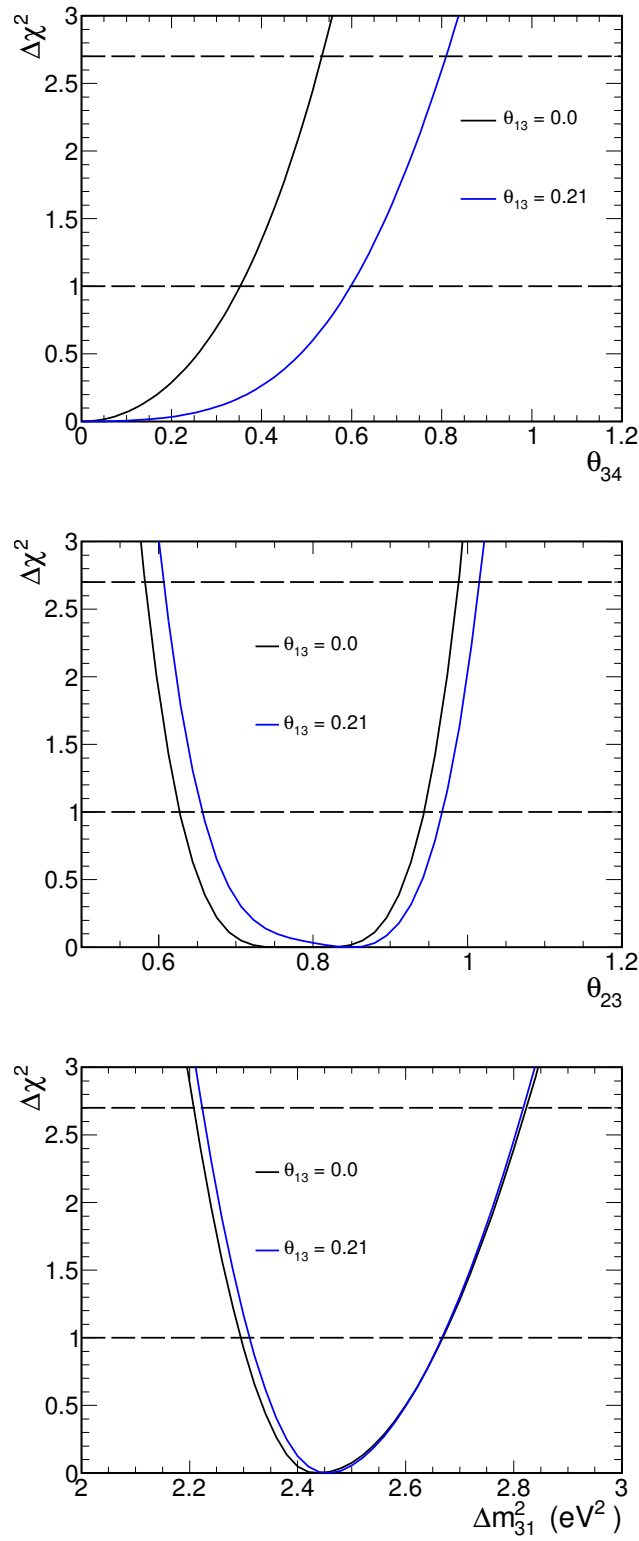he body of knowledge added to the neutrino physics sector not just in the atmospheric mixing parameters but in topics as diverse as cross section measurements and studies of atmospheric muons is considerable.

The experiment was primarily designed for studying neutrino oscillations and in particular to measure the atmospheric mixing parameters. This has been achieved by analysis of the spectrum of CC neutrino interactions and this is very much the flagship analysis performed by the experiment. The latest result was published in 2008 and only uses half of the current data set. Despite this it still provides the best measurement in the world of the atmospheric mass splitting Δm^2_{32}. A new analysis using the entire data set collected so far is expected in 2010.

In addition to the CC analysis performed by MINOS the experiment has been used to investigate other neutrino phenomena. Investigations of the unknown but small mixing θ_{13} have been performed and are already comparable to the world best limit set by the CHOOZ experiment. An updated analysis using the full data

set available is eagerly awaited by the particle physics community.

Analyses of $\overline{\nu}_\mu$ oscillations in the atmospheric sector have been undertaken for the first time and whilst not producing a strong result show promise, especially in light of the fact that NuMI has recently been running with an anti-neutrino beam and therefore the statistics for this analysis have increased. This updated analysis is expected soon.

The final area in which MINOS has contributed to a study of neutrino oscillation phenomena is in the realm of the Neutral Current interaction and the search for mixing between active and a possible sterile neutrino. Two analyses have been performed in this area [99, 86] with each analysis utilising more data and increasing levels of sophistication in the models used to search for sterile neutrinos. This work has attracted some attention in the wider scientific community [100].

The subject of this thesis is a sterile neutrino search and can be considered complimentary to the published analyses. The steps in the analysis of Neutral Current events were presented. Firstly in Chapter 4 a method of separating NC events from CC events using an Artificial Neural Network was developed. In addition to being used in this thesis the ANN developed will be used in extrapolation techniques developed for future NC analyses.

An extrapolation technique was then developed in Chapter 5 using the already established Beam Matrix method as the basis. This technique is generally favoured in MINOS analyses being used in all the CC results and the forthcoming $\overline{\nu}_\mu$ oscillation analysis. Applying this technique to predict the spectrum of Neutral Current events at the Far Detector is not straightforward and to improve the prediction from the Beam Matrix the prediction is augmented by a technique involving fitting the NC selected MC to the NC selected data spectrum in the Near Detector.

To utilise the extrapolation method developed a model to search for sterile neutrinos that has been used in MINOS publications has also been presented in Chapter 6. This model is presented in very general terms and then specific assumptions about the mass hierarchy of neutrinos are made to allow the model to be realistically used at the MINOS experiment.

The sources of systematic uncertainty considered for the analysis were presented in Chapter 7 along with the result of a cross check of the extrapolation technique and the result of the fit to a model including oscillations to steriles. The result of this analysis is for no oscillations between sterile and active neutrinos and is in good agreement with the published MINOS NC results. It cannot be stated definitively that sterile neutrinos do not exist as the model presented is only sensitive under specific assumptions. Furthermore the experimental evidence against sterile neutrinos is not wholly conclusive as the result of the LSND experiment has not been entirely excluded by the results from the MiniBOONE experiment, although they may be in future analyses.

One final NC analysis is planned at the MINOS experiment utilising the full data set acquired to date and making use of more models involving oscillations between sterile neutrinos than has been presented here.

MINOS is now a mature experiment and will end its period of data taking some time in the next few years. The ground it has broken will be followed by future neutrino experiments with the emphasis very much on the sub dominant θ_{13} mixing. Experiments such as T2K, Nova and Double CHOOZ. Neutrino physics is a rapidly moving field and keeps providing interesting and exciting physics. The MINOS experiment has contributed fully towards this and will continue to do so in the near future.

Appendix A

Defining Figures of Merit

As was mentioned in Chapter 4 the decision about where to place the cut value in the particle identification to achieve good sensitivity will be a balance between selecting as many signal events as possible whilst rejecting as many background events as possible.

A quick and simple way to quantify these contributions to sensitivity is to define a figure of merit that in some way encapsulates these contributions. In this thesis these figures of merit are defined in terms of 2 quantities: efficiency (ϵ) and purity ($\mathbf{P}$). Efficiency is the percentage of the total number of signal events that are selected. Purity is the percentage of selected events that are signal events.

The simplest figure of merit is simply $\epsilon \times \mathbf{P}$. This figure of merit was considered and shown in Chapter 4

The figure of merit maximised in this thesis is:

$$\frac{\epsilon \times \mathbf{P}}{2 - \mathbf{P}}$$

The demonstration of this result was originally shown in [76]. As this experiment is in essence a counting experiment this figure of merit is chosen as it

minimises the fractional error on the number of signal events σ_s/s.

This is equivalent to maximising s^2/σ_s^2 which is easier to calculate. When considering data only n the total number of events selected is available. The number of selected signal events can then be estimated by subtracting the background predicted by the MC simulation.

$$s = n - b$$

The statistical error[1] on the total number of selected events is $\sigma_n = \sqrt{n}$ and the statistical error on the number of background events is $\sigma_b = \sqrt{b}$. If the assumption that the error on the background estimate is independent of the total number of events selected we have

$$\sigma_s^2 = \sigma_n^2 + \sigma_b^2 = n + b$$

Using the definitions of ϵ and $\mathbf{P}$ given in Chapter 4 then numbers of events can be expressed as $s = \epsilon S = n\mathbf{P}$ and $b = n - n\mathbf{P}$ where S is the total number of signal events before selection.

Therefore

$$\frac{s^2}{\sigma_s^2} = \frac{\epsilon S n \mathbf{P}}{n + n - nP}$$

S is the same for all selections so the figure of merit to be maximised is:

$$\frac{\epsilon \times \mathbf{P}}{(2 - \mathbf{P})}$$

---

[1]It is assumed that the systematic errors on the background are small

Bibliography

[1] W. Pauli, Letter, addressed to participants of the Tübingen conference on radioactivity 1930, Available from the CERN Document server: `http://cdsweb.cern.ch/record/83282P`, translation available from `http://www.symmetrymagazine.org/pdfs/200703/logbook_letter_translation.pdf`% relax .

[2] J. Chadwick, The Existence of a Neutron, Proc. R. Soc. Lond. A **136**, 692 (1932).

[3] E. Fermi, Versuch einer Theorie der β-Strahlen. I, Z. Phys. **88**, 161 (1934).

[4] F. L. Wilson, Fermi's Theory of Beta Decay, Am. J. Phys. **36**, 1150 (1968).

[5] H. Beithe and R. Peierls, The "Neutrino", Nature **133**, 532 (1934).

[6] F. Reines and C. L. Cowan, The "Neutrino", Nature **178**, 446 (1956).

[7] F. Reines, C. L. Cowan, F. B. Harrison, A. D. McGuire, and H. W. Kruse, Detection of the Free Neutrino, Phys. Rev. **117**, 159 (1960).

[8] T. D. Lee and C. N. Yang, Question of Parity Conservation in Weak Interactions, Phys. Rev. **104**, 254 (1956).

[9] C. S. Wu, E. Embler, R. W. Hayward, D. D. Hoppes, and R. P. Hudson, Experimental Test of Parity Conservation in Beta Decay, Phys. Rev. **105**, 1413 (1957).

[10] R. L. Garwin, L. M. Lederman, and M. Weinrich, Observations of the Failure of Conservation of Parity and Charge Conjugation in Meson Decays: the Magnetic Moment of the Free Muon, Phys. Rev. **105**, 1415 (1957).

[11] L. Goldhaber, M. Grodzins and A. W. Sunyar, Helecity of Neutrinos, Phys. Rev. **109**, 1015 (1958).

[12] S. L. Glashow, Partial-Symmeteries of Weak Interactions, Nucl. Phys. **22**, 579 (1961).

[13] S. Weinberg, A Model of Leptons, Phys. Rev. Lett. **19**, 1264 (1967).

[14] A. Salam and J. C. Ward, Electromagnetic and Weak Interactions, Phys. Lett. **13**, 168 (1964).

[15] F. J. Hasert et al., Search For Elastic Muon-Neutrino Electron Scattering, Phys. Lett. B **46**, 121 (1973).

[16] F. J. Hasert et al., Observation of Neutrino-Like Interactions Without Muon or Electron in the Gargamelle Neutrino Experiment, Phys. Lett. B **46**, 138 (1973).

[17] F. J. Hasert et al., Observation of Neutrino-Like Interactions Without Muon or Electron in the Gargamelle Neutrino Experiment, Nucl. Phys. B **73**, 1 (1974).

[18] A. Benvenuti et al., Observation of Muonless Neutrino-Induced Inelastic Interactions, Phys. Rev. Lett. **32**, 800 (1974).

[19] G. Danby et al., Observation of High-Energy Neutrino Reactions and the Existence of Two Kinds of Neutrinos, Phys. Rev. Lett. **9**, 36 (1962).

[20] M. Perl et al., Evidence for Anomalous Lepton Production in e^+e^- Annihilation, Phys. Rev. Lett. **35**, 1489 (1975).

[21] ALEPH Collaboration: D. DeCamp et al., Determination of the number of light neutrino species, Phys. Lett. B **231**, 519 (1989).

[22] DONUT Collaboration: K. Kodama et al., Observation of tau neutrino interactions, Phys. Lett. B **504**, 218 (2001).

[23] C. Giunti and C. W. Kim, *Fundamentals of Neutrino Physics and Astrophysics* (Oxford University Press, 2007).

[24] J. R. Davis, Attempt to Detect the Antineutrinos from a Nuclear Reactor by the $\text{Cl}^{37}(\overline{\nu}, e^-)\text{A}^{37}$ Reaction, Phys. Rev. **97**, 766 (1955).

[25] Review of Particle Physics, Physics Letters B **667**, 1 (2008).

[26] B. Kayser, On the quantum mechanics of neutrino oscillation, Phys. Rev. D **24**, 110 (1981).

[27] A. Aguilar et al., Evidence for neutrino oscillations from the observation of $\overline{\nu}_e$ appearance in a $\overline{\nu}_\mu$ beam, Phys. Rev. D **64**, 112007 (2001).

[28] The ALEPH Collaboration The DELPHI Collaboration The L3 Collaboration The OPAL Collaboration The SLD Collaboration The LEP Electroweak Working Group and The SLD Electroweak and Heavy Flavour Groups Collaboration, Precision electroweak measurements on the Z resonance, Phys. Rep. **427**, 257 (2006).

[29] A. M. Bahcall, J. N. Serenelli and B. Sarbani, New Solar Opacities, Abundances, Helioseismology and Neutrino Fluxes, Astrophys. J. **621**, L85 (2005).

[30] R. Davis, D. S. Harmer, and K. C. Hoffman, Search for Neutrinos from the Sun, Phys. Rev. Lett. **20**, 1205 (1968).

[31] J. N. Abdurashitov et al., Solar neutrino flux measurements by the Soviet-American gallium experiment (SAGE) for half the 22-year solar cycle, J. Exp. Theor. Phys. **95**, 181 (2002).

[32] B. Aharmim et al., Electron energy spectra, fluxes, and day-night asymmetries of 8B solar neutrinos from measurements with NaCl dissolved in the heavy-water detector at the Sudbury Neutrino Observatory, Phys. Rev. C **72**, 055502 (2005).

[33] L. Wolfenstein, Neutrino oscillations in matter, Phys. Rev. D **17**, 2369 (1978).

[34] S. Mikheyev and A. Smirnov, Resonant neutrino oscillations in matter, Prog. Part. Nucl. Phys. **23**, 41 (1989).

[35] S. Abe et al., Precision Measurement of Neutrino Oscillation Parameters with KamLAND, Phys. Rev. Lett. **100**, 221803 (2008).

[36] J. Hosaka et al., Solar neutrino measurements in Super-Kamiokande-I, Phys. Rev. D **73**, 112001 (2006).

[37] C. Arpesella et al., Direct Measurement of the ^{7}Be Solar Neutrino Flux with 192 Days of Borexino Data, Phys. Rev. Lett. **101**, 091302 (2008).

[38] SNO with liquid scintillator: SNO+, Progress in Particle and Nuclear Physics **57**, 150 (2006).

[39] C. Achar et al., Detection of muons produced by cosmic ray neutrinos deep underground, Phys. Lett. **18**, 196 (1965).

[40] F. Reines et al., Evidence for High-Energy Cosmic-Ray Neutrino Interactions, Phys. Rev. Lett. **15**, 429 (1965).

[41] K. S. Hirata et al., Experimental study of the atmospheric neutrino flux, Phys. Lett. B **205**, 416 (1988).

[42] R. Becker-Szendy et al., Electron- and muon-neutrino content of the atmospheric flux, Phys. Rev. D **46**, 3720 (1992).

[43] M. Aglietta et al., Experimental Study of Atmospheric Neutrino Flux in the NUSEX Experiment, Europhys. Lett **8**, 611 (1989).

[44] C. Berger et al., A study of atmospheric neutrino oscillations in the Frejus experiment, Phys. Lett. B **245**, 305 (1990).

[45] S. Ahlen et al., Atmospheric neutrino flux measurement using upgoing muons, Phys. Lett. B **357**, 481 (1995).

[46] W. W. M. Allison et al., Measurement of the atmospheric neutrino flavour composition in Soudan 2, Phys. Lett. B **391**, 491 (1997).

[47] S. Hatakeyama et al., Measurement of the Flux and Zenith-Angle Distribution of Upward Through-Going Muons in Kamiokande $II + III$, Phys. Rev. Lett. **81**, 2016 (1998).

[48] Y. Fukuda et al., Evidence for Oscillation of Atmospheric Neutrinos, Phys. Rev. Lett. **81**, 1562 (1998).

[49] Y. Ashie et al., Evidence for an Oscillatory Signature in Atmospheric Neutrino Oscillations, Phys. Rev. Lett. **93**, 101801 (2004).

[50] Y. Ashie et al., Measurement of atmospheric neutrino oscillation parameters by Super-Kamiokande I, Phys. Rev. D **71**, 112005 (2005).

[51] M. H. Ahn et al., Measurement of neutrino oscillation by the K2K experiment, Phys. Rev. D **74**, 072003 (2006).

[52] M. Apollonio et al., Limits on neutrino oscillations from the CHOOZ experiment, Physics Letters B **466**, 415 (1999).

[53] Daya Bay Collaboration: X. Guo et al., A precision measurement of the neutrino mixing angle θ_{13} using reactor antineutrinos at Daya Bay, hep-ex/0701029 (2007).

[54] RENO: reactor experiment for neutrino oscillation at Yonggwang, J. Phys.: Conf. Ser **120**, 05025 (2008).

[55] P. Astier et al., Search for $\nu_\mu \to \nu_e$ oscillations in the NOMAD experiment, Phys. Lett. B **570**, 19 (2003).

[56] B. Achkar et al., Search for neutrino oscillations at 15, 40 and 95 meters from a nuclear power reactor at Bugey, Nucl. Phys. B **434**, 503 (1995).

[57] B. Armbruster et al., Upper limits for neutrino oscillations $\overline{\nu}_\mu \to \overline{\nu}_e$ from muon decay at rest, Phys. Rev. D **65**, 112001 (2002).

[58] A. A. Aguilar-Arevalo et al., Search for Electron Neutrino Appearance at the $\Delta m^2 \sim 1$ eV^2 Scale, Phys. Rev. Lett. **98**, 231801 (2007).

[59] A. A. Aguilar-Arevalo et al., Search for Electron Antineutrino Appearance at the $\Delta m^2 \sim 1$ eV^2 Scale, Phys. Rev. Lett. **103**, 111801 (2009).

[60] R. M. Zwaska, *Accelerator Systems and Instrumentation for the NuMI Neutrino Beam*, PhD thesis University of Texas at Austin, 2005.

[61] J. Hylen et al., NuMI Technical Design Handbook, Internal NuMI report (2003).

[62] MINOS Collaboration: D. Michael et al., The magnetized steel and scintillator calorimeters of the MINOS experiment, Nucl. Instrum. Meth. A: Accelerators **596**, 190 (2008).

[63] GEANT Detector description and simulation tool, CERN Program Library, Long Writeup, W5013, `http://wwwasdoc.web.cern.ch/wwwasdoc/pdfdir/geant.pdf`.

[64] H. Gallagher, The NEUGEN neutrino event generator, Nuclear Physics B - Proceedings Supplements **112**, 188 (2002).

[65] C. Zeitnitz and T. Gabriel, The GEANT-CALOR interface and benchmark calculations of ZEUS test calorimeters, Nucl. Instrum. Meth. A **349**, 106 (1994).

[66] S. Kopp et al., Constraining the Beam Neutrino MC Flux Using the MINOS ND Data, MINOS-doc-2965 (2007).

[67] MINOS Collaboration: P. Adamson et al., Measurement of Neutrino Oscillations with the MINOS Detectors in the NuMI Beam, Phys. Rev. Lett. **101**, 131802 (2008).

[68] MINOS Collaboration: P. Adamson et al., Neutrino and Antineutrino Inclusive Charged-current Cross Section Measurements with the MINOS Near Detector., Accepted for publication in Phys. Rev. D.

[69] MINOS Collaboration: P. Adamson et al., Charge-separated atmospheric neutrino-induced muons in the MINOS far detector, Phys. Rev. D **75**, 092003 (2007).

[70] MINOS Collaboration: P. Adamson et al., Measurement of the atmospheric muon charge ratio at TeV energies with the MINOS detector, Phys. Rev. D **76**, 052003 (2007).

[71] MINOS Collaboration: P. Adamson et al., Observation of muon intensity variations by season with the MINOS far detector, Phys. Rev. D **81**, 012001 (2010).

[72] MINOS Collaboration: P. Adamson et al., Search for Muon-Neutrino to Electron-Neutrino Transitions in MINOS, Phys. Rev. Lett. **103**, 261802 (2009).

[73] J. Evans, Recent Results From the MINOS Experiment, in proceedings of European Physical Society Europhysics Conference on High Energy Physics, (2009), PoS(EPS-HEP 2009)279.

[74] T. M. Raufer, *A study of neutrino oscillations in MINOS.*, DPhil thesis, University of Oxford, 2007.

[75] T. Raufer and G. Tinti, Near Detector data cleaning – updated for daikon MC and cedar reconstruction, MINOS-doc-3422 (2007).

[76] R. P. Litchfield, *Neutrino Induced Events in the MINOS Detectors.*, DPhil thesis, University of Oxford, 2008.

[77] T. M. Mitchell, *Machine Learning - International Edition* (McGraw-Hill, 1997).

[78] G. Cybenko, Approximation by superpositions of a sigmoidal function, Math. Control. Signal. **2**, 303 (1989).

[79] D. F. Shanno et al., Conditioning of Quasi-Newton Methods for Function Minimization, Math. Comput. **24**, 647 (1970).

[80] A. B. P. e. Sousa, *Studies of Nu-mu to Nu-e Oscillation Appearance in the MINOS Experiment.*, PhD thesis Tufts University, 2005.

[81] R. Ospanov, *A Measurement of Muon Neutrino Disappearance with the MINOS Detectors and NuMI Beam*, PhD thesis University of Texas at Austin, 2008.

[82] MINOS Collaboration: P. Adamson et al., Study of muon neutrino disappearance using the Fermilab Main Injector neutrino beam, Phys. Rev. D **77**, 072002 (2008).

[83] J. J. Evans, *Measuring Antineutrino Oscillations with the MINOS Experiment*, DPhil thesis, University of Oxford, 2008.

[84] P. Renton, *Electroweak Interactions* (Cambridge University Press, 1990).

[85] MINUIT - Function Minimization and Error Analysis, CERN Program Library, Long Writeup, D50g, `http://wwwasdoc.web.cern.ch/wwwasdoc/minuit/minmain.html`.

[86] MINOS Collaboration: P. Adamson et al., Search for sterile neutrino mixing in the MINOS long-baseline experiment, Phys. Rev. D **81**, 052004 (2010).

[87] W. Mann, A 3+1 model with sterile neutrino and matter effects, MINOS-doc-4872 (2008).

[88] S. Baker and R. D. Cousins, Clarification of the use of CHI-square and likelihood functions in fits to histograms, Nucl. Instr. and Meth. **221**, 437 (1984).

[89] P. Rodrigues, Notes on the Normalization Systematic, MINOS-doc-6636 (2009).

[90] J. M. Paley et al., Summary of Hand-scan Study of NC Events, MINOS-doc-6714 (2010).

[91] R. Pittam, Normalisation in the NC Analysis, MINOS-doc-3612 (2007).

[92] J. S. Marshall, *A study of muon neutrino disappearance with the MINOS detectors and the NuMI neutrino beam*, PhD thesis University of Cambridge, 2009.

[93] P. Rodrigues and L. Hsu, CC BG in NC Analysis: Position Paper, MINOS-doc-3878 (2007).

[94] R. Nichol, Calibration Position Paper, MINOS-doc-3941 (2008).

[95] Kodorsky, H. M. Gallagher, and S. Dytman, Shower Energy Scale Uncertainty For the Run I+II CC Analysis, MINOS-doc-4287 (2008).

[96] R. Hatcher et al., Range/Energy Task Force Position Paper, MINOS-doc-3134 (2007).

[97] C. Andreopoulos et al., Updated Cross Section Model Uncertainties for the Charged Current Analysis, MINOS-doc-2989 (2007).

[98] C. Backhouse, Systematics interpolation for the 7e20 analysis, MINOS-doc-6048 (2009).

[99] MINOS Collaboration: P. Adamson et al., Search for Active Neutrino Disappearance Using Neutral-Current Interactions in the MINOS Long-Baseline Experiment, Phys. Rev. Lett. **101**, 221804 (2008).

[100] E. Hand, Hunt for the sterile neutrino heats up, Nature **464**, 334 (2010).